MICROCOPY RESOLUTION TEST CHART

NATIONAL BUREAU OF STANDARDS-1963-A

RADC-TR-83-139
Final Technical Report
September 1983

MSW VARIABLE TIME DELAY TECHNIQUES

Westinghouse Electric Corporation

J. D. Adams
S. N. Bajpai
M. R. Daniel
P. R. Emtage
S. H. Talisa
R. W. Weinert

DTIC
SELECTE
OCT 2 4 1983
B

DTIC FILE COPY

ROME AIR DEVELOPMENT CENTER
Air Force Systems Command
Griffiss Air Force Base, NY 13441

83 10   008

This report has been reviewed by the RADC Public Affairs Office (PA) and
is releasable to the National Technical Information Service (NTIS). At NTIS
it will be releasable to the general public, including foreign nations.

RADC-TR-83-139 has been reviewed and is approved for publication.
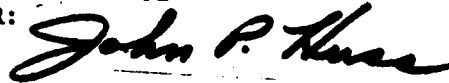
APPROVED: *James C. Sethares*

JAMES C. SETHARES
Project Engineer

APPROVED: *Allan C. Schell*

ALLAN C. SCHELL, Chief
Electromagnetic Sciences Division

FOR THE COMMANDER: *John P. Huss*

JOHN P. HUSS
Acting Chief, Plans Office

If your address has changed or if you wish to be removed from the RADC
mailing list, or if the addressee is no longer employed by your organization,
please notify RADC (EEAC) Hanscom AFB MA 01731. This will assist us in
maintaining a current mailing list.

Do not return copies of this report unless contractual obligations or notices
on a specific document requires that it be returned.

UNCLASSIFIED

REPORT DOCUMENTATION PAGE		READ INSTRUCTIONS BEFORE COMPLETING FORM
1. REPORT NUMBER RADC-TR-83-139	2. GOVT ACCESSION NO. AD-A133770	3. RECIPIENT'S CATALOG NUMBER
4. TITLE *(and Subtitle)* MSW VARIABLE TIME-DELAY TECHNIQUES		5. TYPE OF REPORT & PERIOD COVERED Final Technical Report 1 Oct 80 - 31 Oct 82
		6. PERFORMING ORG. REPORT NUMBER 82-6F3-Delay-R4
7. AUTHOR(s) J. D. Adams P. R. Emtage S. N. Bajpai S. H. Talisa M. R. Daniel R. W. Weinert		8. CONTRACT OR GRANT NUMBER(s) F19628-80-C-0150
9. PERFORMING ORGANIZATION NAME AND ADDRESS Westinghouse Electric Corporation 1310 Beulah Road Pittsburgh PA 15235		10. PROGRAM ELEMENT, PROJECT, TASK AREA & WORK UNIT NUMBERS 61102F 2305J529
11. CONTROLLING OFFICE NAME AND ADDRESS Rome Air Development Center (EEAC) Hanscom AFB MA 01731		12. REPORT DATE September 1983
		13. NUMBER OF PAGES 188
14. MONITORING AGENCY NAME & ADDRESS*(if different from Controlling Office)* Same		15. SECURITY CLASS. *(of this report)* UNCLASSIFIED
		15a. DECLASSIFICATION/DOWNGRADING SCHEDULE N/A

16. DISTRIBUTION STATEMENT *(of this Report)*

Same

DISTRIBUTION STATEMENT A

Approved for public release;
Distribution Unlimited

17. DISTRIBUTION STATEMENT *(of the abstract entered in Block 20, if different from Report)*

Approved for public release; distribution unlimited.

18. SUPPLEMENTARY NOTES

RADC Project Engineer: James C. Sethares, (EEAC)

19. KEY WORDS *(Continue on reverse side if necessary and identify by block number)*

Magnetostatic	Phase	Measurements	Radar
Delay	Dispersion	Angle	ECM
YIG	Epitaxial	Transducers	Arrays
Microwaves	Films	GGG	Antenna

20. ABSTRACT *(Continue on reverse side if necessary and identify by block number)*

Studies of magnetostatic wave (MSW) propagation in epitaxial yttrium iron garnet (YIG) aimed at the development of dispersive delay lines electronically variable delay lines for use in radar and ECM systems are described. Initially, the application of MSW delay lines in wide instantaneous bandwidth phased array antennas is discussed, and both dispersive and variable delay using the "up-chirp" and "down-chirp" configuration were demonstrated. Beam steering of backward-volume waves, due to a close

DD FORM 1473 EDITION OF 1 NOV 65 IS OBSOLETE
1 JAN 73

UNCLASSIFIED

proximity ground plane, was calculated and found to be significant at low wavenumbers. Theory for the transduction of surface waves by slot line and coplanar waveguide transducer was developed. Techniques to decrease the phase error, or delay ripple, in simple delay lines were investigated. These included optimized nonuniform ground plane spacings and compensation transducers. The effect of a change in bias field angle on MSW propagation was studied, and a configuration yielding an approximately constant delay which can be varied in magnitude by changing the bias field angle was found. Construction of a field probe for MSW is described and the results of measurements performed on beam steering of forward-volume waves discussed. MSW propagation and transduction in double YIG films was studied both theoretically and experimentally. Experiments were performed both on separate YIG films held close together and YIG/Sm:GGG/YIG/GGG substrate epitaxial structures.

Techniques which show the potential for achieving the performance required for systems application of MSW delay lines have been developed. The most pressing problem area is the reduction of amplitude and phase ripple arising from reflections and higher order mode interference to acceptable levels.

Accession For		
NTIS GRA&I	✓	
DTIC TAB	☐	
Unannounced	☐	
Justification		
By		
Distribution/		
Availability Codes		
Dist	Avail and/or Special	
A		

TABLE OF CONTENTS

i

LIST OF FIGURES

iii

iv

xi

LIST OF TABLES

xiii

1. INTRODUCTION

This report describes work performed in the course of a program to investigate magnetostatic wave (MSW) device techniques for phased array antennas and microwave signal processing. At the start of this program, initial experiments on variable delay[1] and also broadband linearly dispersive delay[2] using magnetostatic wave delay lines had been demonstrated. Both of these device characteristics have a potentially wide application in radar and ECM systems. However, these magnetostatic wave devices had significant phase error ($>100^\circ$) which reduced their allure. Thus, the main thrust of this program was to reduce the phase error to less than 10°, which is typically required for devices in radar and ECM systems.

Following this introduction, the basic concepts of magnetostatic wave delay lines used in phased array antennas are discussed. Because MSWs are dispersive, ideas derived from considering nondispersive delay lines require some modification, before being applied to MSW.

Single film delay lines are discussed in Section 2. Constant delay lines are briefly described and a possible technique to obtain variable delay by changing the ground plane spacing is critically examined. This technique was found to be inappropriate. Calculations on variable delay lines using presently available "up-chirp" and "down-chirp" delay lines in cascade are described, and it is concluded that sufficiently low phase errors can be obtained if the delay adjustment is restricted to <10 nS. Measurements on a variable delay line using a magnetostatic forward-volume wave (FVW) "up-chirp" and a backward-volume wave (BVW) "down-chirp" delay line are described. In these experiments the center frequency of the FVW device could be changed by an electromagnet incorporated in its bias field magnet arrangement.

Although variable delay was demonstrated, the phase errors obtained were much larger than predicted and emphasized the need to reduce amplitude and phase ripple due to reflections, higher order modes, etc. These mechanisms can cause phase ripple significantly larger than the ripple due to the MSW dispersion.

Techniques to achieve low phase error delay lines using special transducer arrangements which compensate for the nonlinear variation in MSW delay were conceived. Calculations show that these relatively simple techniques can be applied in devices for phased array antennas where the delay is <50 nS, but are not suitable for longer delays required in ECM systems. A test device was constructed and tested but e.m. feedthrough was too large, due to the extensive microstrip circuitry required, so that small phase errors due to the MSW could not be measured.

Design and construction of a BVW "down-chirp" delay line and a surface wave (SW) "up-chirp" delay line operating around 3 GHz are described. Both of these devices had differential delays of 200 nS or more, making them potentially useful in either ECM or very large phased array antenna applications. Backward-volume waves are very useful in the construction of "down-chirp" delay lines. However, the degree of control over their dispersion characteristics which can be achieved via the ground plane spacing is limited. The limitation arises since the ground plane makes the BVW "walk off." This effect is significant when $k <$ (ground plane spacing)$^{-1}$ and is discussed in detail in Section 2.6.

Magnetostatic surface waves propagating on a metallized surface of a YIG film show high group velocities with approximately linear delay with frequency characteristics. They thus have potential applications as the "up-chirp" delay line in a variable delay module. Experimental work has not been performed on this topic during this contract period, however, a theory to explain the excitation of SWs by both slot line and co-planar wave guide transducers has been derived and is described in Section 2.7.

2

A technique to achieve low phase error dispersive delay lines with FVWs is described in Section 3. Initially, the delay line was considered as composed of several different sections, each with a different ground plane spacing. The length of each section was then optimized to provide a minimum phase error over an approximately 1 GHz bandwidth. An experimental device was constructed which gave encouraging results but had large delay ripple attributed to reflections from a step between different ground plane spacings. This technique has been extended to the case of a continuous variation in ground plane spacing, and a computer program developed which calculates the coefficients of a quadratic variation in ground plane spacing. This technique predicts that phase errors of $<20^{\circ}$ can be obtained.

Propagation of magnetostatic volume waves in YIG films magnetized in an arbitrary direction is described in Section 4. Calculations and experiments were performed for two cases, a) with the bias field in the plane defined by the normal to the film and the propagation direction (FVW-BVW) and b) the plane defined by the normal to the film and the in-plane normal to the propagation direction (FVW-SW). In both cases agreement between calculations and measurement was very good. Based on this work a technique to achieve variable delay using a single delay line was developed. Variation in delay of $\pm$ 20% over an approximately 150 MHz bandwidth in X-band was achieved by varying the angle of the bias field in the FVW-BVW plane. It was necessary to adjust the bias field at each angle in order to keep the center frequency of the delay line constant.

Hitherto unexpected beam steering of FVWs was reported previously,[3] and in Section 5 work performed on measurements of this phenomena and possible explanations are described. Beam steering was felt to be a potential source of ripple in FVW delay lines and of other unexplained observations. Beam-steering measurements were performed using a co-axial probe and results obtained were qualitatively the same as those of other workers.[3] Previously, the beam steering was attributed to an in-plane component of magnetization[3]; however, we

3

were not able to find a convincing physical reason for the presence of the in-plane component in epitaxial YIG films grown on <111>-oriented gadolinium gallium garnet (GGG) substrates. Several other explanations were considered and the one which fits our experimental observations best is diffraction from the edge of the transducer.

The technical section of the report concludes with a discussion of MSW propagation in double films. First, the theory of MSW propagation and transduction in double YIG film structures is developed. Experiments performed on both epitaxially grown double film structures and arrangements of coupled single films are described, and in all cases agreement between measurements and calculations is good. Finally, the growth of YIG/Sm:GGG/YIG/GGG substrate structures is described.

1.1 Magnetostatic Wave Delay Lines in Phased Arrays

Variable magnetostatic wave delay lines are potentially useful in phased array antennas because of the wide instantaneous bandwidth obtained when real time delay, as opposed to phase shift with a limited $0-2\pi$ radians range, is used for beam steering.

One of the basic functions of control devices in a phased array antenna is to provide a planephase wavefront which propagates at an angle θ to the antenna surface. In its simplest form, this could be done by the insertion of a phase shift $\phi_n = \frac{\omega_o \ell_n \sin\theta}{v}$ in the feed to each element in the array so as to equalize the total phase shift between the signal source and the desired phasefront. This is shown in Figure 1 for the extreme elements (0 and n) in a linear array. In present phased array antennas, the absolute phase shift is not equalized but rather phase shifters, variable over a $0-2\pi$ range, are adjusted to produce a planephase front. This small phase variation can be used to steer even large arrays since contributions from individual elements will add in phase as long as their absolute phase differs only by $2n\pi$, where n is an integer. Use of $0-2\pi$ phase shifters, however, limits the instantaneous bandwidth of the array.

4
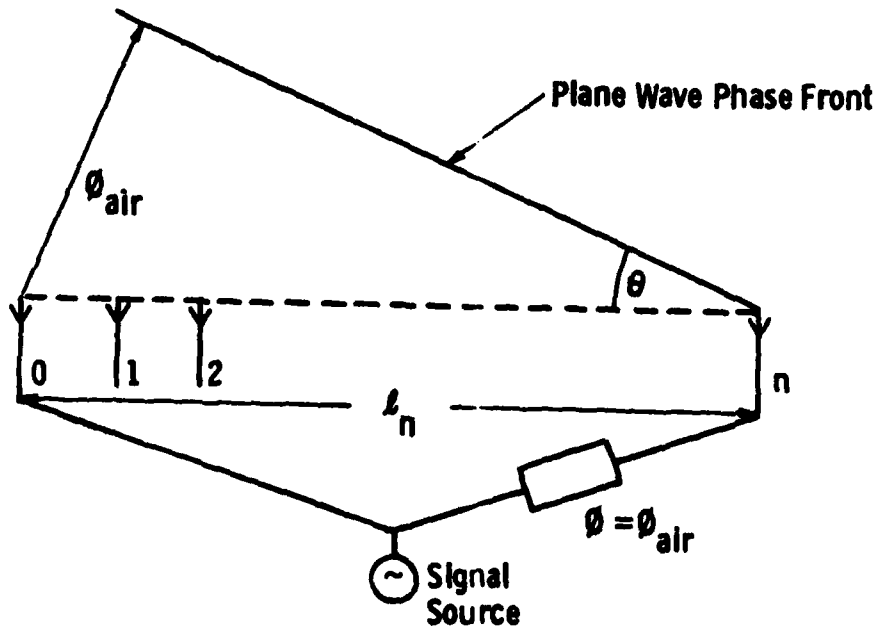
Figure 1. Plane phase-front produced by array antenna.

For operation of a phased array over a wide instantaneous frequency band, not only must the phase at each element be set to give the required beam angle at a certain frequency, say midband (ω_0), but the rate of change with frequency must be set so as to keep the beam angle constant with variations in frequency. These conditions on the required phase shift can be summarized as

$$\phi_n = \frac{\omega_o \ell_n}{V} \sin \theta \qquad\qquad [1]$$

and

$$\frac{\partial \phi_n}{\partial \omega} = \frac{\ell_n}{V} \sin \theta \qquad\qquad [2]$$

where ϕ_n is the phase shift at element n, ω is the angular frequency, ℓ_n is the distance of the element from one end of the linear array, V is the velocity of light in air, and θ is the beam-pointing angle.

Obviously, the conditions given in Equations 1 and 2 are satisfied simultaneously by a nondispersive delay line, i.e., a delay line in which the phase velocity and group velocity are equal and invariant with frequency. However, magnetostatic wave delay lines are dispersive, as are lumped-constant, stripline, and folded-tape-meander delay lines. Here, dispersive means that the phase velocities and group velocities are not equal and, in the context of Equations 1 and 2,

$$\frac{\phi_n}{\omega} \neq \frac{\partial \phi_n}{\partial \omega} \, .$$

The variation of phase shift with frequency for an ideal nondispersive variable delay line and a magnetostatic wave variable delay line is shown in Figure 2. In this figure, 1, 2, and 3 refer to three different bias field values for delay line characteristics with the same group delay, i.e., $\partial \phi/\partial \omega$. Note that the phase shift of the MSW does not extrapolate to zero at zero frequency.

This implies that if the <u>absolute</u> phase at midband is set using a dispersive delay line to produce a beam angle θ, then any change in

6

Phase
Shift
Φ

1
2
3

1
2
3
} MSW
Variable
Delay
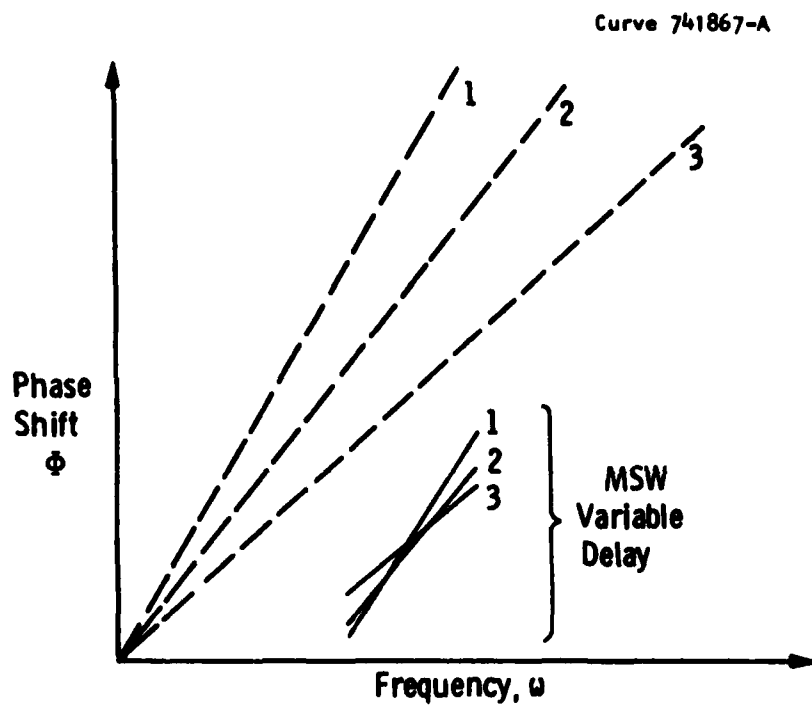
Frequency, ω

Figure 2.   Schematic plot of phase shift versus frequency for ideal
phase shifter (---) and phase shift produced by MSW delay
lines (___). Note that the phase shift from the MSW variable
delay line does not extrapolate to zero at zero frequency.

7

frequency will result in a change in θ. However, since absolute phase shift cannot be distinguished from $\phi - 2n\pi$, then it may be possible to adjust the phase shift of the MSW delay line to a suitable value of $\phi - 2n\pi$ at midband. Then, providing the group delay is simultaneously adjusted to the correct value, the beam will be steered in the desired direction, i.e., the delay line is adjusted so that ϕ_n and $\frac{\partial \phi_n}{\partial \omega}$ are set to the required values simultaneously. This may necessitate bias field control of both "up-chirp" and "down-chirp" delay lines if this technique is used to achieve variable delay. Alternatively, it will be possible to use a variable dispersive delay line, e.g., a magnetostatic wave device and a $0-2\pi$ phase shifter as shown in Figure 3. Here, the phase shifter trims the total phase shift to give the desired beam angle (θ) at midband with the delay line adjusted so that

$$\frac{\partial \phi_n}{\partial \omega} = \frac{\ell_n}{V} \sin \theta .$$

The necessary phase shift could be integrated with the GaAs power amplifier in an active aperture array. If, however, the delay lines are used to feed subarrays, as shown in Figure 4, then the dispersive nature of the magnetostatic wave delay line does not introduce an increase in component count.

8
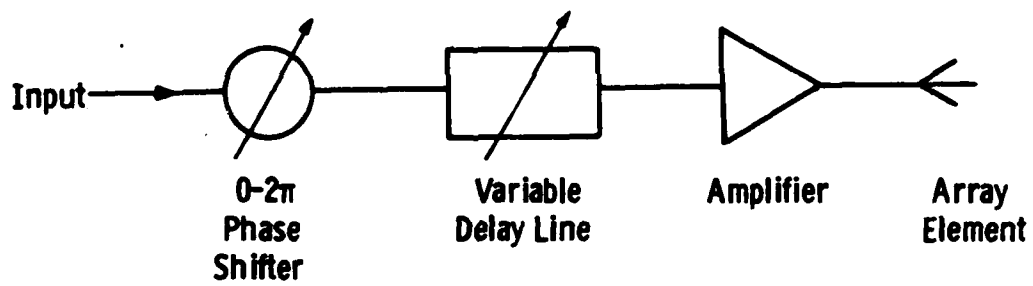
Figure 3. Phase control for antenna element using an MSW variable delay
line plus a phase shifter.

Dwg. 7754A03
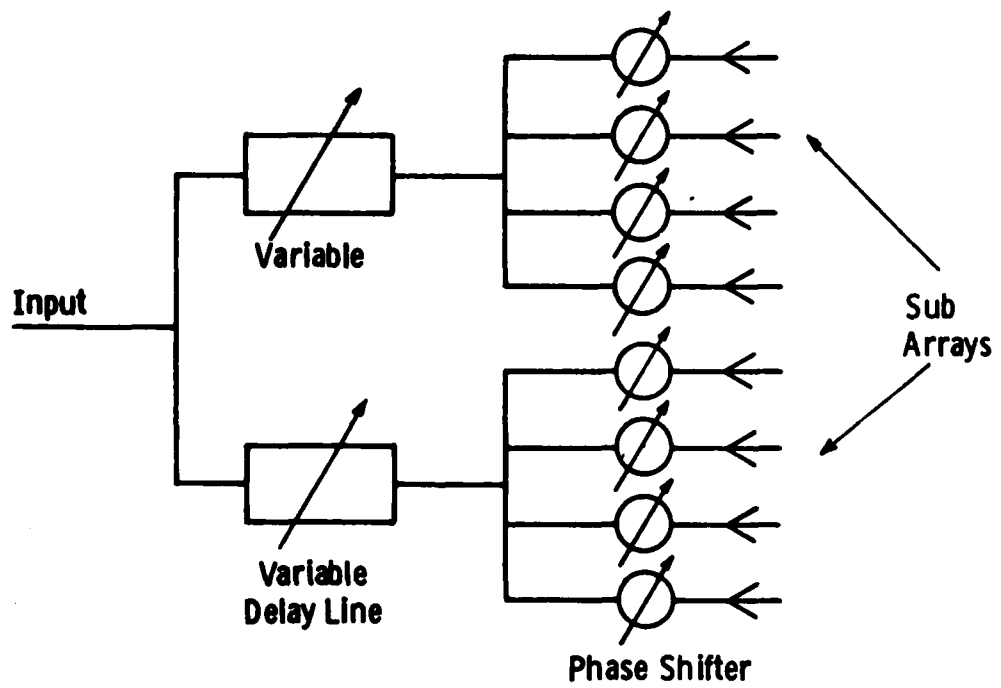
Figure 4. Phase control using an MSW variable delay line in an antenna
with subarrays.

10

2. SINGLE FILM DELAY LINES

2.1 Constant Delay

Previously reported work[2,4] has shown how the presence of a
close proximity ground plane to a yttrium iron garnet (YIG) film may
usefully modify the magnetostatic dispersion characteristics (Figure 5).
In fact, all three types of magnetostatic wave can be so influenced by the
ground plane to give useful ranges of constant delay[5,6] over bandwidths
from 200 to 500 MHz. Contant delay means constant to within 1 to 5%. In
practice, a necessarily finite conductivity ground plane does cause some
attenuation of the magnetostatic wave[7] due to eddy current damping.
However, this attenuation was generally found to be an acceptable price to
pay for the simplicity of the technique -- single film plus ground plane
-- in most parameter ranges. There are in any practical device always two
ground planes. Frequently, the second ground plane is the delay line box
lid or the metallization on an alumina substrate supporting the microstrip
feedlines and transducers. These second ground planes are usually at
least ten times further removed from the YIG film compared to the spacing
of that plane specifically designed to influence the MSW dispersion
characteristics. In these cases the influence of this second plane can be
readily ignored.

One of the aims of this program was to develop techniques to
obtain electronically variable delay. The ground plane spacing from the
YIG film was a possible parameter to achieve this aim. Unfortunately,
calculations performed under this contract failed to yield a way of
adjusting the constant delay region by control of the ground plane
spacing. This spacing from a YIG film changed the delay characteristic
but not in a useful way. This is illustrated in Figure 6a for forward-
volume waves (FVWs). A ground plane spacing (t) of 150 microns from a 20

11

Figure 5. A basic magnetostatic delay line configuration.

micron film gave a region of constant delay over about 400 MHz. The
second ground plane spaced (s) at 0.55 mm maximized this constant delay
range.[6] Changing t to 100 microns did not move this constant delay
region either up or down, but distorted it. A not so drastic but similar
situation was found for backward-volume waves (BVWs; Figure 6b). Thus,
the single film plus ground plane could be made to yield a constant delay,
but this delay was not readily adjustable through a parameter such as the
ground plane spacing.

2.2 "Up-Chirp" and "Down-Chirp" Calculations

A suitable ground plane spacing could also be chosen to yield a
region of linear delay variation.[2] If a BVW delay line was employed in
series with either a FVW or a surface wave (SW) line, then a constant
delay resulted. Additionally, the constant delay was adjustable[1] if one
of the delay line responses was made to slide along the frequency axis,
e.g., by adjusting the static bias field on one of the delay lines. For a
constant total delay, the delay-versus-frequency slopes of each device
must be numerically equal as shown in Figure 7. Figure 8a gives the
results of a calculation of the constant delay achievable over a 200 MHz
bandwidth at X-band and shows how the delay could be increased or
decreased by varying the bias field on the FVW delay line. A figure of
merit for the constancy of the delay is the phase deviation from linearity
over the operating bandwith. A calculation of this for the curves of
Figure 8a is shown in Figure 8b. This deviation is too large for curves
(a) and (c) to be of practical value in, e.g., a phased array radar
antenna, particularly curve (a). It results primarily from the large
absolute delay of about 270 nS of the combined delay lines. Smaller phase
deviation could be obtained using delay lines with shorter time delay. If
a sacrifice in bandwidth was made, then the phase error could be reduced
to ± 3° over the frequency range 9.50 to 9.65 GHz, and this ± 3° error
could be maintained over a delay range adjustment of ± 5 nS, i.e., from
258 to 268 nS [curves (b) and (c) of Figure 8a]. This 150 MHz bandwidth
translates to a 135 MHz bandwidth at 3 GHz. The necessary adjustment in
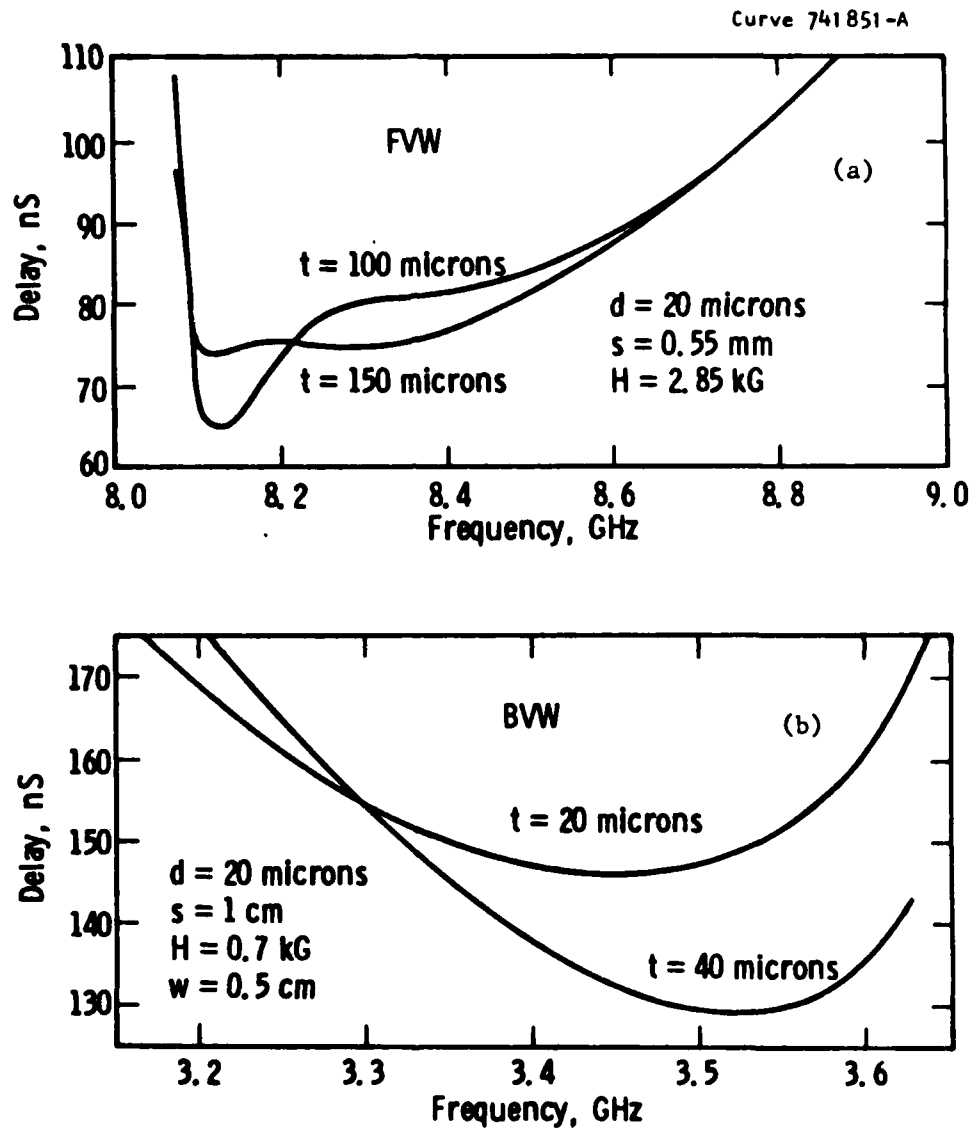
Figure 6. (a) Delay versus frequency for a FVW with a ground plane at 0.55 mm and a second one at the respective positions ot 100 and 150 microns. (b) Delay versus frequency for a BVW with a ground plane at 1 cm and a second one at the respective positions of 20 and 40 microns.
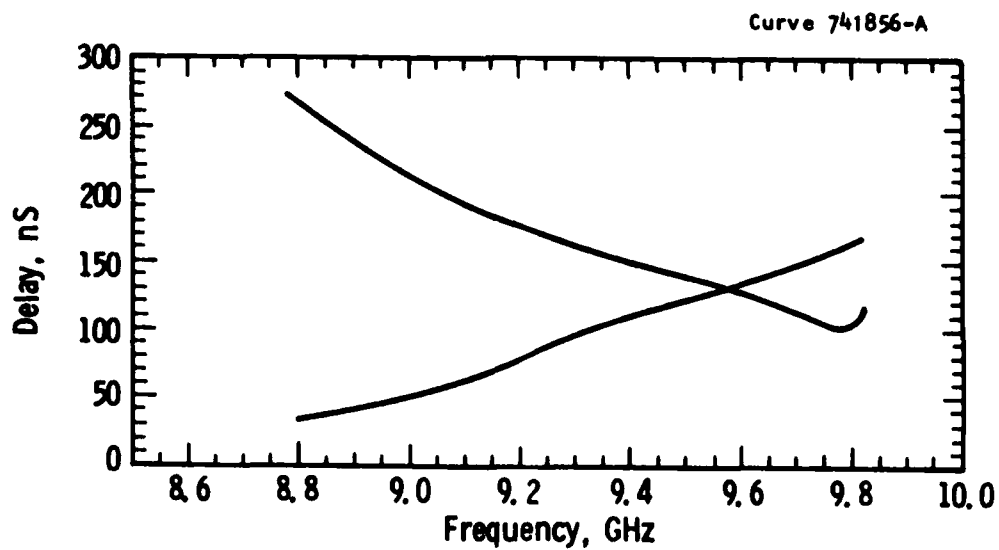
Figure 7. Computed delay versus frequency for a FVW "up-chirp" and a BVW "down-chirp" with numerically equal average slopes over the range 9 to 9.8 GHz. FVW curve: 26.4 μm film thickness; 26.4 μm ground plane spacing; 3071 Gauss bias field. BVW curve: 15 μm film thickness; 150 μm ground plane spacing; 2750 Gauss bias field.
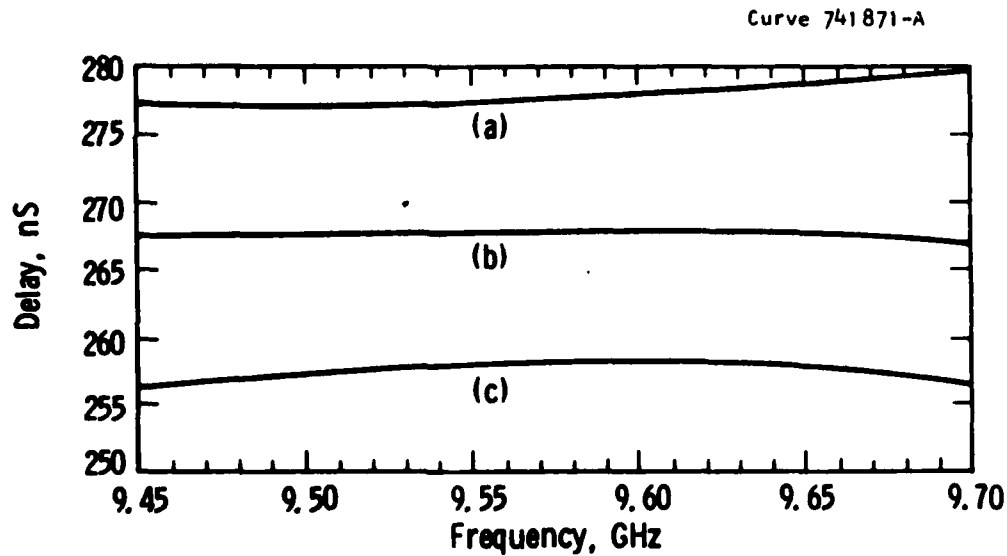
Figure 8a. Combined delay versus frequency from the curves of Figure 7 with equalized average slopes over the range 9.47 to 9.68 GHz; (a) FVW bias field 3041 Gauss, (b) 3071 Gauss, (c) 3101 Gauss; FVW pathlength 1 cm; BVW pathlength 1.072 cm.
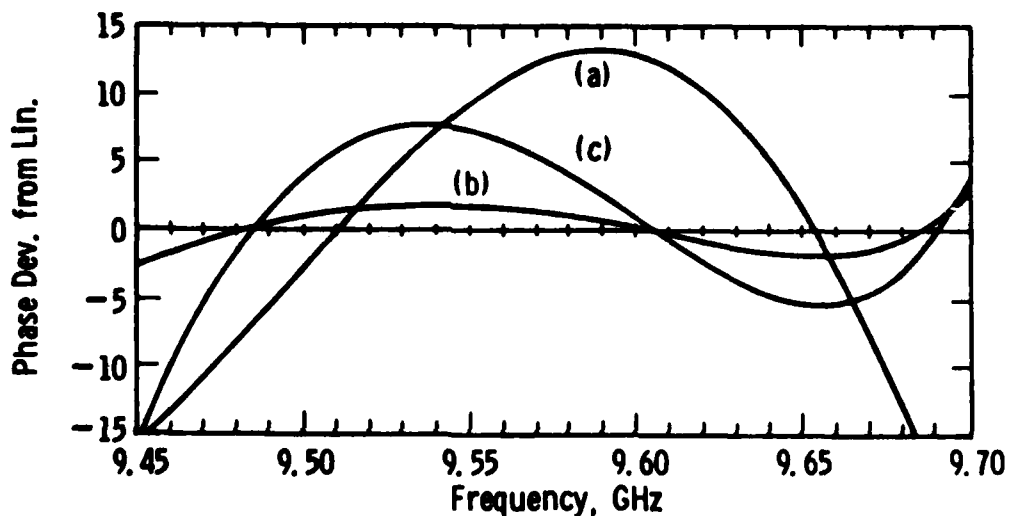
Figure 8b. Phase deviation from linearity versus frequency for the curves of Figure 8a with respect to a least-squares-fitted phase function for each curve in Figure 8a.
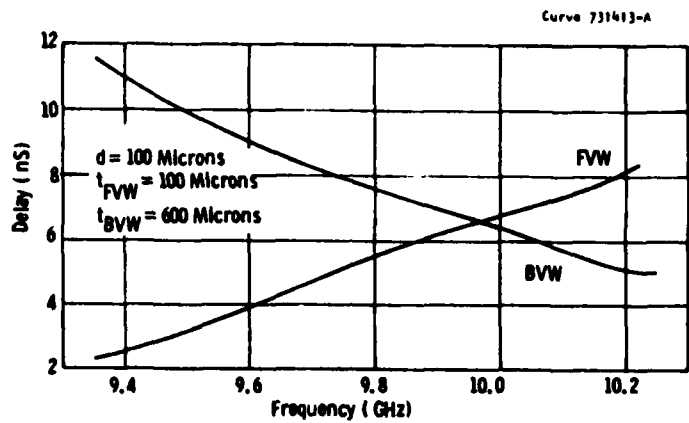
Figure 9a. Delay versus frequency for FVW and BVW delay line designed for
            an optimum degree of delay linearity by the ground plane
            spacings (t). The delay slopes are numerically equalized by
            having a FVW pathlength of 2 mm and BVW pathlength of
            3.28 mm.
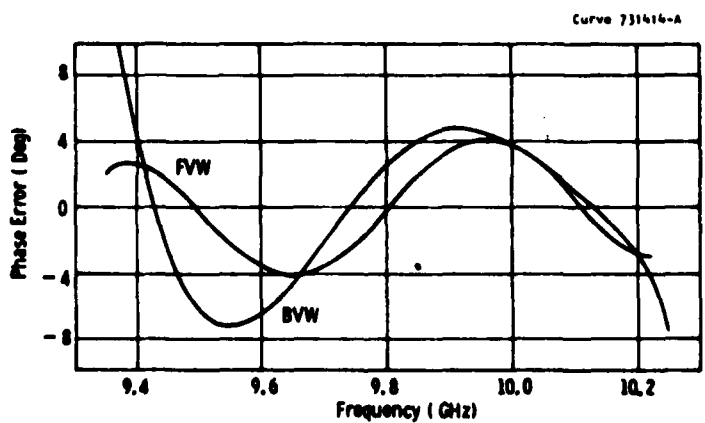
Figure 9b. Phase error or phase deviation from a quadratic function
            versus frequency for the above delay curves of Figure 9a.

17

the static bias field of the "up-chirp" delay to get the ± 5 nS shift is
only ± 15 Gauss in about 5000 Gauss of external field at X-band.

One potential application of MSW variable delay lines is in air-
borne radar. For example, an X-band radar for use in a fighter aircraft
may have an antenna in the approximate shape of an ellipse, the major
and minor axes of which measure about 90 cm and 50 cm, respectively.
This antenna could have more than 500 radiating elements with the phase
to each element preset to achieve a desired radiation pattern and to
have steering of the radiated beam accomplished mechanically. In fact,
beam steering could be achieved electronically over a ± 60° angle by MSW
delay lines which had no more than a ± 2.7 nS adjustable delay at X-
band. With these numbers in mind, it was interesting to ask what could
be achieved in terms of phase error using presently available FVW and
BVW delay line characteristics. To produce short delays (~10 nS)
requires a combination of thick YIG films and short pathlengths for the
magnetostatic waves. Figure 9a shows the calculated delay versus
frequency for 100 μm thick YIG films supporting either an FVW or a BVW
over a 2 mm and 3.28 mm pathlength, respectively. The different path-
lengths ensure the delay slopes are numerically equal. In Figure 9b the
phase error versus frequency is plotted for the two curves of Figure 9a.
The FVW results show a maximum phase error of ± 4° over the full 900 MHz
bandwidth. If attention is confined to the interval 9.75 GHz to 10.2
GHz, the BVW results also lie within a ± 4° band. With the parameters
used here, such a device would have a 450 MHz bandwidth at X-band with a
total delay adjustment of approximately 10 to 15 nS. This adjustment
would be obtained by sweeping the FVW curve of Figure 9a parallel to the
frequency axis over a 450 MHz range. The total phase error would not
exceed ± 8° under these conditions. This is an encouraging result
because it has been achieved without using any phase error compensation
technique. With compensation techniques to be described later, it may
be possible to reduce the phase error to ± 2°.

18

2.3 "Up-Chirp" and "Down-Chirp" Measurements

An experimental adjustable delay line has been reported[1] using a BVW delay line in series with a SW line. The device operated at S-band and displayed a constant-but-adjustable delay from about 165 to 185 nS over a 250 MHz bandwidth. Curiously, the SW delay line had parameters which would have guaranteed its delay to be far from an optimum degree of linearity based on experience reported here. A similar adjustable delay line was fabricated on this program which used a BVW delay line in series with a FVW one. It was decided to use a FVW "up-chirp" filter instead of the SW filter and obtain improved bandwidth as a result.

Delay calculations were performed for single 54 micron thick YIG films grown epitaxially on GGG. Delay linearity was optimized by placing a single ground plane 54 microns from the YIG film for the FVW device and 400 microns for the BVW device. The two slopes were respectively calculated as 93 nS/GHz/cm and -68 nS/GHz/cm and, in order to equalize them numerically, the FVW delay line was designed to have a pathlength of 7.33 mm and the BVW delay line a 10 mm pathlength. The 54 micron spacing was achieved by grinding down a piece of Corning 7059 glass optically cemented to a gold-plated commercial alumina substrate. The 54 micron glass spacer then formed a dielectric spacer on which the microstrip feeds, and transducers were fabricated using conventional photolithography. For the 400 micron spacer, a conventional 25 mil alumina substrate was thinned down to 16 mils by grinding, and then microstrip feeds and transducers were defined photolithographically in 5 micron gold film. The transducers were 50 μm wide over a 5 mm length equal to the YIG width. They were then extended beyond the YIG as 50 ohm microstrip lines to have an overall electrical length of one quarter wavelength at midband measured from the open circuited end to the YIG midpoint. This ensured a microstrip current maximum at the center of the YIG sample. The YIG samples were cut from a 2-inch diameter wafer and measured 25 mm by 5 mm. Each was bevelled to 1° at the ends as an aid to suppressing MSW reflections.

19

The static bias fields were provided by Sm-Co magnets. For the
FVW delay line, a conventional-type yoke machined from low-carbon steel
surrounded these magnets and gave a 3 mm airgap for the device. The
typical field profile for this type of structure is shown in Figure 10.
Over the active region of the YIG film, the field was uniform to about
0.1%. The BVW delay line was a more difficult design because the
magnetic field must run parallel to the YIG film. The solution was to
use only Sm-Co magnets with no yoke and magnetized on their small or end
faces, as shown in Figure 11. Field calculations showed that for a
given thickness of magnet there was optimum separation of the polepieces
to give a maximum field uniformity over the YIG active region. In
Figure 11 the 25 mm square magnets gave a field uniformity of 1% over a
1 cm pathlength along the long axis of the YIG sample. Transverse to
the long axis, the field uniformity was about 1.5% across the 5 mm width
of the sample. The delay adjustment was readily achieved by winding
bias coils on the yoke of the permanent magnet assembly for the FVW "up-
chirp" delay line in Figure 10. A dc current through these coils could
shift the net bias field on the YIG film either up or down about the
fixed value of 2.5 kG provided by the Sm-Co permanent-magnet polepieces
and yoke assembly.

Initial transmission measurements on both delay lines showed
substantial interference from reflected triple-transit signals. The
bevelled sample ends were not sufficient to suppress these.
Additionally, the steep fall-off in magnetic field immediately beyond
the transducers in the BVW device was certain to have caused reflections
of the bidirectional waves. Fortunately, considerable improvement was
achieved by evaporating a thin (~500Å) Al film on each end of the YIG
films and extending up almost to where the transducers contacted the
films. These Al films acted as areas of ohmic loss for the MSWs. The
completed delay lines are shown in Figure 12. The bias coils on the FVW
delay lines are clearly visible. These coils had a sufficient number of
turns on them to cause a 500 MHz shift in the operating frequency of the
delay line when fed by a dc current of ≃1A.
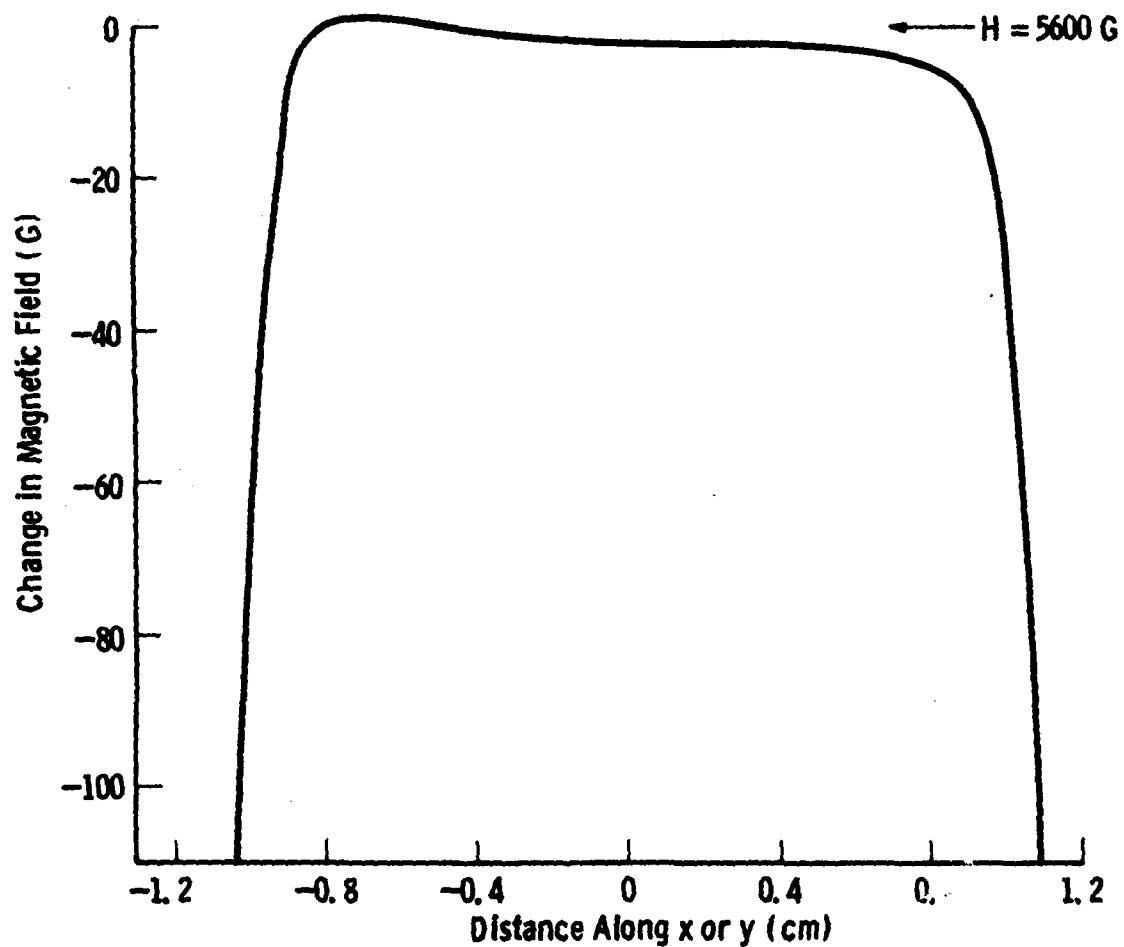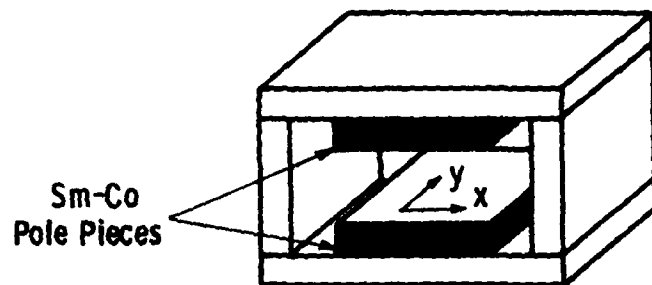
Figure 10.   Magnetic-field profile in the horizontal mid-plane of the
             3 mm air gap for the FVW permanent magnet shown in the
             sketch.

21
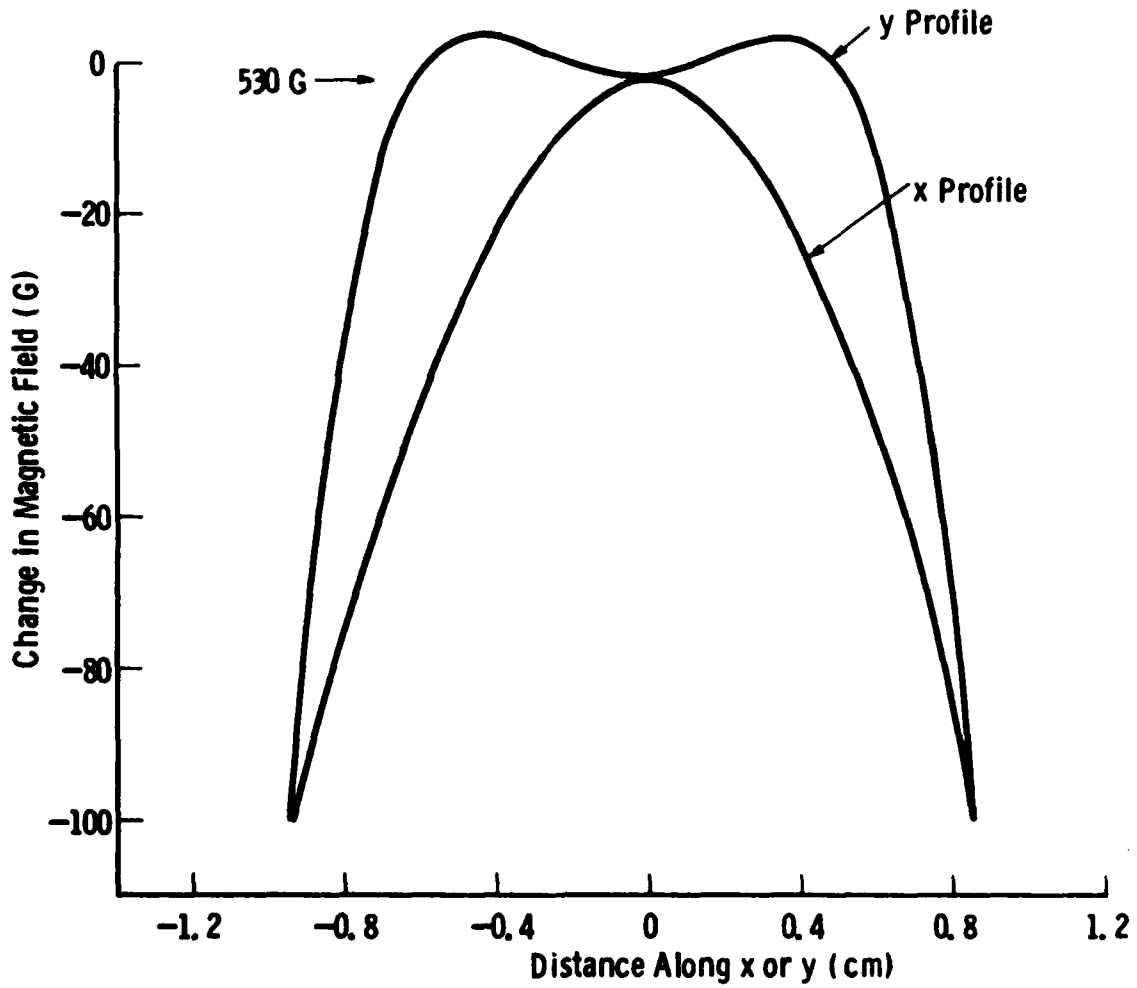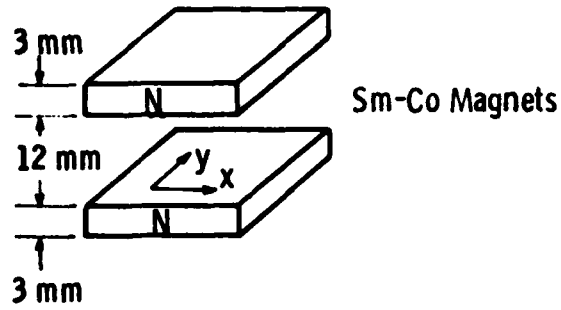
Figure 11. Magnetic-field profiles in the horizontal mid-plane of the 12 mm air gap for the BVW permanent magnet shown in the gap.
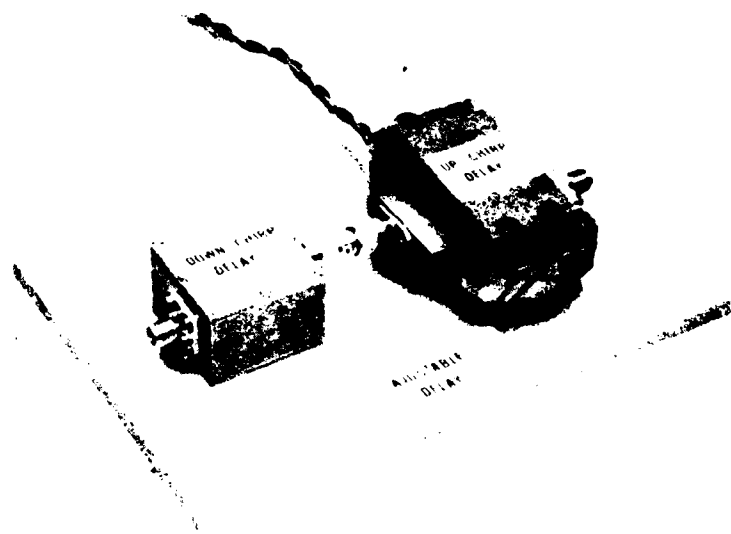
Figure 12. Photograph of the assembled constant-but-adjustable delay line module. The bias coils for adjusting the FVW delay line element are visible on the magnet yoke structure.

23

Curve 730417-A
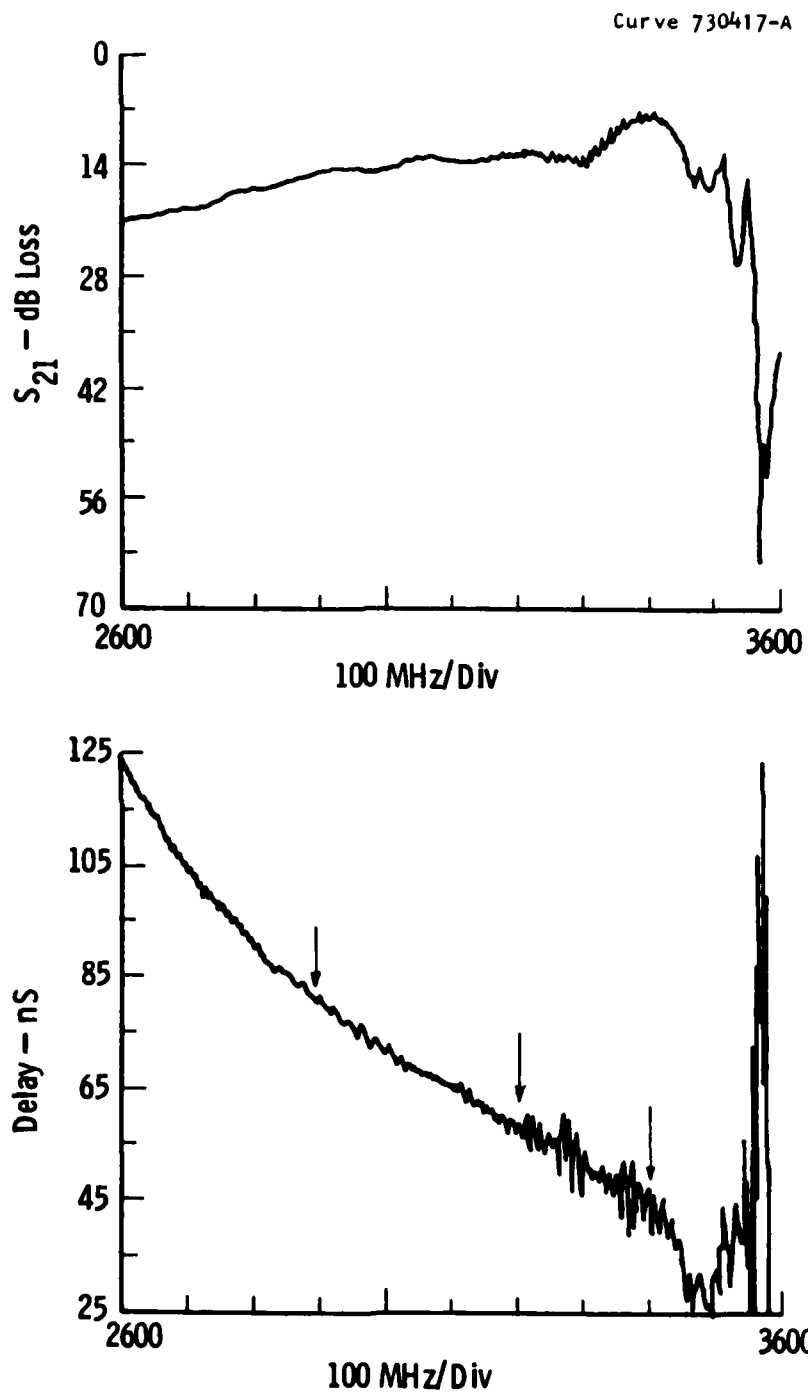
Figure 13. Upper curve: Transmission loss versus frequency for the BVW delay line over part of its bandwidth.
Lower curve: Delay versus frequency for the same delay line.

24

The transmission loss (S_{12}) and delay versus frequency are shown
for the BVW device in Figure 13. The transmission loss is quite smooth
and ripple-free except in the vicinity of the band edge at 3.55 GHz.
The delay results reflect this performance. The 400 micron ground plane
spacing has ensured a fairly linear group delay from about 3.5 to
2.9 GHz. However, residual transmission loss ripple limits the useful
delay region from 3.2 GHz to 2.9 GHz. The mean slope of the delay curve
between 3.5 GHz and 2.9 GHz is 71 nS/GHz, a figure quite close to the
calculated value of 68 nS/GHz. Figure 14 shows the corresponding S_{12}
and delay values for the FVW device. The delay curve has more ripple
than the BVW delay line and S_{12} shows a greater loss value. The mean
slope of the delay curve is 64 nS/GHz over the frequency range 2.5 to
3.0 GHz. The reason the two slopes of 71 and 64 nS/GHz were not closer
to the calculated value of 68 nS/GHz is believed to be due to experi-
mental tolerances in assembling the delay lines, particularly the FVW
delay line with its close ground plane spacing requirement. Just what
would be an ultimate attainable degree of accuracy has not been
studied. But at least the above two measured numbers could be corrected
by redesigning the transducer separation to equalize the delay slopes.
Thus, the total delay was not quite constant since the two delay slopes
were not equal. Figure 15 shows the combined performances over a 400
MHz bandwidth. An approximately constant delay was obtained and it was
adjustable by varying the FVW bias field. However, delay ripple was
clearly a problem and ways of minimizing it are of prime importance.
Future work will have to address this problem.

2.4 Delay Error Compensation

An ideal linear dispersive delay line would have a delay versus
frequency curve with no delay deviation or delay error from a straight
line; expressed otherwise, there would be no phase deviation or phase
error from a quadratic variation. Presently, simple MSW delay lines
using either single films and a uniform ground plane spacing or double
YIG films still show a residual delay ripple even after they have been

25
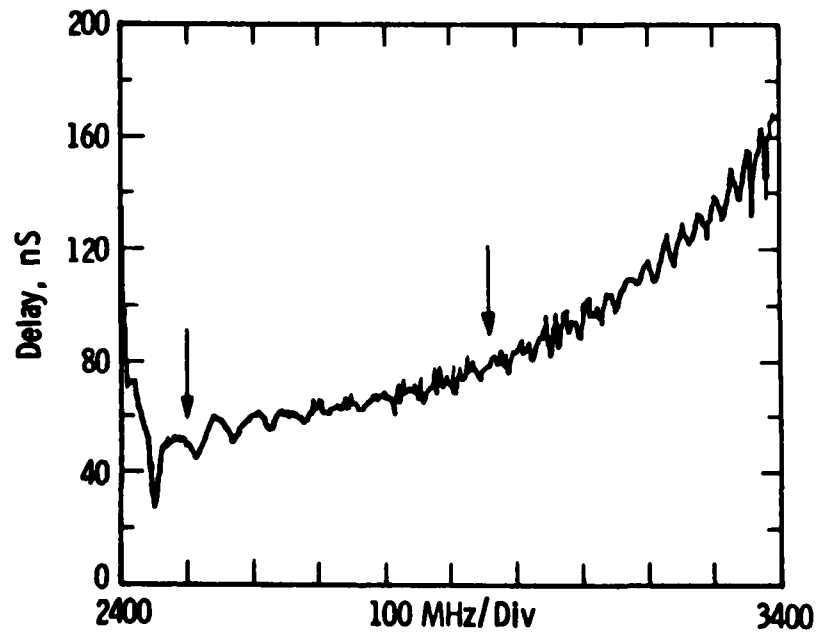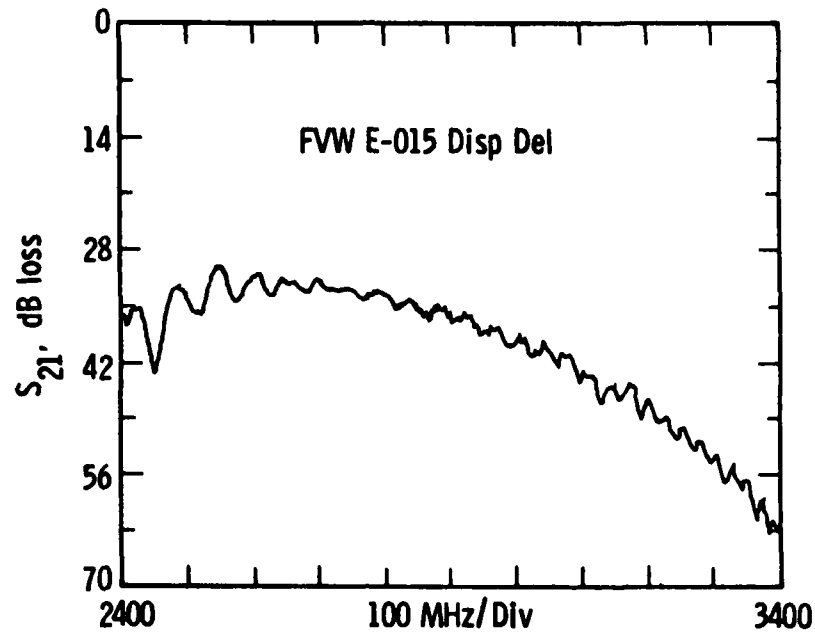
Figure 14. Upper curve: Transmission loss versus frequency for the FVW
delay line over part of its bandwidth.
Lower curve: Delay versus frequency for the same delay line.

26
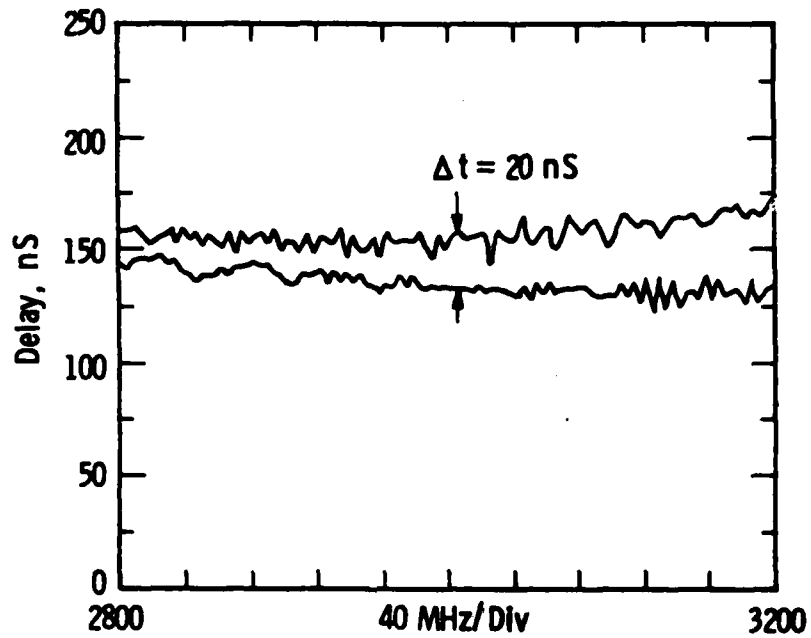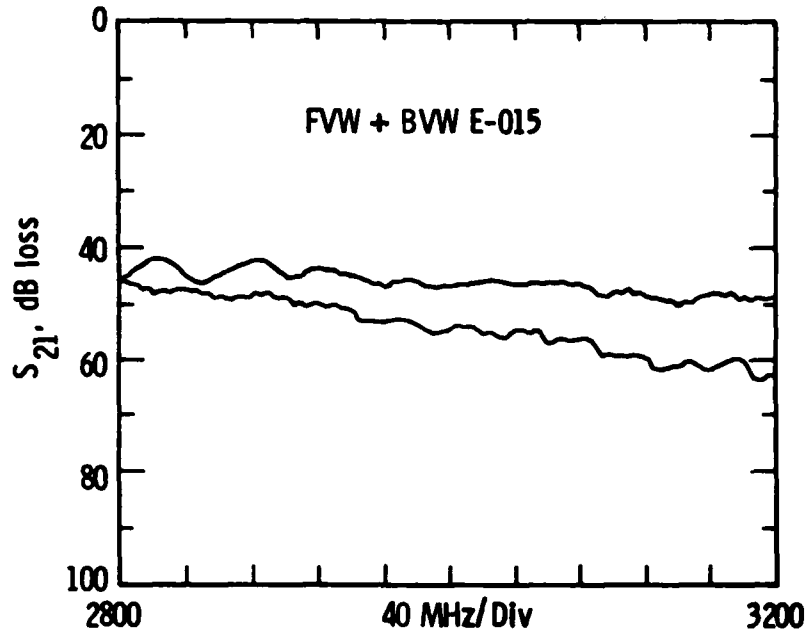
Figure 15. Upper curve: Transmission loss versus frequency for the combined FVW and BVW delay lines at 2 bias field values on the FVW delay line.

Lower curve: The corresponding delay versus frequency for the combined delay lines at the 2 bias field values.

27

optimized for a linear delay variation. It is intrinsic to the MSW and takes the form of a slow W- or S-type variation superposed on the nominally linear delay. It can in principle be compensated for by the use of multiple transducers over most of the useful bandwidth in a delay line. One approach is illustrated in Figure 16, whereby an array consisting of a combined bar and interdigital transducer for the transmitter and receiver has a delay variation approximately opposite in sign to the delay deviation of the basic delay line with single finger transducers. An analysis based on regarding each finger as a launcher or receiver of MSWs of the form αe^{ikx} is easy to implement. Reflections between fingers are neglected, α is an amplitude weighting factor for a wave of wavevector k propagating in the +x direction. Thus, the response (R) of the transducers in Figure 16 can be written:

$$R = e^{ikL} \left(\alpha_1^2 \, e^{i2k(\ell_1 + \ell_2)} + \alpha_2^2 \, e^{i2k\ell_2} + \alpha_3^2 + 2\alpha_1\alpha_2 e^{ik(\ell_1 + 2\ell_2)} \right.$$

$$\left. + 2\alpha_1\alpha_3 \, e^{ik(\ell_1 + \ell_2)} + 2\alpha_2\alpha_3 \, e^{ik\ell_2} \right)$$

[3]

where, in particular, $\alpha_1 = +1/2$, $\alpha_2 = +1$, $\alpha_3 = -1/2$ for the bar and interdigital combination. L is the separation of the inner or $-1/2$ amplitude transducers and typically $L \sim 1$ cm and is $\gg \ell_1$ or ℓ_2. (The response has a phase Φ given by

$$\Phi = kL + \phi \qquad [4]$$

where $\phi = \tan^{-1}(B/A)$ and A and B are, respectively, the sum of the real and imaginary contributions in Equation 3.) Therefore, the actual delay (g) is given by

$$g = 1/2\pi \;\; \partial\Phi/\partial f \;\; = 1/2\pi \;\; \partial k/\partial f (L + \partial\phi/\partial k) = g_0 + \Delta g,$$

28
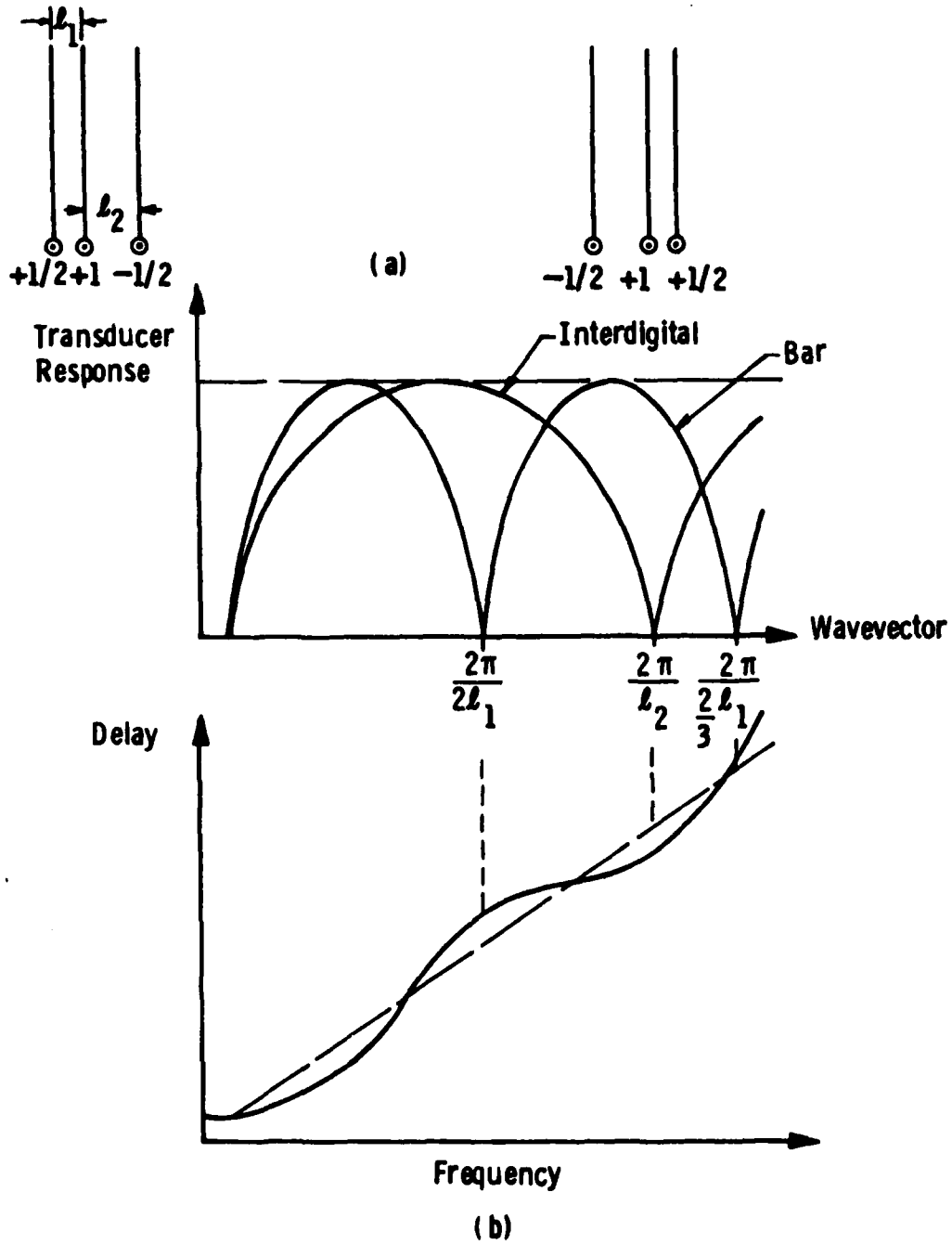
Figure 16. Combined bar and interdigital transducers (a) to produce
delay compensation for a typical quasilinear magnetostatic
wave delay function (b).

where g_o is the intrinsic group delay in the absence of any correction Δg from the multiple transducers.

As an example of what might be expected by way of phase error improvement, Figure 17 shows the results of a calculation for a 50 μm YIG film optimally spaced 50 μm from a ground plane to give a quasi-linear delay for FVWs. It was found initially that two sets of transducers overcompensated the delay ripple and one set with a single finger receiver transducer was sufficient. In Figure 17 the phase error has been reduced from about $\pm 30^{\circ}$ to about $\pm 12^{\circ}$ by this approach except at the band edges -- below 2.7 GHz or above 3.2 GHz.

A second approach to error compensation uses transducers with a unidirectional characteristic which gives an added bonus of compensating for the usual 3 dB loss of bidirectional FVW and BVW transducers. Figure 18 shows a two-finger transmitter transducer feeding two-finger receiver transducers on either side of it. One finger of each pair requires an appropriate 90° phase shift in the microwave drive current with which it is fed. Proceeding as before, the amplitudes from each of the receiver pairs is summed to give:

$$R = e^{ikL} \left(\alpha_1^2 \{e^{i2k\ell} + e^{ik\delta}\} - d_2^2 \{1 + e^{i(2k\ell + k\delta)}\} \right.$$
$$\left. + 2\alpha_1\alpha_2 \, e^{i(k\ell + \pi/2)}\{1 + e^{ik\delta}\} \right) \tag{5}$$

In Figure 18, $\alpha_1 = \alpha_2 = 1$ and δ is the difference in pathlength between the + and - waves, i.e., the + wave travels a distance L and the -wave a distance $L + \delta$. Delay compensation occurs because of this small difference. Equation 3 applied to Figure 18 reduces to a simplified form:

$$R = 4i \, e^{ik(L + \ell + \delta/2)}\left(\cos \frac{k\delta}{2} - i \sin \frac{k\delta}{2} \sin k\ell\right) \tag{6}$$

30

Curve 731412-A
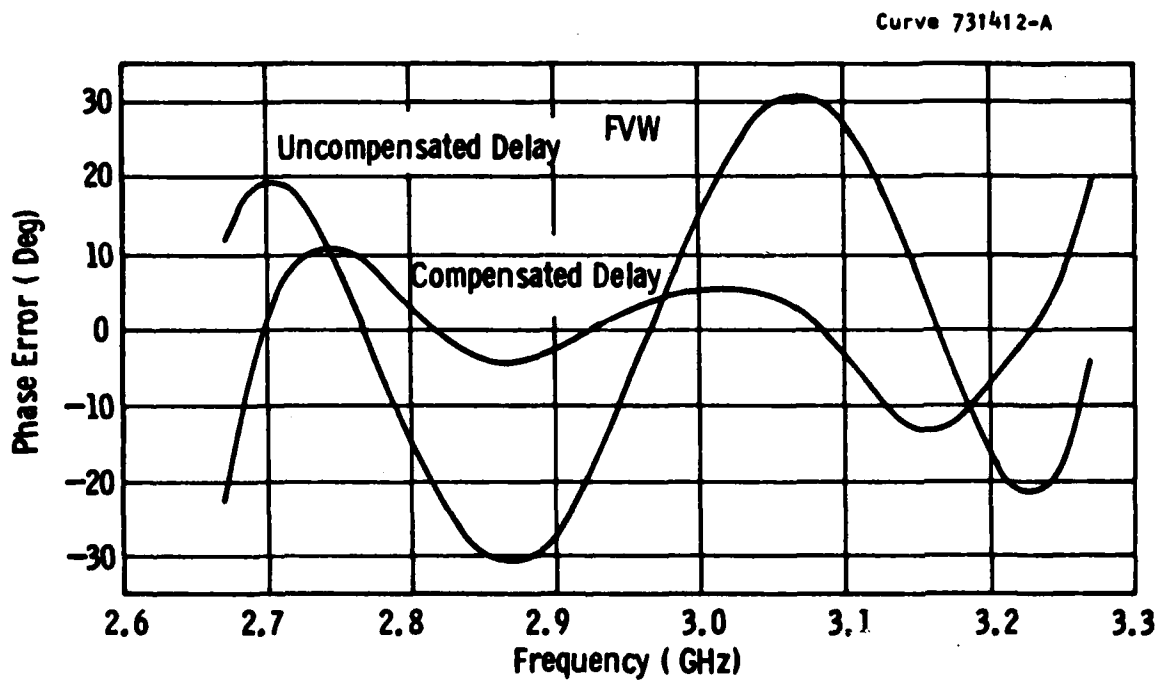
Figure 17. Phase error versus frequency for a 50 μm YIG film spaced
50 μm from a ground plane. The compensated delay curve
employed a bar-interdigital transducer combination as a
transmitter and a single-finger receiver.

31
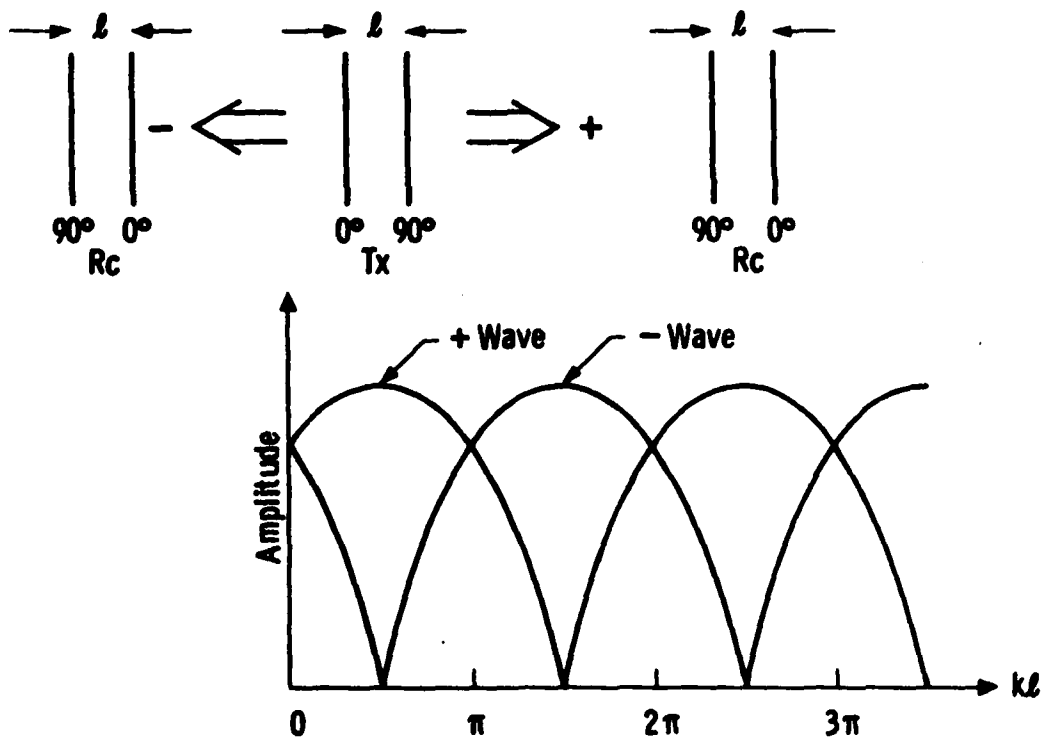
Figure 18. Use of unidirectional transducers to recover all bidirectionality loss and simultaneously compensate for delay ripple.

32

Figure 19 is an example of this unidirectional transducer approach applied to a BVW dispersive delay line. A 50 μm YIG film spaced 400 μm from a ground plane gives a region of quasilinear delay with a maximum delay error of 0.3 nS. The unidirectional transducer compensation reduces this to about 0.1 nS over most of the band, 2.9 to 3.2 GHz in the calculated example.

A transducer assembly to achieve these aims was designed and fabricated. Figure 20 is a photograph of the photolithographic mask used to generate the pattern. Each transducer pair has one member with a 90° phase shift and each pair is fed or combined by a Wilkinson combiner. This combiner provides about 20 dB of coupling isolation between each member of a pair. The 100 ohm resistors were subminiature discrete components bonded onto the microstrip after fabrication. In order for the assembly to work as required, care had to be taken to ensure the correct phasing sense of each pair. Prior to fabrication, the whole microstrip circuit was analyzed with the aid of SUPER-COMPACT[8] for correct electrical performance.

Initial measurements with a 50 μm YIG film on a 400 μm alumina substrate have been disappointing due to a high level of extraneous rf feedthrough. Much time was spent in the design stage trying to minimize the required "real estate" for the microstrip, but it could not be squeezed onto anything smaller than a 2 inch x 1 inch commercial substrate for S-band operation. Electrical cross-coupling due to the close proximity of some of the transmitter circuitry to the receiver circuitry may be causing problems. Present measurements of S_{11} or S_{22} give a confusing picture that strongly hints at a moderate to severe rf feedthrough or rf cross-coupling problem.

Utilizing the experience gained above, a second delay-correcting transducer has been designed using the interdigital-bar approach for FVWs. The photolithographic mask for this is shown in Figure 21. By going to X-band operation, the transducer overall length has been shortened and in this way there is improved separation between input and

33
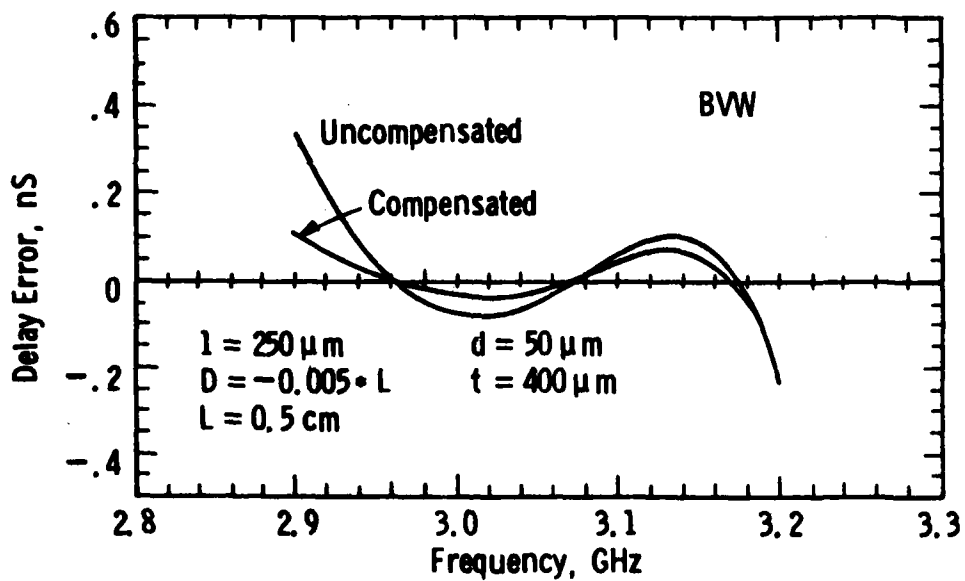
Figure 19. Calculated delay error for uncompensated and unidirectional compensated transducers versus frequency. Film thickness, 50 μm; ground plane spacing, 400 μm; unidirectional transducer pair separation, 250 μm; transmitter-receiver separation, 0.5 cm; D = differential path difference between transmitter and the two receivers.
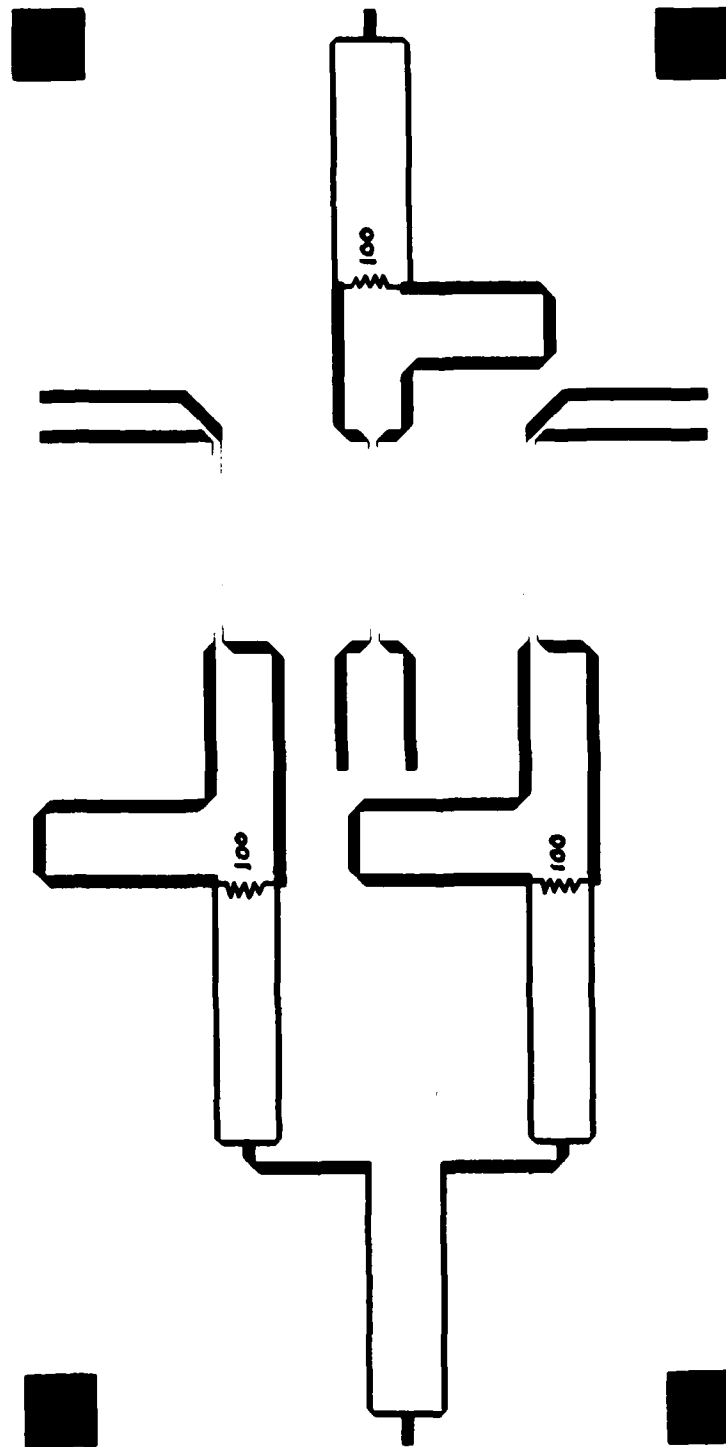
Figure 20. Magnified drawing of the photolithographic mask used for
fabricating the unidirectional transducers and also showing
the location of the discrete 100 ohm resistors for the
Wilkinson combiners.

35
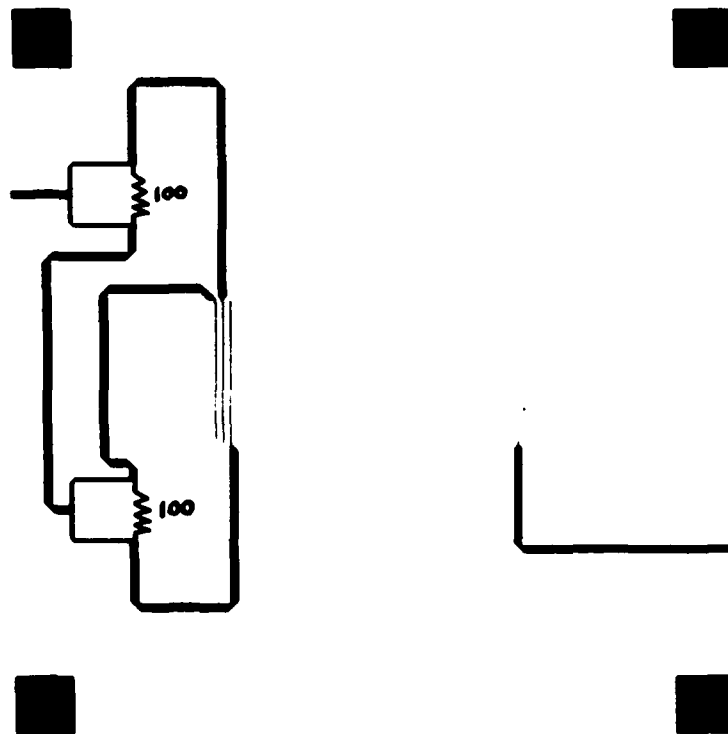
Figure 21. Magnified drawing of the photolithographic mask used for
fabricating the delay error-compensating transducer. Also
shown are the location of the 100 ohm discrete resistors
used for the Wilkinson combiners.

output transducers compared to Figure 20. Thus, the isolation between ports should be improved when metal walls are made as part of the delay line box, and they will be midway between the ports and extend up to the YIG sample. The fabrication technique will use commercial 10 mil thick sapphire on which to define the microstrip circuitry in 5 μm gold. A 50 μm thick YIG-film sample measuring 25 mm by 5 mm will then be glued face down on the sapphire with optical cement. The GGG epitaxial layer above the YIG will then be ground down to 50 μm thickness and the ground surface then metallized in Au. In this way a quasilinear FVW dispersive delay line will result with delay correction provided by the interdigital-bar trrnsducer combination. At this time the device has yet to be completed. Note that the predicted delay errors are very small and for this reason other sources of delay ripple such as rf feedthrough, reflections, etc. must be minimized, otherwise they will dominate the measured results.

2.5 Low Phase Error Dispersive Delay Lines

In this subsection we give two examples of recently fabricated S-band dispersive delay lines using the single film approach. Both were designed to give a linear differential delay of 200 nS over a 500 MHz bandwidth. These parameters are more applicable to the time dispersive delay elements in a microscan receiver than to variable delay lines for phased array antennas. The first used BVWs in a 20 μm YIG film spaced 127 μm from a ground plane. Figure 22a shows the calculated delay versus frequency expected for this device with arrows defining the region of linear delay. Figure 22b shows the corresponding phase error expected over a 1 cm pathlength for the bandwidth defined by the arrows in Figure 22a. A commercial 5 mil thick alumina substrate provided the dielectric spacer upon which were fabricated the transducers and microstrip feedlines. The transducers were 50 μm wide lines 5 mm long which then were continued as 50 ohm microstrip lines on the 5 mil alumina and left open-circuited at their ends. With a 5 mm wide YIG sample the transducer electrical length was one quarter wavelength at midband from

37
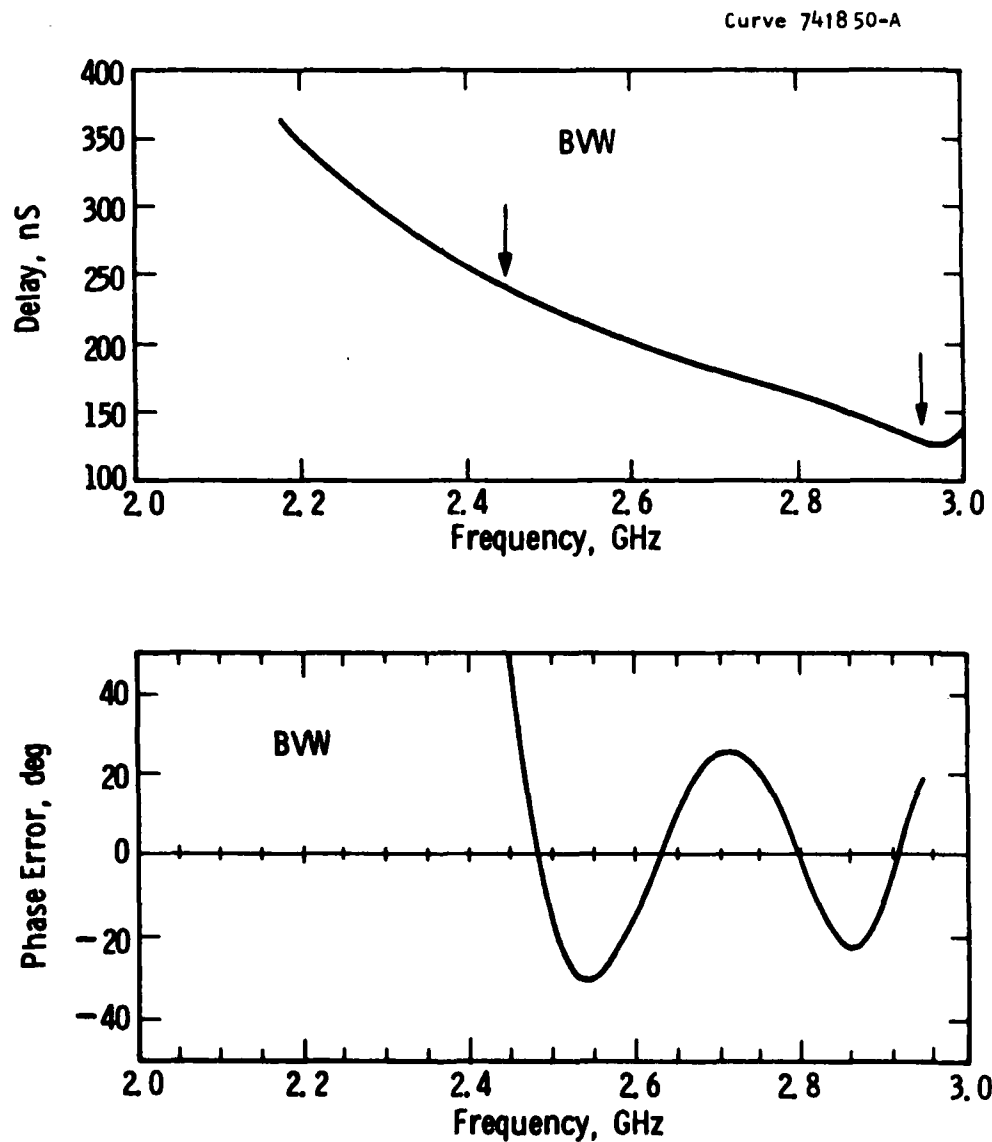
Figure 22.   (a) Calculated delay versus frequency for BVWs in a 20 μm
             thick YIG film spaced 127 μm from a ground plane. Arrows
             define a 500 MHz band of linear delay; H = 505G, transducer
             path separation 1 cm. (b) Phase error or phase deviation
             from a least-squares-fitted quadratic variation versus
             frequency corresponding to the linear delay region defined
             in Figure 22a.

38

the open-circuited ends to the midpoint of the YIG width. A 2 cm path-
length was required to achieve the 200 nS of differential delay. This
pathlength further dictated Sm-Co magnets measuring 1.5 inch x 1 inch to
achieve a field uniformity of ± 1% over the device active region.

Figure 23 shows the transmission loss and delay versus frequency
responses. The 200 nS linear differential delay was achieved although
it was upon a pedestal of 220 nS. At the low-k end of the band
significant ripple is evident, at least in part attributed to the
asymmetric walk-off angles which will be discussed later. Figure 24 is
a photograph of the device showing one of the Sm-Co magnets lying on the
lid. Calculations have predicted a maximum phase error of ± 45° over
the 500 MHz bandwidth for this delay line with its 2 cm pathlength.
This figure awaits experimental verification and requires a software
modification to the network analyzer program for its measurement.

The second delay line employed SWs with a new approach to
obtaining the ground plane spacing (Figure 25). A 10 micron thick YIG
film was glued face down on an optically transparent sapphire substrate.
The substrate was a commercially available 25 mil thick variety upon
which the transducers and microstrip lines had been photolithograph-
ically defined in 5 micron gold. As with the BVW delay line, the 50 μm
wide transducers were 5 mm long under the 5 mm wide YIG sample. They
then continued as 50 ohm microstrip lines and were left open-circuited.
The electromagnetic length, as before, was one quarter wavelength at
midband from the open-circuited end to the midpoint of the YIG width.
Optical transparency was required to allow curing of the glue (Norland
#61 optical cement) by a UV light source. The GGG substrate on the YIG
was then ground down to 50 microns and the ground surface plated with Au
to 5 μm for the ground plane. A 200 nS differential delay required a
2.5 cm pathlength and hence magnets measuring 2.75 inch x 0.75 inch to
give a ± 1% field uniformity. Figure 26a shows the calculated delay
versus frequency for a 1 cm pathlength with arrows defining a 500 MHz
bandwidth of approximately linear delay. Figure 26b shows the
corresponding phase error over the linear delay region again for a 1 cm

39
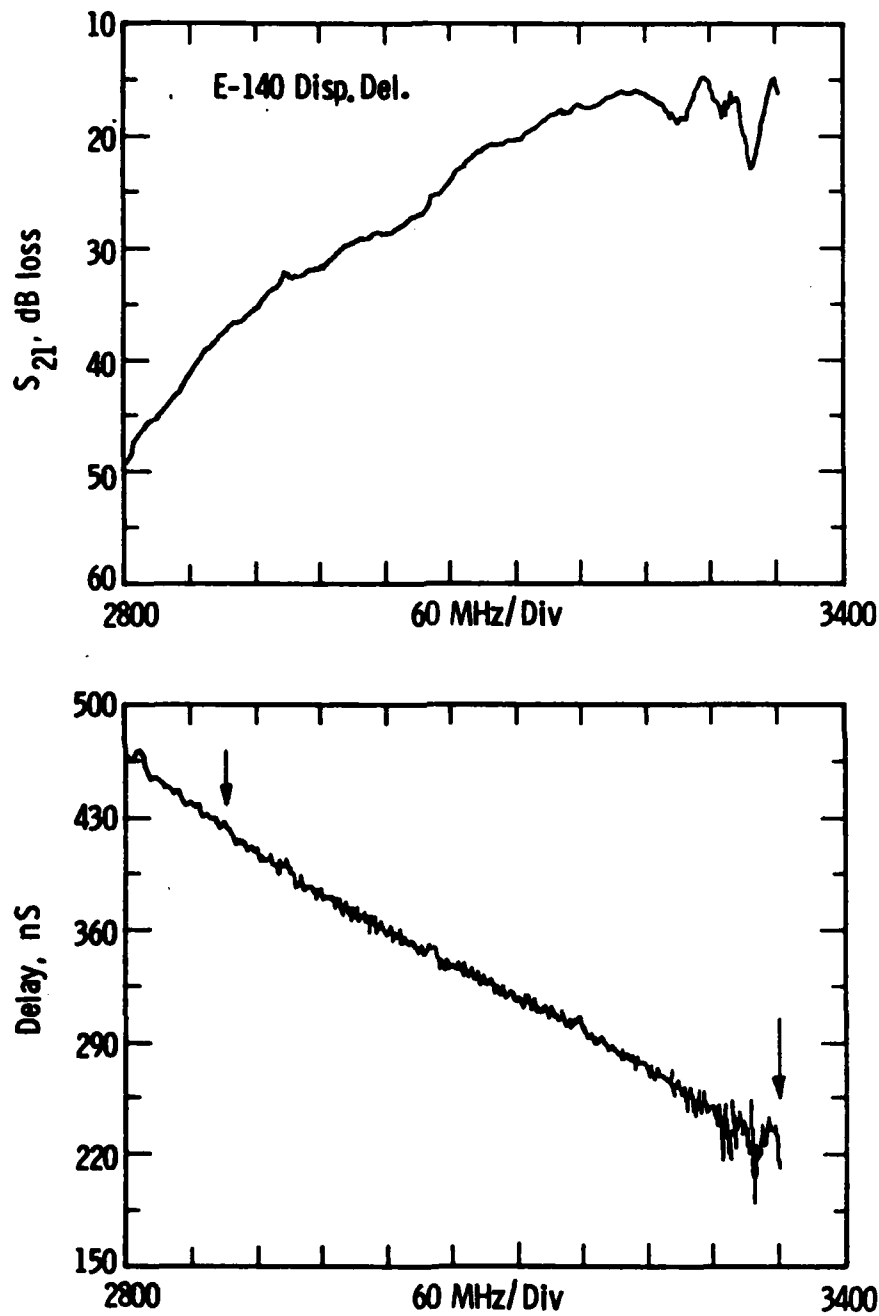
Figure 23. Upper curve: Transmission loss for the S-band BVW
dispersive delay line versus frequency.
Lower curve: Delay versus frequency with arrows defining a
band of linear delay variation.
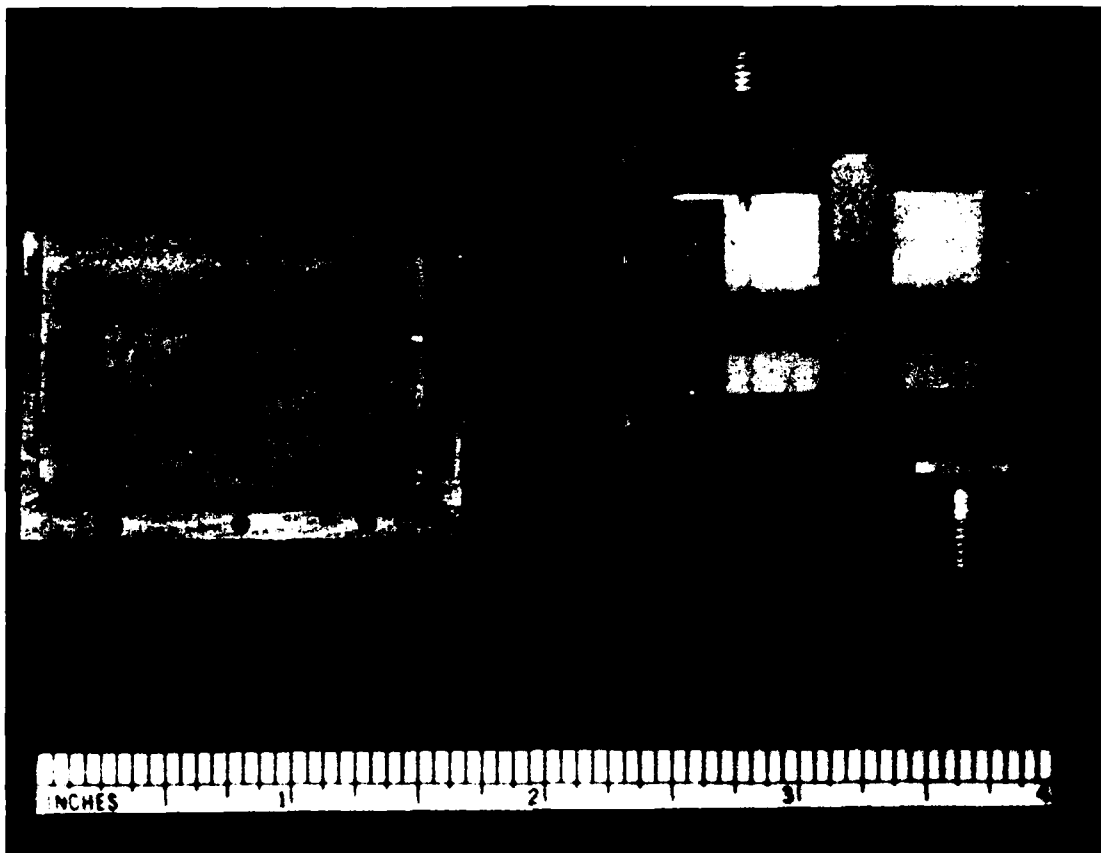
Figure 24. A photograph of the BVW delay line.

Dwg. 7775A52

5 μm Au Metalization

50 ohm Microstrip

50 μm wide transducer
under YIG

10 μm thick
YIG

25 mil thick
Sapphire substrate

50 μm thick GGG
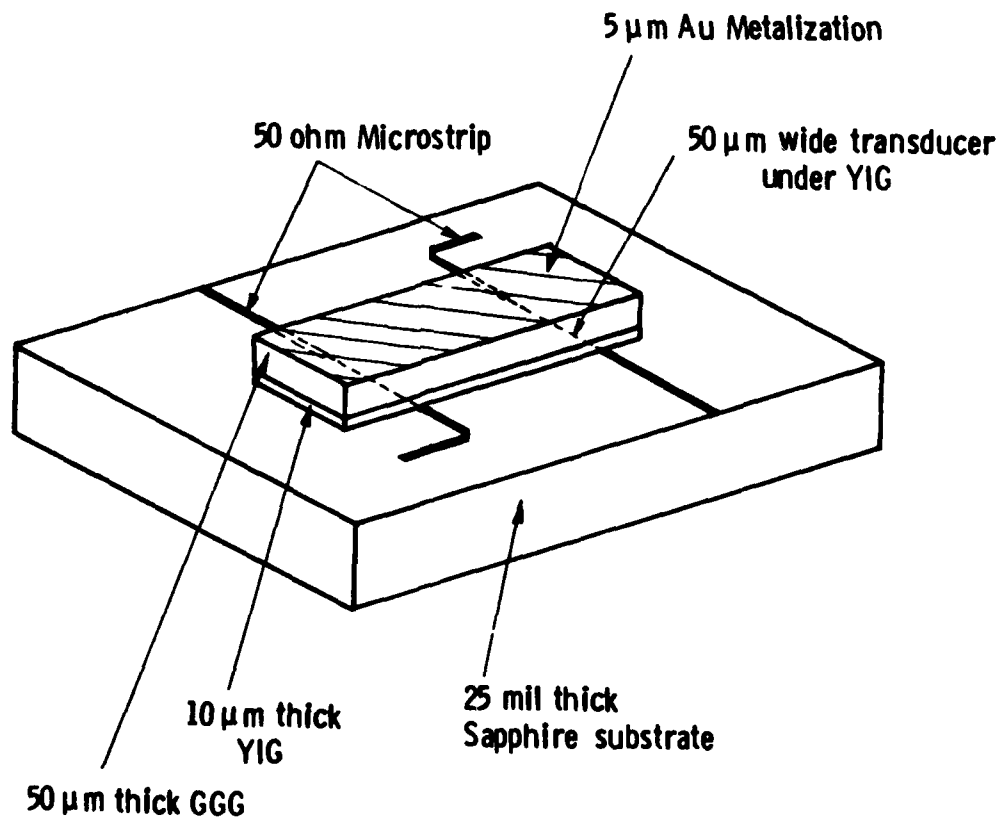
Figure 25. Perspective sketch of the SW dispersive delay line
construction. The SW propagates on the YIG film surface in
contact with the sapphire substrate.

42
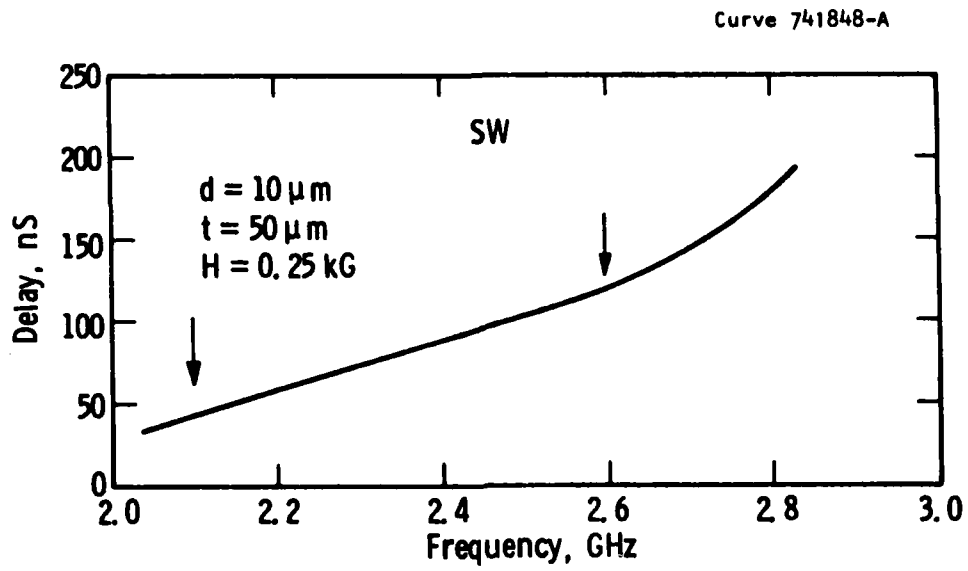
Figure 26a. Calculated delay versus frequency for SWs in a 10 μm YIG film spaced 50 μm from a ground plane. Arrows define a 500 MHz band of linear delay; H = 250G, transducer path separation 1 cm.
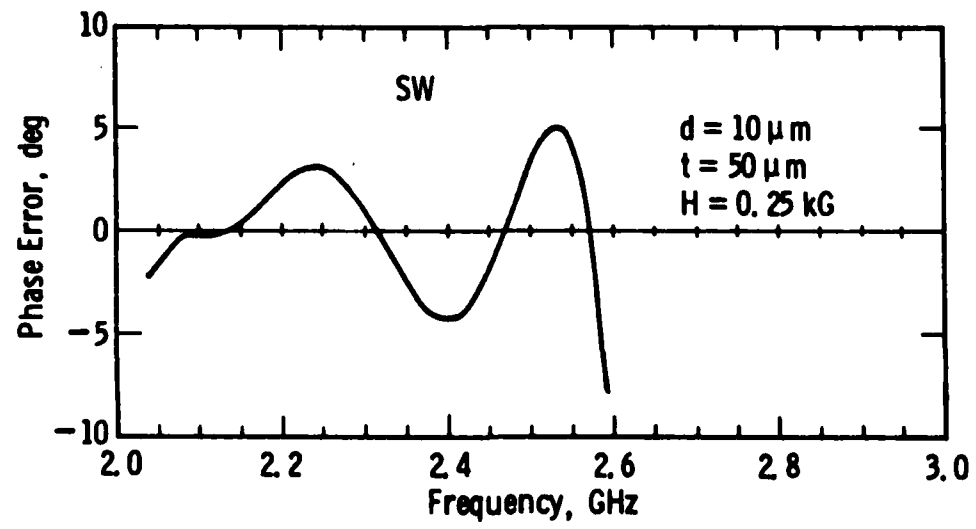
Figure 26b. Phase error or phase deviation from a least-squares-fitted quadratic variation versus frequency corresponding to the linear delay region in Figure 26a.

43

pathlength. Figure 27 shows the measured transmission loss and delay versus frequency. The 200 nS differential delay was met and, except again for amplitude ripple, the device performed as expected. Calculations had shown this delay line should have a maximum phase error of only ± 12° for the 2.4 cm pathlength of the device, but this remains to be measured. Figure 28 is a photograph of the device before deposition of the top metallization showing the one Sm-Co magnet required to generate approximately 350G of bias field.

2.6 Backward-Volume Wave Walk-Off

BVW beam walk-off is an interesting effect which results from a magnetostatic asymmetry caused by the presence of asymmetrically disposed ground planes on either side of the YIG; it can result in amplitude and delay ripple in BVW delay lines. In a wide enough sample, this walk-off of the beam could be compensated for by offsetting the receiver transducer with respect to the transmitter transducer to intercept the wavefront. However, in samples of practical widths ($\gtrsim$ 1 cm) this may not readily be achieved because the walk-off angles can be quite large — see Table 1 for some representative values. Additionally, the walk-off angle varies with frequency, particularly at the band edge.

Take the plane of the YIG film as the x-y plane with the static bias field (H) along x. For a sample of finite width (W), the magnetostatic boundary conditions are not satisfied by a standing transverse wave of the form $\sin k_y y$, where $k_y = n\pi/W$ for a single ground plane or two ground planes asymmetrically disposed about either face of the YIG. A present solution to the problem is to allow a travelling transverse wave of the form $e^{ik_y y}$ to exist when all boundary conditions are satisfied and a dispersion relation of the following form results:

$$\tan Md = \frac{\mu_1 MN(\tanh Ns + \tanh Nt)}{\mu_1^2 M^2 + (\mu_2 k_y + N \tanh Ns)(\mu_2 k_y - N \tanh Nt)}, \qquad [7]$$
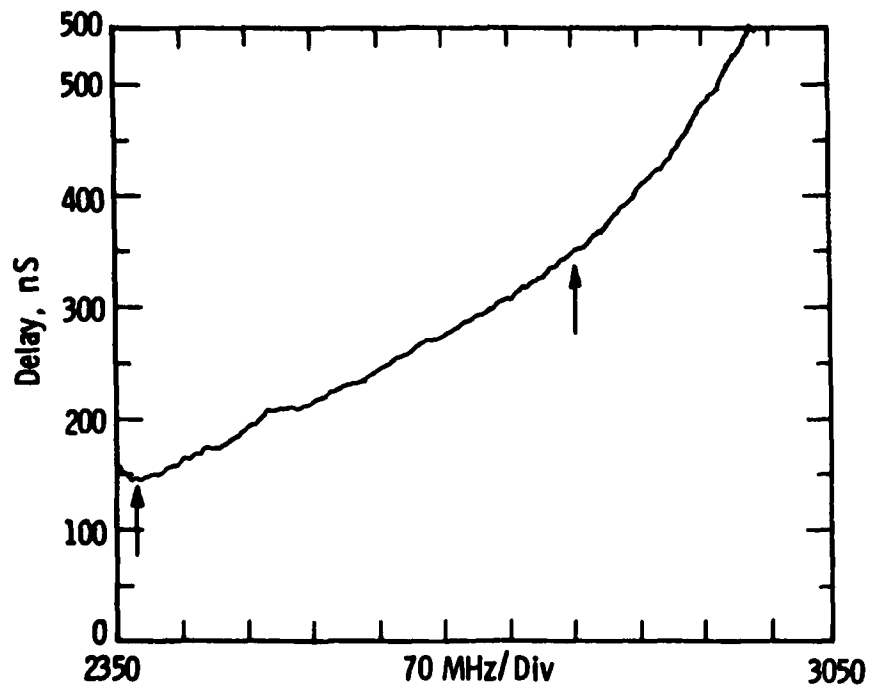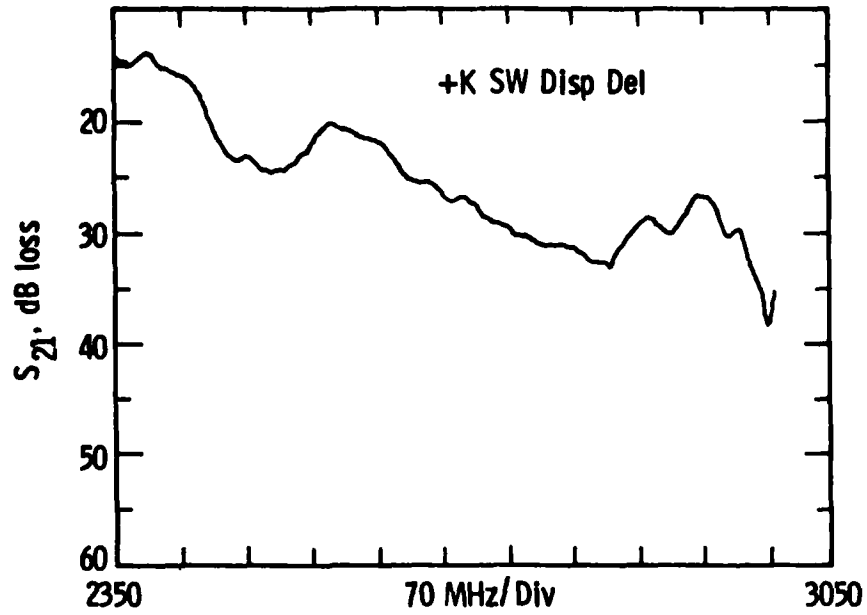
Figure 27. Upper curve: Transmission loss for the S-band SW dispersive delay line versus frequency.
            Lower curve: Delay versus frequency with arrows defining a band of linear delay variation.
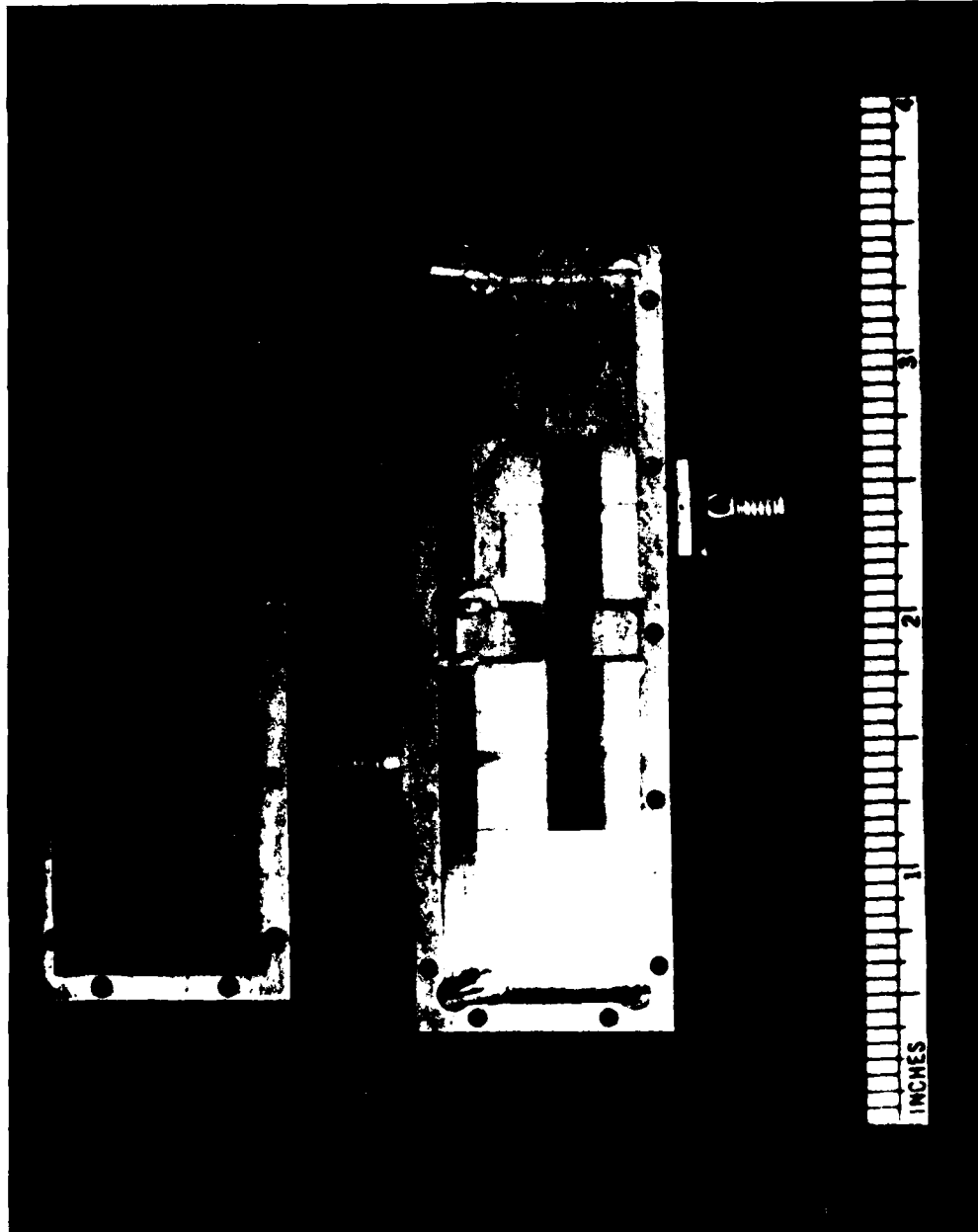
Figure 28. A photograph of the SW delay line before deposition of the top Au metallization.

46

d is the YIG film thickness and s and t are the respective ground plane spacings. The YIG permeability tensor components μ_1 and μ_2 are given in terms of the field H, magnetization $4\pi M$ and frequency f as:

$$\mu_1 = 1 - \frac{4\pi MH}{(\frac{f}{2.8})^2 - H^2} , \quad \mu_2 = \frac{4\pi M(\frac{f}{2.8})}{(\frac{f}{2.8})^2 - H^2} . \qquad [8]$$

The BVW has an x-component of wavevector k_x related by the equations:

$$M^2 = k_x^2/\mu_1 + k_y^2, \quad N^2 = k_x^2 + k_y^2 \qquad [9]$$

Figure 29 is a locus of k_x and k_y at a fixed frequency for two ground plane locations: 1) s = t = 400 μm; 2) s = 1 cm, t = 400 μm. In a sample of finite width W, Equation 7 is satisfied simultaneously for two values of k_y at a given value of f and k_x such that $k_y^+ + k_y^- = 2\pi/W$, as shown in Figure 29. If s = t, then symmetry has $k_y^+ = k_y^- = k_y$ and $k_y = \pi/W$ as for FVWs. Thus, in Figure 30 the BVW is characterized by two wavevectors, k_1 and k_2, inclined to x or the field direction at angles α_1 and α_2, respectively. The power flow angles ϕ_1 and ϕ_2 are the angles with respect to the wavevectors k_1 and k_2 and the power flow direction which is normal to the curve. k_1 and k_2 are each given by $k_1^2 = k_x^2 + k_y^{+2}$; $k_2^2 = k_x^2 + k_y^{-2}$. In general, if the ground plane spacings t and s are unequal, then $k_1 \neq k_2$, and $\alpha_1 \neq \alpha_2$, and $\phi_1 \neq \phi_2$. Thus, a transducer of BVWs would launch two waves k_1 and k_2 inclined at angles α_1 and α_2 to the x-axis and power flow would occur at angles ϕ_1 and ϕ_2 with respect to k_1 and k_2. At a receiving transducer the two waves would add to produce a varying amplitude with frequency because each would experience a different path between input and output transducers. If s and t are equal, then this asymmetry would disappear as shown in Figure 29 for s = t = 400 microns. Table 1 gives a list of representative values of the above parameters as a function of frequency for s = 1 cm, t = 400 microns, H = 0.7 kG, and W = 0.5 cm. Table 1 was obtained from a program which worked as follows. For a given frequency and α_1 value, it calculated k_1 using the standard BVW dispersion relation for an infinite width sample. It then evaluated α_2

47
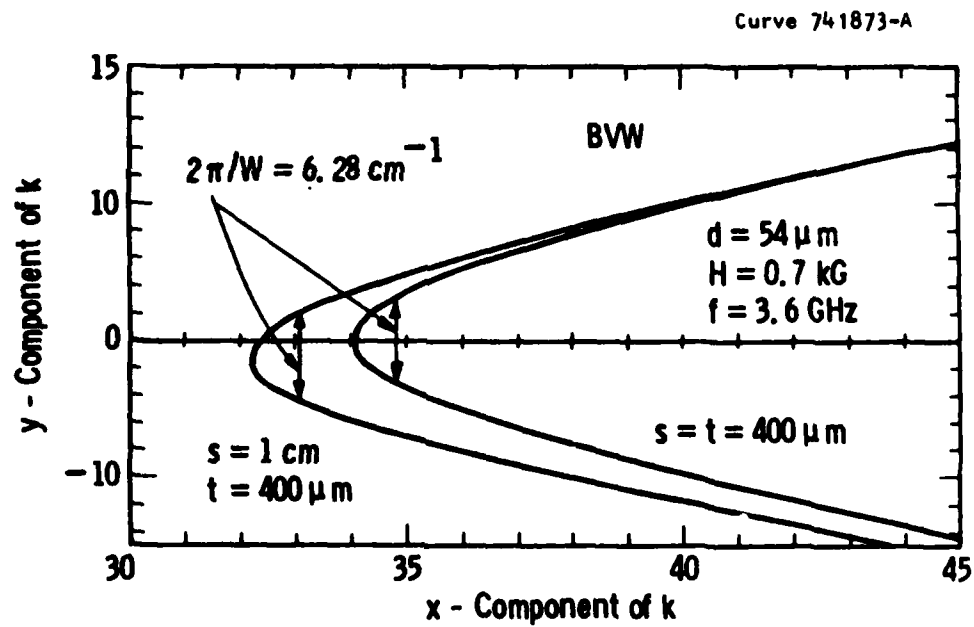
Figure 29. Two solutions to the BVW dispersion relation given by
Equation 7 at a fixed frequency of 3.6 GHz. Shown are two
locations for a transverse wavevector appropriate to a 1 cm
wide YIG sample.
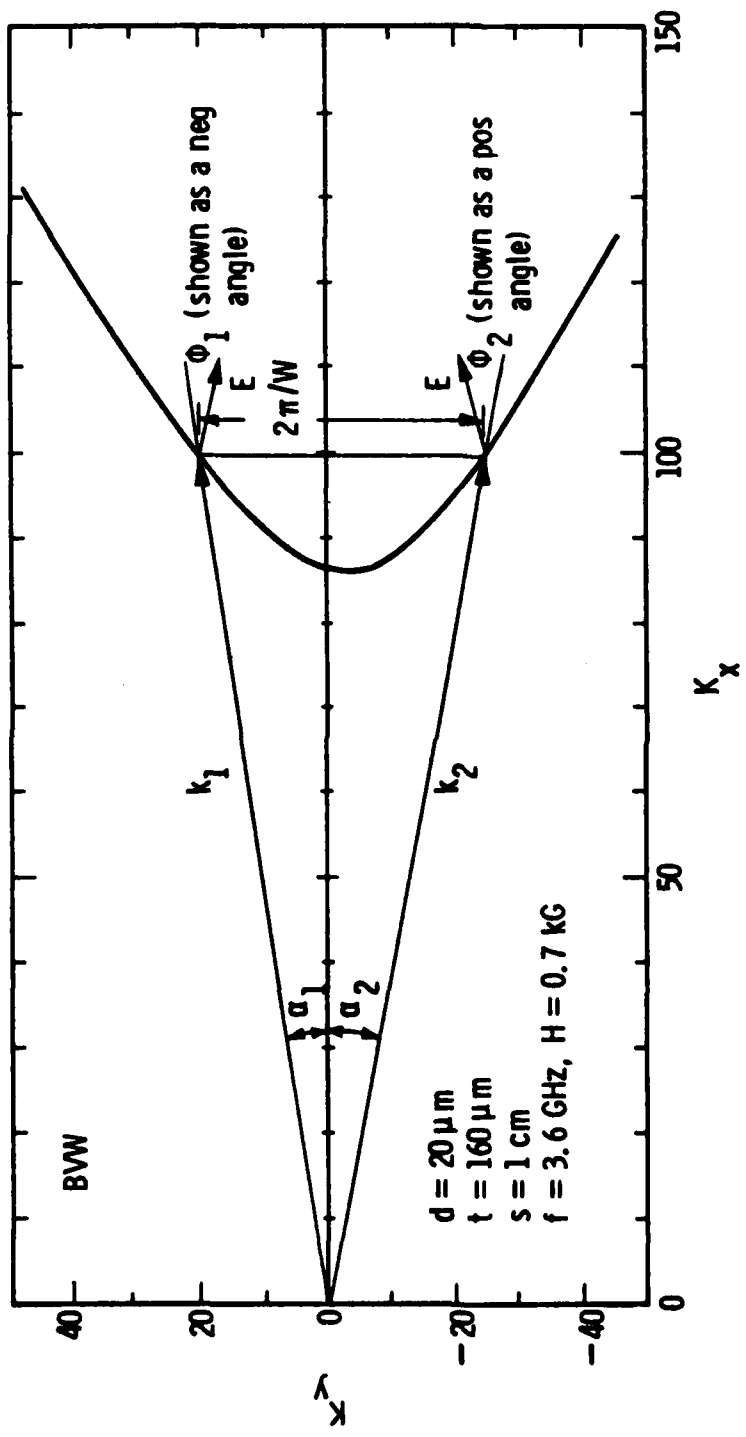
Figure 30. A solution to the BVW dispersion relation at a fixed frequency showing the wavevectors and energy flow angles appropriate to a sample of width W.

49

and hence k_2 such that $k_1 \cos \alpha_1 = k_2 \cos \alpha_2$. Finally, it compared $(k_1 \sin \alpha_1 + k_2 \sin \alpha_2)$ with $2\pi/W$ and repeated the whole calculation with a reset value of α_1 until an equality was obtained. The walk-off angles were calculated from a derived relation:

$$\tan \phi = - \frac{1}{k} \left. \frac{\partial F}{\partial \alpha} \right|_{k,\omega} \left(\left. \frac{\partial F}{\partial k} \right|_{\alpha,\omega} \right)^{-1} \qquad [10]$$

where F = dispersion relation for propagation at angle α to the field H. Thus, in Table 1, $k_1 \sin \alpha_1 + k_2 \sin/\alpha_2| = 2\pi|0.5$ to an accuracy of 0.001. Table 1 shows, as might be expected, that where k_1 or k_2 are comparable to $2\pi/W$, then k_1 and k_2 are most unequal in value as are the numerical value of α_1 and α_2. Hence, any amplitude ripple resulting from unequal pathlengths is going to be most manifest at the high-frequency (i.e., low k) end of the BVW band. Qualitatively, this is what is found experimentally, although a quantitative estimate of the ripple amplitude using the above analysis has not yet been made.

2.7 Coplanar Excitation of Magnetostatic Surface Waves

2.7.1 Coupling Constants

We here treat the theory of the generation of magnetostatic waves by currents flowing in a metallic plane adjacent to the magnetic medium. Such systems are slot lines and coplanar waveguides, which are sketched in Figure 31.

We state and comment on the results, derivations being relegated to Appendix I.

For surface waves, the forward and backward ranges of waves on a ferrite film adjacent to a metal are very different, as drawn in Figure 32. When k is positive, solutions exist between Ω_{min} and Ω_{max},

$$\Omega_{min} = (\Omega_H^2 + \Omega_H)^{1/2}, \quad \Omega_{max} = \Omega_H + 1 . \qquad [11]$$

50

Table 1

THE PARAMETERS SHOWN IN FIGURE 30 FOR A RANGE OF FREQUENCIES

f (GHz)	k_1 (cm^{-1})	k_2 (cm^{-1})	g_1 (nS)	g_2 (nS)	α_1 (deg)	α_2 (deg)	ϕ_1 (deg)	ϕ_2 (deg)
3.650	51.90	53.07	109.14	111.23	1.51	-12.18	-38.05	-43.46
3.600	87.34	87.76	115.51	116.01	2.19	-6.04	-23.68	-26.69
3.550	125.59	125.72	127.46	127.58	2.29	3.44	-17.85	18.87
3.500	167.09	167.13	137.54	137.57	2.01	-2.30	-14.09	14.37
3.450	211.35	211.35	145.48	145.48	1.67	-1.74	11.33	11.40
3.400	257.98	257.98	152.64	152.64	1.39	-1.40	-9.30	9.32
3.350	306.91	306.91	159.92	159.92	1.17	-1.17	-7.79	7.79
3.300	358.25	358.25	167.73	167.73	1.00	-1.00	-6.64	6.64
3.250	412.17	412.17	176.23	176.23	.87	-.87	-5.75	5.75
3.200	468.91	468.91	185.56	185.56	.77	-.77	-5.03	5.03
3.150	528.74	528.74	195.85	195.85	.68	-.68	-4.45	4.45
3.100	591.98	591.98	207.23	207.23	.61	-.61	-3.97	3.97
3.050	659.00	659.00	219.88	219.88	.55	-.55	-3.56	3.56
3.000	730.23	730.23	234.01	234.01	.49	-.49	-3.22	3.22

Dwg. 7775A53
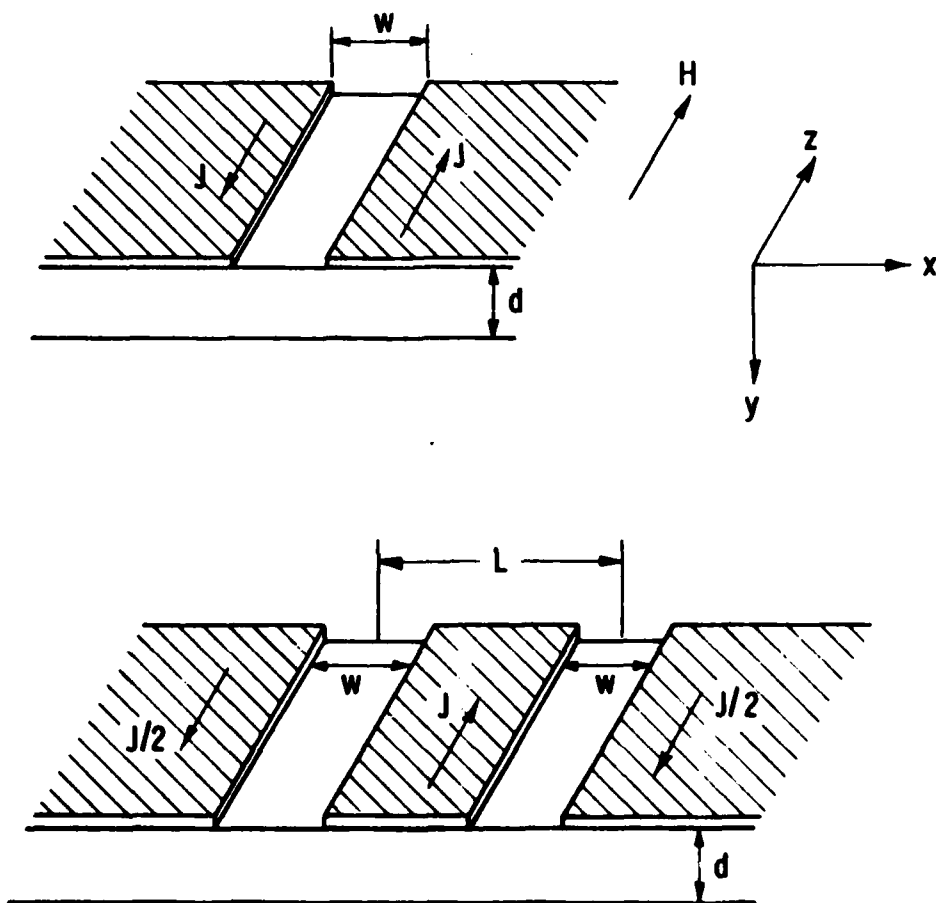
Figure 31. Slot line and coplanar waveguide.
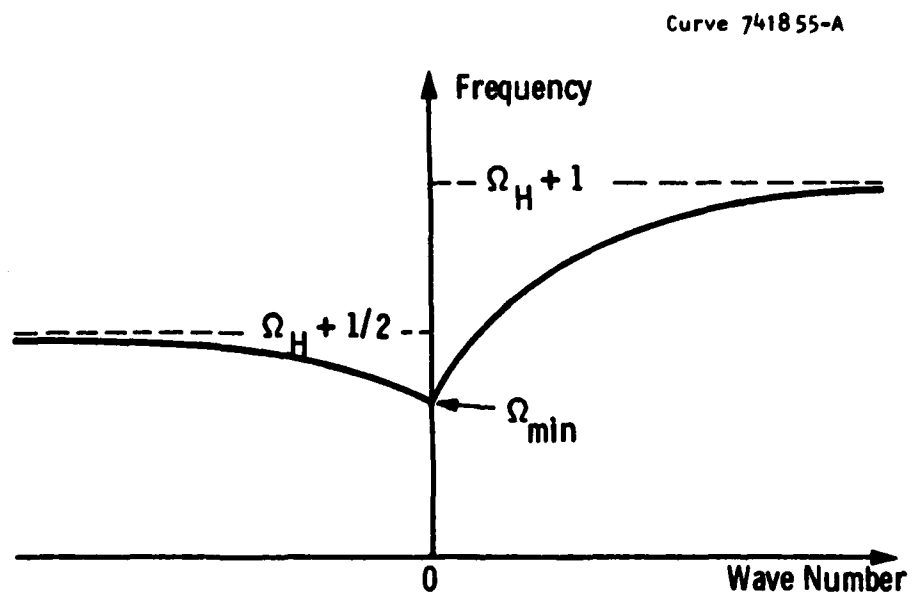
Figure 32.   Schematic dispersion relation for surface waves on metallized YIG.

When k is negative, the solutions occupy the narrower range between Ω_{min} and $\Omega_H + 1/2$, as shown.

The powers $P^{\pm}$ dissipated in the forward and backward directions have the form, for unit length of transducer,

$$P^{\pm} = R^{\pm} J^2, \qquad [12]$$

where J is the current (in the case of a slot line, J is the current on one side of the line), and the resistances per unit length are

$$R^{\pm} = \mu_o \omega K^{\pm} |s(k_{\pm})|^2 \qquad [13]$$

Here, μ_o is the vacuum permeability, ω is the frequency, $s(k_{\pm})$ is a shape function that is generally (but not always) less than unity, and the terms $K^{\pm}$ are coupling constants to forward and backward waves.

The coupling constants are

$$K^{\pm} = \frac{1}{8k_{\pm}d} \frac{\Omega^2 - \Omega^2_{min}}{\Omega^2_{max} - \Omega^2} \qquad [14]$$

where d is the thickness of the ferrite film. In the upper frequency range, above $\Omega_H + 1/2$, only k_+ exists, and only forward waves are emitted (see Figure 32). In the lower range of frequencies, $k_+ \ll k_-$ for a given frequency and, therefore, from Equation 14, $K^+ \gg K^-$.

It is therefore expected that coupling to the forward waves will be dominant at all frequencies. An exception to this usual rule can arise through the dependence of the shape factor s(k) on wavenumber, particularly in the slot line.

54

2.7.2 The Shape Function

The theory of the generation of magnetostatic waves usually involves Fourier transforms of the stimulating current. When the surface is metallized apart from some narrow gaps, as in Figure 31, the generating agent is the magnetic field in the gaps, which is proportional to the current, and the shape function is the Fourier transform of this field.

For a slot line of width w on a material of dielectric constant ε we have, approximately

$$s(k) \simeq \frac{\pi}{2} J_0(kw/2)/\cosh^{-1}(1/2k_{em}w) \qquad [15]$$

where k_{em} is the electromagnetic wavenumber at frequency ω, and $J_0(x)$ is the zero order Bessel function of argument x.

Coupling at a slot line is substantially reduced by the inverse cosh in Equation 15. At 9 GHz, with $\varepsilon = 16$ and $w = 30$ μm, this factor is approximately four; the total coupling strength, proportional to $|s|^2$, is reduced by more than an order of magnitude.

This reduction occurs because the current falls slowly at large distances compared with the width of the line; at distance x from the center the current falls as

$$1/[x^2-(w/2)^2]^{1/2}$$

up to distances of order $\lambda_{em}/2\pi$. Most of the current is therefore distant from the slot line and takes no part in the excitation.

For a coplanar waveguide, with slots of width w the centers of which are separated by a distance L, the shape function is approximately

$$s(k) \simeq \frac{\pi}{2} J_0(kw/2) \sin(kL/2)/\cosh^{-1}(2L/w). \qquad [16]$$

55

This approximation is best when $L \gg w$; in fact, $L = 2w$ is the most likely case, and the inverse cosh reduces the total coupling strength by about a factor of four.

2.7.3 Comments

The coupling of surface magnetostatic waves to a current is substantially less, for in-plane excitation, than the coupling to a microstrip.

Two effects are present:

i. In the slot line much of the current is not local and therefore plays no part in excitation. In the coplanar wave guide the central current is localized, but excitation on the two sides of the central strip is opposite in sense, giving rise, through the trigonometric term in Equation 16, to weak coupling at low magnetostatic wave numbers.

ii. The coupling constants K are somewhat less than in the case of a microstrip at low frequencies, though not at high. From the dispersion relations, together with Equation 14, one finds at small wavenumbers,

$$K^{\pm} = \frac{1}{4} \frac{\Omega_{min}}{\Omega_{max} \pm \Omega_{min}} \qquad [17]$$

This is a factor Ω_{min} times the coupling constants of a microstrip, so at S-band we expect weaker coupling, while at X-band we expect stronger coupling.

Against these we must set:

iii. The total coupling strength is certainly not weak; i.e., it is of order unity. At high frequencies in particular, the use of coplanar excitation offers relatively strong coupling over a much wider range of frequencies than can be achieved by an isolated microstrip.

Finally, we note an unusual effect in the characteristics of the coplanar waveguide; at small wavenumbers, radiation is stronger in the weak-coupling direction than in the opposite direction. This occurs because the coupling is inversely proportional to k, while the shape

56

factor is proportional to k when k is small. The power, $P \sim Ks^2$, therefore gives $P^-/P^+ = k_-/k_+$, which is a large ratio. This reversal of weak and strong directions can occur only at long wavelengths, and only when the excitation is asymmetric.

3. VARIABLE GROUND PLANE SPACING

3.1 Introduction

The delay versus frequency characteristics of simple delay lines comprising a YIG film spaced from a ground plane are dependent upon the saturation magnetization, bias field, YIG film thickness, and ground plane spacing. Improvements in the degree of delay linearity have been demonstrated by application of a linear variation in bias field along the length of a forward-volume wave delay line. However, this approach resulted in a reduction in bandwidth.[10] Earlier work on surface waves[11] had shown that a linear variation in delay with frequency could be obtained by adjusting the variation in the magnetic bias field along the length of the YIG film by a series of iron screws.

A study of how the different parameters affect the delay characteristics of forward-volume waves indicated, however, that a controlled variation of the ground plane spacing would be most effective in synthesizing linearly dispersive delay lines.

3.2 Stepped Ground Plane

The variation in group delay with frequency for different ground plane spacings away from a 20 μm thick YIG film is shown in Figure 33. Examination of this figure shows that it may be possible to achieve a linear variation of delay with frequency if the delay line is composed of several short sections, each with a different ground plane spacing, as shown in Figure 34a.

Fixing the number of sections and their ground plane spacing, the group delay was then calculated for each section and their length optimized so as to obtain a minimum phase error from a quadratic phase versus frequency variation. (Phase deviation from an ideal quadratic

58
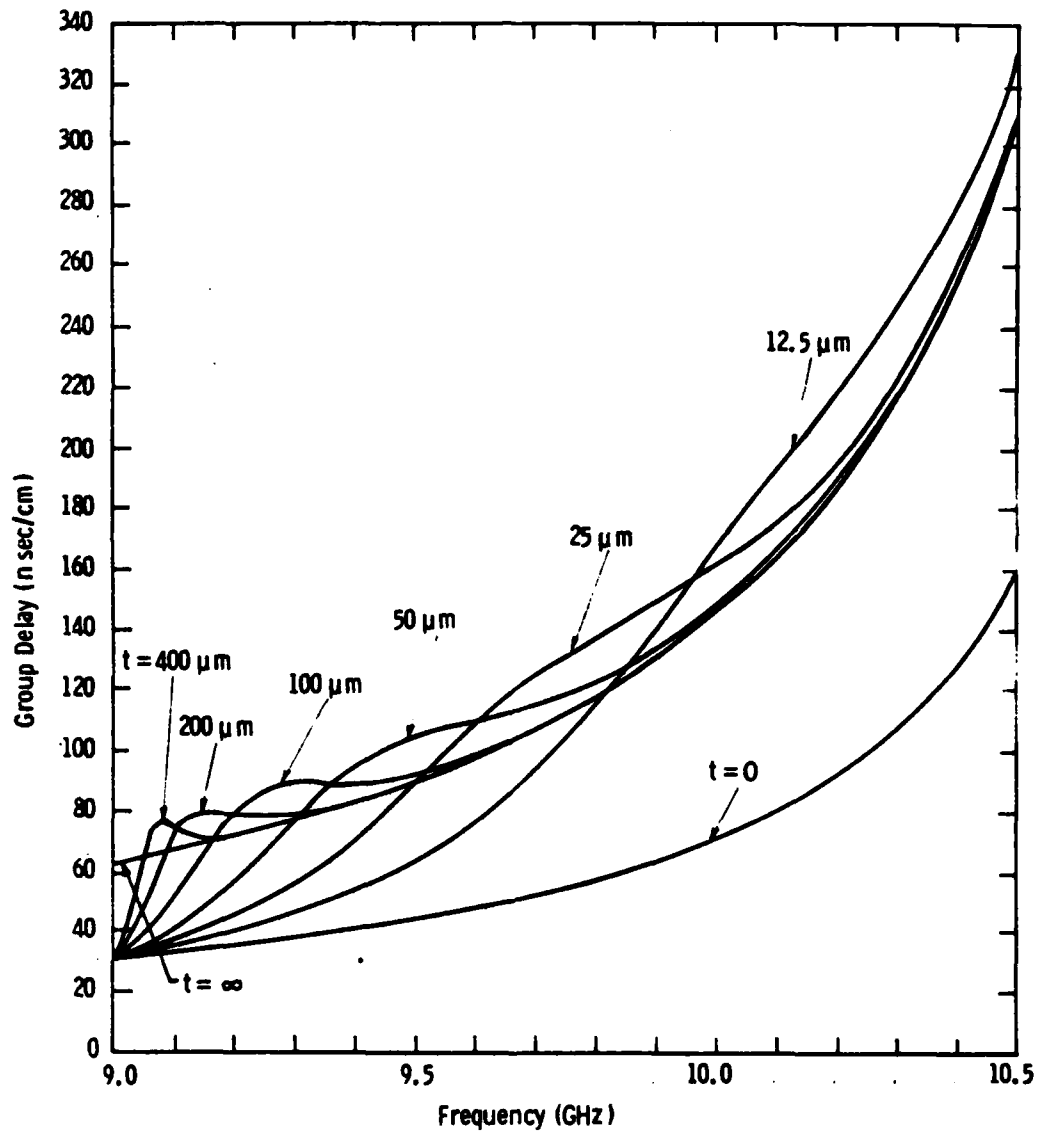
Figure 33. Variation of group delay with frequency for FVWs with the spacing, t, of the YIG from one ground plane as a parameter. The YIG film thickness is 20 μm.

Dwg.7758A14
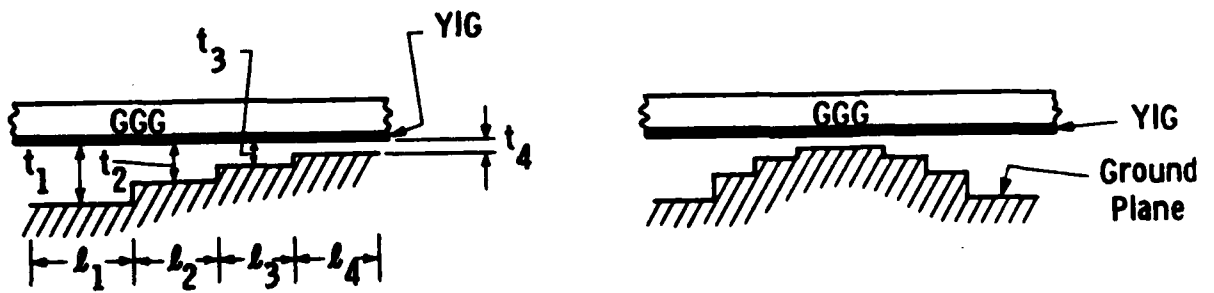
Figure 34. (a) Stepped ground plane with single YIG film; (b) Stepped spacing between two YIG films.

60

phase versus frequency variation is a more sensitive measure of the delay linearity.) The minimum phase error obtained is dependent to some extent upon the choice of ground plane spacing for each section, the number of sections, and the bandwidth over which the optimization is performed.

3.2.1 Calculated Results

Calculated results with a YIG film 32 μm thick and 0.5 cm wide are shown in Figure 35 for a delay line with four sections and the dimensions shown in Table 2.

Table 2

GROUND PLANE SPACINGS AND LENGTHS FOR A FOUR-SECTION DELAY LINE

Section Number, n	Ground Plane Spacing, t_n (cm)	Section Length, ℓ_n (cm)
1	0.0032	0.180
2	0.0045	0.369
3	0.0075	0.155
4	0.0136	0.296

The deviation from a linear variation of delay with frequency in Figure 35 is less than 0.5 nS. The calculated phase error over the same bandwidth is shown in Figure 36 and is less than $\pm 7^{\circ}$. This result could be improved even further by increasing the number of sections or by optimizing the ground plane spacings as well as the length.

In principle, zero phase error could be obtained over some bandwidth with an infinite number of steps, i.e., a continuous variation in ground plane spacing. This approach is treated in the next section. One potential problem with the stepped structure is that each change in ground plane spacing causes a change in the wave number over a limited frequency range. The resulting wave impedance mismatch and

61
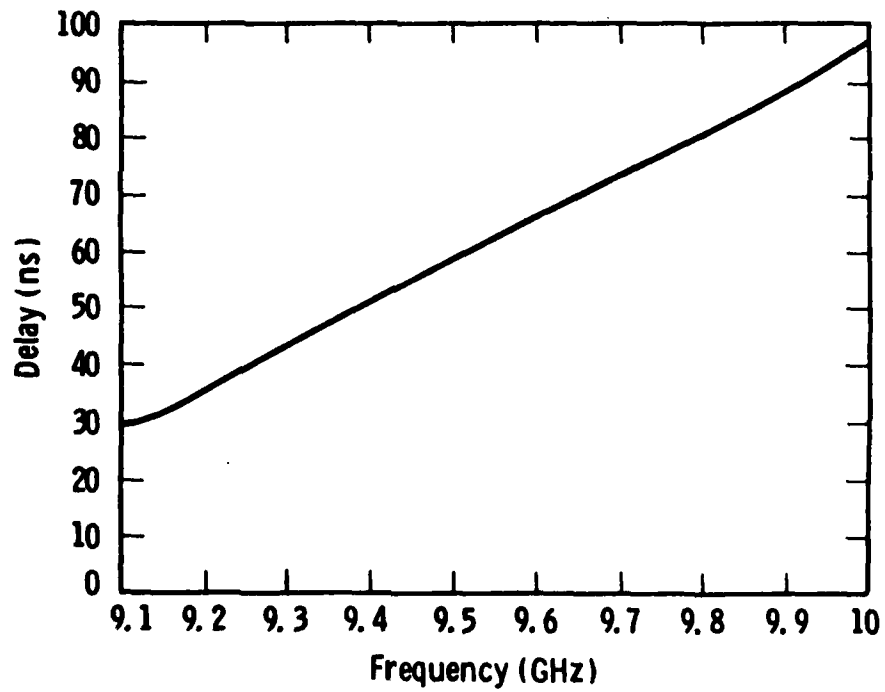
Figure 35. Calculated variation of group delay with frequency for a YIG
film 32 μm thick, and a stepped ground plane of dimensions
given in Table 2.

Curve 739186-A
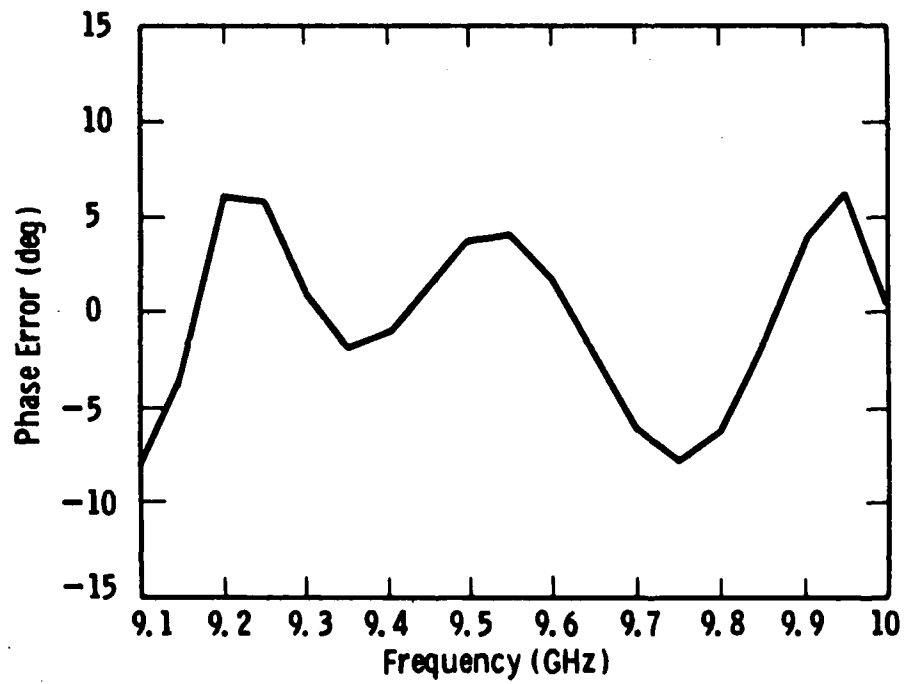
Figure 36. Calculated phase error from a quadratic phase with frequency variation as a function of frequency for the same conditions as in Figure 35.

63

hence MSW reflection coefficient can be minimized to acceptable levels
by using small enough steps. Steps greater than approximately 0.0005
inch may be produced by machining. Smaller steps may be produced by
photolithography and etching of a suitable metal, or a semiconductor or
insulator which may then be metal coated.

3.2.2 Experimental Results

Initial experiments have been performed with a ground plane
machined to give the dimensions shown in Table 2, which established the
feasibility of this technique. Measured results of delay as a function
of frequency are shown in Figure 37. The principal source of delay
ripple, occuring near 9.4 GHz, was identified as the step between
sections 3 and 4. However, provided small step sizes are used, the
ripple and spurious signals could be kept within acceptable limits.
Reflections due to the finite step size may also be reduced by making
the transitions between sections occur gradually over a distance long
compared to the MSW wavelength affected most by the step.

These techniques are also applicable to surface wave devices.
Furthermore, a modification could be used in double film structures, as
shown in Figure 34b, where the spacing between two YIG films is made
variable in steps of finite length. Again, the length of each section
and/or film spacing could be optimized to yield the desired delay
characteristic. In practice, the GGG layer separating the two YIG films
could be masked and etched to produce the desired step size and then the
second YIG film grown. In this case it may be possible to obtain a
continuous variation in GGG thickness by withdrawing a GGG-coated YIG
film at a controlled rate from a hot HPO_3 etch, before growth of the
second YIG film. This double YIG film technique is applicable to FVW
and BVW propagation in double film structures.

64

Curve 739185-A

MSVW Stepped Ground Plane
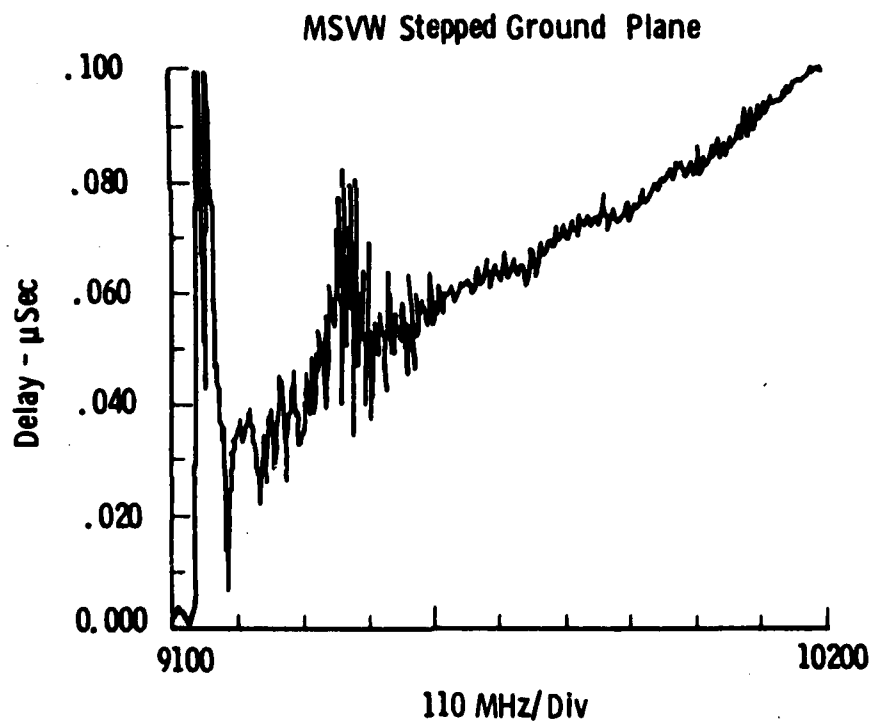
Figure 37. Measured variation of group delay with frequency for a delay line with dimensions given in Table 2.

65

3.3 Continuous Variation

The basic idea behind designing delay lines composed of sections of finite length and different ground plane spacing has a natural extension in the problem of a continuous variation of the ground plane spacing. That is, the resulting dispersive delay line can now be thought of as composed of sections of infinitesimal length with different distance from the YIG film to a conducting surface.

Such an approach would be expected to eliminate much of the delay ripple due to mismatch between sections of finite length since it presents, instead, a smooth transition between infinitesimally short sections.

At first, for simplicity, take the distance to the ground conducting surface to be a quadratic function t of the propagation direction y, i.e.,

$$t(y) = ay(y-L) + t_o \qquad [18]$$

where L is the length of the delay line, t_o is the ground surface spacing at both ends of the delay line, and a defines the curvature. This is the equation of a parabola symmetric about the point y = L/2. We can assume a symmetric ground surface without loss of generality since the total delay is the summation of the delay in each infinitesimal section. Thus, the delay variation with frequency will be defined only by the first half of the delay line, whereas the second half multiplies this delay by a factor of two.

The assumption was made that the ground surface curvature is small enough for the magnetostatic field distribution to change slowly as fields propagate down the delay line.

Figures 38a and b show the geometry to be studied. In the YIG film the magnetostatic potential ψ satisfies the equation

$$\mu_1 \left(\frac{\partial^2 \psi}{\partial x^2} + \frac{\partial^2 \psi}{\partial y^2}\right) + \frac{\partial^2 \psi}{\partial z^2} = 0 \qquad [19]$$

66
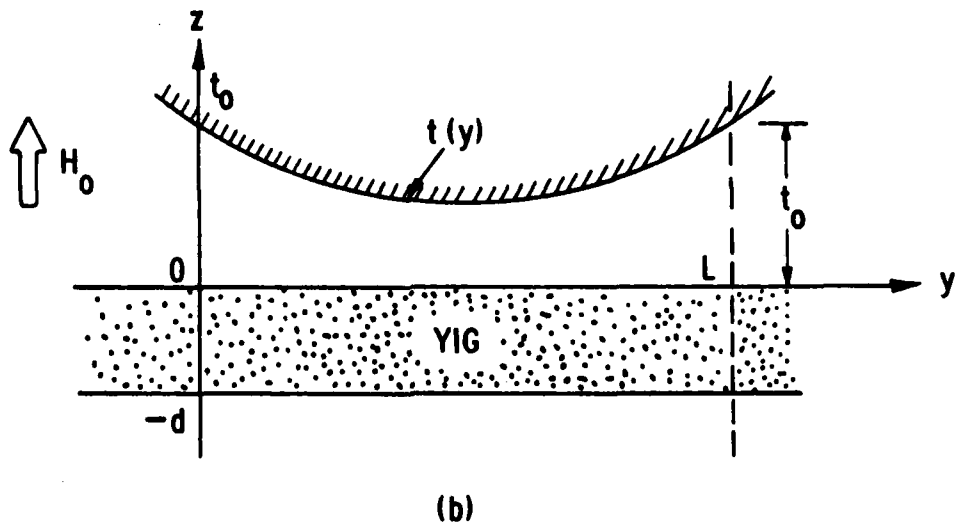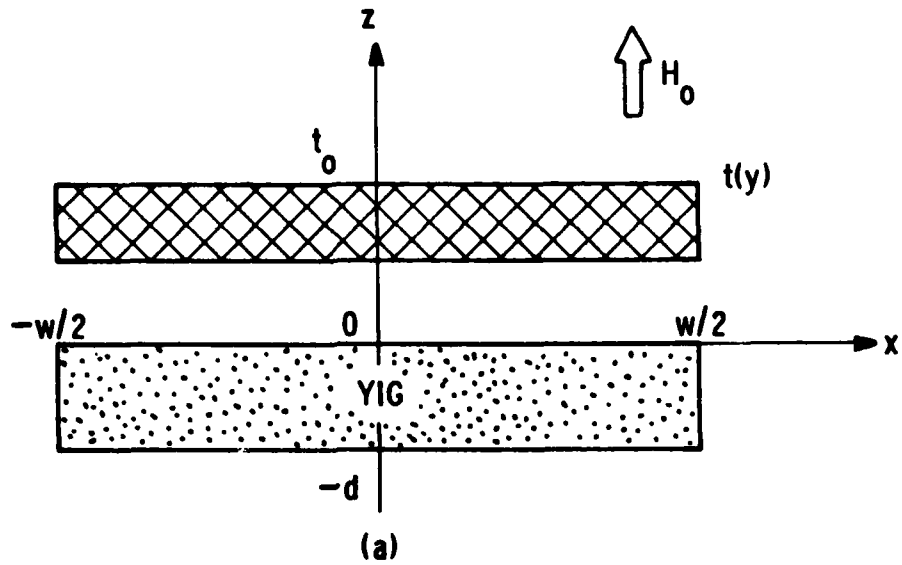
Figure 38. The continuously variable ground plane spacing structure. The conducting surface is a parabola in the direction of propagation (y) but constant in the transverse direction (x). (a) and (b) show cross sections of the structure corresponding to the planes $y = 0$ and $x = 0$, respectively.

with
$$\mu_1 = 1 - \frac{\Omega_H}{\Omega^2 - \Omega_H^2}$$

and
$$\Omega_H = H/4\pi M \; ; \; \Omega = \omega/(\gamma 4\pi M) \; .$$

FVWs have a sinusoidal distribution of the magnetostatic fields across a YIG film with two parallel ground planes uniformly spaced from the YIG surfaces. Now, however, the distance to one of the conducting planes varies along the propagation direction y. Therefore, both the transverse distribution of the potential ψ and the phase along y will now be functions of y. The magnetostatic potential can then be written as

$$\psi = [Ae^{j\kappa(y)z} + Be^{-j\kappa(y)z}] \, e^{-j\phi(y)} \qquad [20]$$

where $\kappa(y)$ is the transverse wavenumber and $\phi(y)$ is the phase along the propagation direction. In the particular case of $t(y)$ = constant, $\phi(y)$ = βy, where β is the propagation constant.

Substituting Equation 20 into Equation 19 and rearranging terms we obtain

$$Ae^{j\kappa z}\left\{\mu_1[j\phi" - j\kappa"z + (\phi' - \kappa'z)^2)] + \kappa^2\right\} + \qquad [21]$$

$$Be^{-j\kappa z}\left\{\mu_1[j\phi" + j\kappa"z + (\phi' + \kappa'z)^2] + \kappa^2\right\} = 0$$

where prime and double-prime mean differentiation with respect to y. Notice that for $t(y)$ = constant $\kappa" = \kappa' = \phi" = 0$ and $\phi' = \beta$, giving the eigenvalue equation

$$\mu_1 \beta^2 + \kappa^2 = 0$$

If the assumption of a slow variation of the field distribution in the y-direction is to remain valid, the term $\kappa'z$ must be negligible with respect to ϕ', which is of the order of β. Also, the derivative of ϕ' is expected to be small so that

$$(\phi')^2 \gg j \, (\phi'' - \kappa''z).$$

These simplifications result, from Equation 21, in the equation

$$-\mu_1(\phi')^2 = \kappa^2(y) \qquad [22]$$

Since $\kappa^2(y)$ must be positive for a trigonometric distribution of potential, forward-volume waves exist in the range of frequencies where $\mu_1 < 0$.

In the regions adjacent to the YIG film, the field distribution is hyperbolic. Since the potential ψ satisfies Laplace's equation, a similar analysis as that performed above leads to the equation

$$(\phi')^2 = \kappa_o^2(y) > 0. \qquad [23]$$

From Equations 22 and 23, introducing the label $K(y)$,

$$\frac{\kappa^2(y)}{-\mu_1} = \kappa_o^2(y) \equiv K^2(y) > 0 \qquad [24]$$

so that $\varphi'(y) = K(y)$

or, integrating over the length L of the delay line,

$$\phi(L) = \int_o^L K(y)dy \qquad [25]$$

In other words, the delay line can be thought of as composed of infinitesimal sections of length dy. The propagation constant $K(y)$ of each section is found assuming each section to be formed by a YIG film sided by an infinite ground plane at $z = t(y)$ (see Figure 38). The phase change in each section is then $K(y)dy$, and so the total phase change for the delay line is given by Equation 25. Fixing the length L and the spacing t_o (Equation 18), the total phase change will be a function of the curvature a as well as the frequency. We then rewrite Equation 25 as

$$\phi(\omega,a) = \int_o^L K(\omega,a,y)dy.$$

For a linear variation of delay with frequency, the phase ϕ is required to approach a second order polynomial in ω in the sense of least squares over the band of interest. Namely, if

$$P_2(\omega) \equiv C_2\omega^2 + C_1\omega + C_o,$$

the coefficients C_i must be found, as well as the curvature a, which minimize the distance

$$D(C_0,C_1,C_2,a) = \int_{\omega_1}^{\omega_2} [P_2(\omega) - \phi(\omega,a)]^2 \, d\omega, \qquad [26]$$

where ω_1 and ω_2 define the band of interest. The following equation must then be satisfied:

$$\frac{\partial D}{\partial C_o} = \frac{\partial D}{\partial C_1} = \frac{\partial D}{\partial C_2} = \frac{\partial D}{\partial a} = 0.$$

From Equation 26, minimization with respect to C_0,C_1,C_2 leads to the linear system of equations

$$\begin{bmatrix} \Omega_0 & \Omega_1 & \Omega_2 \\ \Omega_1 & \Omega_2 & \Omega_3 \\ \Omega_2 & \Omega_3 & \Omega_4 \end{bmatrix} \begin{bmatrix} C_0 \\ C_1 \\ C_2 \end{bmatrix} = \begin{bmatrix} \int_{\omega_1}^{\omega_2} \phi(\omega,a)d\omega \\ \int_{\omega_1}^{\omega_2} \omega\phi(\omega,a)d\omega \\ \int_{\omega_1}^{\omega_2} \omega^2\phi(\omega,a)d\omega \end{bmatrix} \qquad [27]$$

where $\Omega_m \equiv \int_{\omega_1}^{\omega_2} \omega^m d\omega = \dfrac{\omega_2^{m+1} - \omega_1^{m+1}}{m + 1}$, $m = 0, \ldots, 4$

The solutions of Equation 27 are functions of a which can be substituted into the equation of minimization with respect to a, i.e.,

70

$$\frac{\partial D}{\partial a} = C_2(a) \int_{\omega_1}^{\omega_2} \omega^2 \frac{\partial \phi}{\partial a} \, d\omega + C_1(a) \int_{\omega_1}^{\omega_2} \omega \frac{\partial \phi}{\partial a} \, d\omega +$$

$$C_0(a) \int_{\omega_1}^{\omega_2} \frac{\partial \phi}{\partial a} \, d\omega - \int_{\omega_1}^{\omega_2} \phi \frac{\partial \phi}{\partial a} \, d\omega = 0 \qquad [28]$$

Equation 28 is nonlinear in the parameter a, the curvature sought, which minimizes the distance between the phase ϕ and the quadratic polynomial $P_2(\omega)$.

3.3.1 Numerical Results

A computer program has been written in Fortran language to perform these calculations. The integrals involved have been calculated using pertinent subroutines from the IMSL package.[12]

The potential advantages of this approach have been demonstrated by direct comparison of our calculations with those presented in the last section for the discrete case, i.e., the same parameters and frequency range have been used. Furthermore, it was observed that a parabola passes through the middle of three of the four steps, as shown in Figure 39. This parabola is defined by the parameters (see Equation 18; L = 1cm):

$$a = 0.04 \text{ cm}^{-1}$$

$$t_0 = 0.0132 \text{ cm}$$

Using these as starting values for a minimum quadratic error search, it was found that for

$$a = 0.0415 \text{ cm}^{-1}$$

$$t_0 = 0.0128 \text{ cm}$$

71
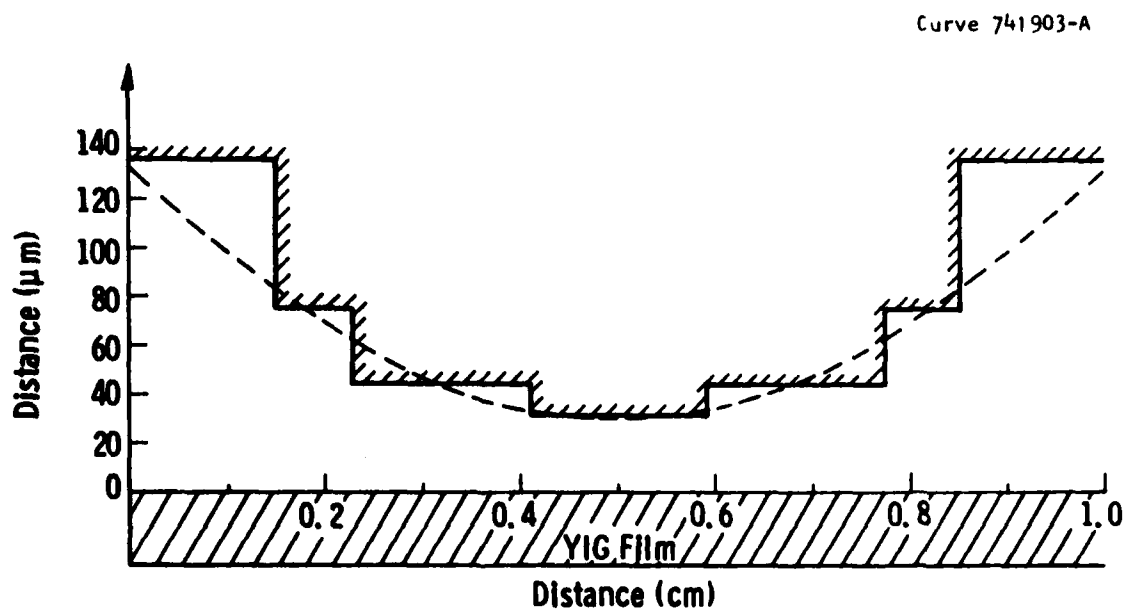
Figure 39. Direct comparison between the two approaches to the variable ground plane spacing technique. A parabola passes through the middle of three of the four steps of the discrete-step delay line.

a phase error of less than ± 15° and a delay deviation from linearity of less than 0.5 nS is obtained from 9.1 to 10 GHz. The delay ranges from 30 to 105 nS. Figures 40 and 41 show the delay and phase error, respectively.

The dashed curve in Figure 40 is the delay for the case of a ground plane (a = 0.0) at a distance equal to the YIG film thickness. It has been shown[2] that this design (ground plane spacing equal to YIG thickness) is optimum for FVW linearly dispersive delay lines composed of a YIG film at a constant distance from a conducting plane. Notice then the significant improvement in delay linearity achieved when the ground plane becomes a parabola with the proper curvature and spacing.
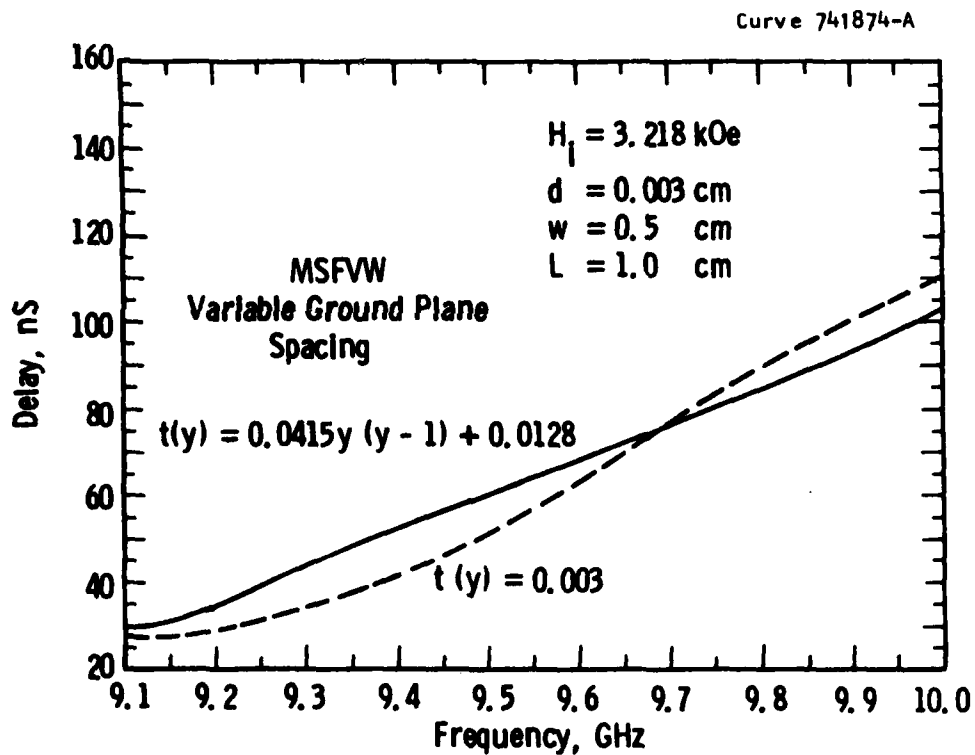
Figure 40. Delay versus frequency characteristic for a delay line with a parabolic ground surface of curvature $a = 0.0415 \text{ cm}^{-1}$ spaced at the ends by $t_o = 0.0128$ cm. The dashed curve corresponds to a ground plane at a distance from the YIG film equal to its thickness, i.e., $t(y) = d = 0.003$ cm (H_i = internal magnetic field, w = YIG width, d = YIG thickness, L = delay line length, $t(y)$ = ground surface).

74
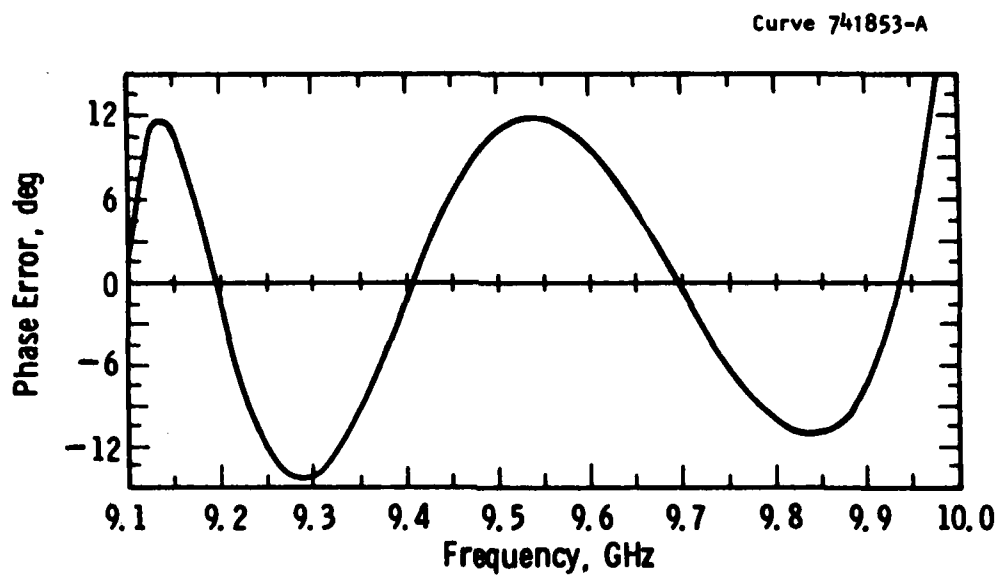
Figure 41. Phase error for the delay line with parabolic ground surface of Figure 40.

4. ARBITRARY MAGNETIZATION ANGLE

The propagation of magnetostatic waves in a variety of YIG-layered planar structures has been investigated in the past. With a few exceptions,[13-18] the theoretical and experimental investigations consider only specific configurations. This work presents a general theoretical and experimental investigation of magnetostatic volume wave propagation in an arbitrarily magnetized YIG film separated from a metal by a dielectric layer. The importance of this study is that dispersion and delay can be controlled to some extent by changing the magnetic-field angle.

4.1 Theory

4.1.1 Permeability Tensor

First, the general permeability tensor was derived using the coordinate transformation method (see Figure 42). The direction of the internal magnetic field was assumed to be arbitrary with respect to the coordinate axes. The unprimed coordinate system was subjected to successive rotations through the first two Eulerian angles[19] ϕ and θ, these angles were chosen so that the Z'-axis of the primed coordinate system was parallel to the internal field. Thus, in the primed coordinate system, the permeability tensor $\underline{\mu}'$ was given as

$$\underline{\mu}' = \begin{bmatrix} \mu & j\kappa & 0 \\ -j\kappa & \mu & 0 \\ 0 & 0 & 1 \end{bmatrix} \qquad [29]$$

where

$$\mu = \frac{\omega_o(\omega_o + \omega_m) - \omega^2}{\omega_o^2 - \omega^2}, \quad \kappa = \frac{\omega \omega_m}{\omega_o^2 - \omega^2}, \quad \omega_o = \gamma H, \quad \omega_m = \gamma 4\pi M_o \qquad [30]$$

76
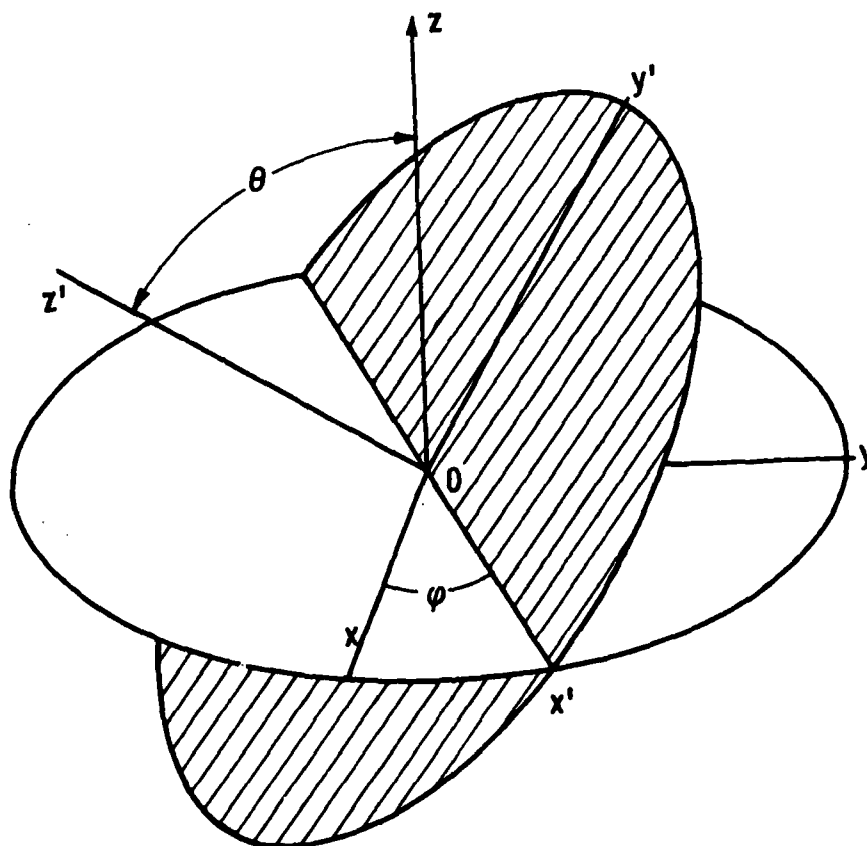
Figure 42. The primed and unprimed coordinate systems.

In Equation 30, H, ω, $4\pi M_o$, and γ are the internal dc magnetic field, wave frequency, saturation magnetization, and gyromagnetic ratio, respectively. The desired rotations were performed through the following orthogonal matrix A[19]

$$A = \begin{bmatrix} \cos\phi & \sin\phi & \phi \\ -\cos\theta\,\sin\phi & \cos\theta\,\cos\phi & \sin\theta \\ \sin\theta\,\sin\phi & -\sin\theta\,\cos\phi & \cos\theta \end{bmatrix}$$ [31]

The relation between the permeability tensor $\underset{=}{\mu}$ (unprimed coordinate system) and $\underset{=}{\mu}'$ (primed coordinate system) was expressed as[19]

$$\underset{=}{\mu}' = A\,\underset{=}{\mu}\,\widetilde{A} ,$$ [32]

where $\widetilde{A}$ is the transpose of A. Equivalently,

$$\underset{=}{\mu} = \widetilde{A}\,\underset{=}{\mu}'\,A = \begin{bmatrix} \mu_{11} & \mu_{12} & \mu_{13} \\ \mu_{21} & \mu_{22} & \mu_{23} \\ \mu_{31} & \mu_{32} & \mu_{33} \end{bmatrix}$$ [33]

where

$\mu_{11} = \mu(\cos^2\phi + \cos^2\theta\,\sin^2\phi) + \sin^2\theta\,\sin^2\phi$

$\mu_{12} = \mu\,\sin^2\theta\,\sin\phi\,\cos\phi + jK\cos\theta - \sin^2\theta\,\sin\phi\,\cos\phi$

$\mu_{13} = \sin\theta\,\{jK\cos\phi + \sin\phi\ \cos\theta\,(1-\mu)\}$

$\mu_{21} = \mu\,\sin^2\theta\,\sin\phi\ \cos\phi - jK\cos\theta - \sin^2\theta\,\sin\phi\,\cos\phi$

$\mu_{22} = \mu(\sin^2\phi + \cos^2\theta\,\cos^2\phi) + \sin^2\theta\,\cos^2\phi$

$\mu_{23} = \sin\theta\,\{jK\sin\phi - \cos\theta\,\cos\phi\,(1-\mu)\}$

$\mu_{31} = (1-\mu)\,\sin\theta\,\cos\theta\,\sin\phi - jK\sin\theta\,\cos\phi$

$\mu_{32} = -jK\sin\phi\,\sin\theta - (1-\mu)\,\sin\theta\,\cos\phi\,\cos\theta$

$\mu_{33} = \mu\,\sin^2\theta + \cos^2\theta$

4.1.2 Dispersion Relation

Consider the propagation of magnetostatic waves in a dielectric layered structure which consists of a YIG film of thickness d, separated from a metal by a dielectric layer of thickness t, as shown in Figure 43. The z-axis of the unprimed coordinate system was assumed to be oriented perpendicular to the plane of the film. The internal dc field (as well as the dc magnetization) was directed along the z'-axis of the primed coordinate system, as shown in Figure 42. In general, the internal dc field H is different from the applied field H_o on account of demagnetization (Figure 44). The two are related as

$$H_o \sin\eta = H \sin\sigma \ , \ \sin(\sigma - \eta) = \frac{4\pi M_o \sin 2\sigma}{2H_o} \quad [35]$$

where η and σ are the angles between $\bar{H}_o$, $\bar{H}$, and the normal to the film, respectively. The magnetostatic wave propagates in the x-direction (Figure 43) and has a uniform field distribution in the transverse direction (y-axis). The analysis was carried out using the magneto-static approximation. The magnetostatic potentials in different regions can be written as

$$\psi^{air} = \exp(-\beta Z) \exp(-j\beta x) \quad [36]$$

$$\psi^{YIG} = [A_1 \exp\{j (p + (p^2-n^2)^{1/2}) z\} + A_2 \exp\{-j ((p^2-n^2)^{1/2}-p) z\}] \\ \times \exp(-j\beta x) \quad [37]$$

$$\psi^{dielectric} = [C_1 \exp(\beta z) + C_2 \exp(-\beta z)] \exp(-j\beta x) \quad [38]$$

where A_1, A_2, C_1, and C_2 are arbitrary constants, while p and n are given by

$$p = \beta \frac{1 - \mu}{\mu_{33}} \sin\theta \cos\theta \sin\phi \quad [39]$$

END

FILMED
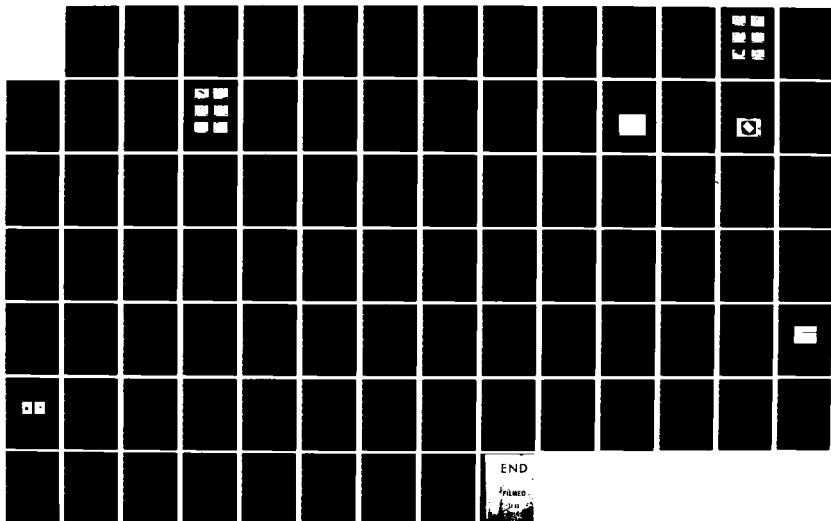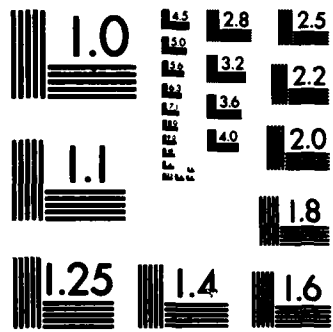
MICROCOPY RESOLUTION TEST CHART

NATIONAL BUREAU OF STANDARDS-1963-A

Dwg. 7775A54
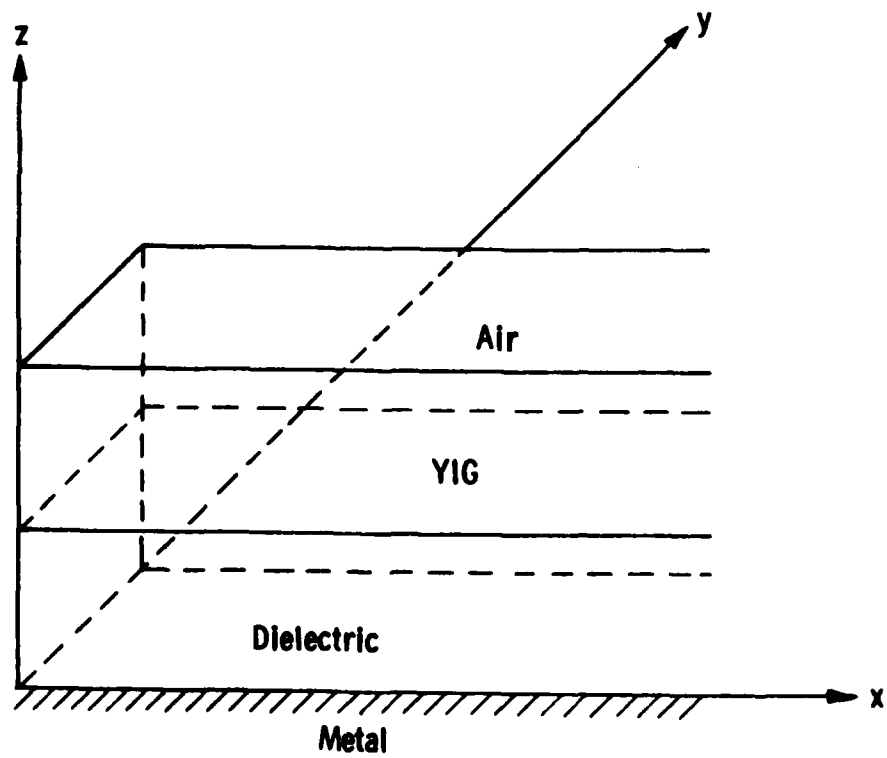
Figure 43.   The metal-dielectric-YIG layered structure.
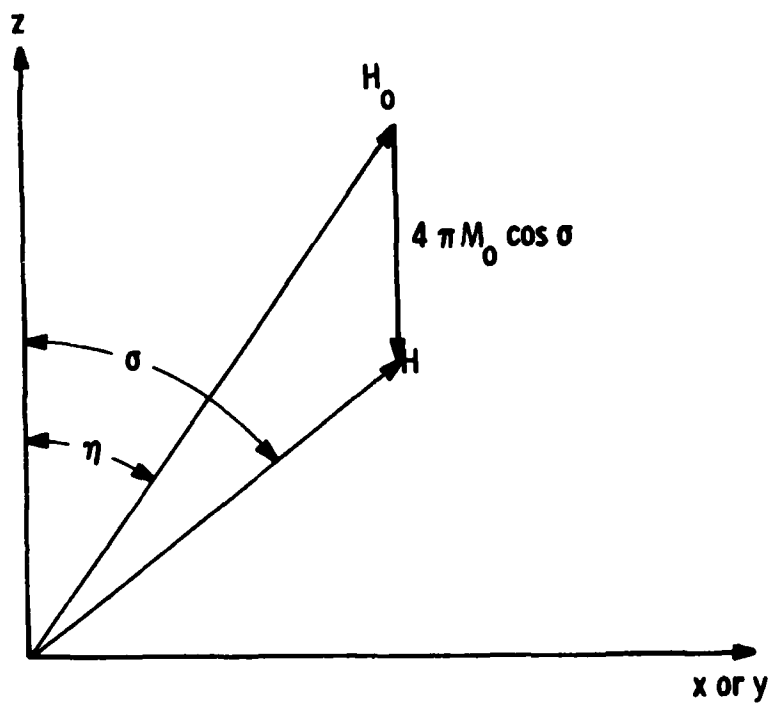
Figure 44. Relationship between applied magnetic field (H_0) and
internal magnetic field (H).

$$n = [\beta^2 \, \mu_{11}/\mu_{33}]^{1/2} \tag{40}$$

and β represents the wave number.

On satisfying the appropriate boundary conditions at each interface, the dispersion relation was obtained as

$$\cot(\beta \, \alpha \, d) = [k \, \sin\theta \, \cos\phi \, (1-\coth \beta t) + \coth(\beta t) \, \{(\mu_{33}\alpha)^2 +$$
$$(K \, \cos\phi \, \sin\theta)^2\} \, -1]/[\mu_{33} \, \alpha \, (1 + \coth \beta t)] \tag{41}$$

where
$$\alpha = \frac{(p^2 - n^2)^{1/2}}{\beta} \tag{42}$$

4.1.3 Frequency Limits

In the case of guided volume waves, α is required to be positive; this leads to the frequency of allowed modes as $\omega_1 < \omega < \omega_3$, where

$$\omega_1 = [\omega_o(\omega_o + \omega_m \sin^2\theta \, \cos^2\phi)]^{1/2} \tag{43}$$

$$\omega_3 = [\omega_o \, (\omega_o + \omega_m)]^{1/2}$$

The transition frequency between forward-volume wave to backward-volume wave is obtained as

$$\omega_2 = [\omega_o \, (\omega_o + \omega_m \sin^2\theta)]^{1/2} \tag{44}$$

The backward and forward waves are obtained in the range $\omega_1 < \omega < \omega_2$ and $\omega_2 < \omega < \omega_3$, respectively.

4.1.4 Group Velocity

The expression for the component of velocity of pulse propagation in the direction of phase propagation is obtained by

82

differentiating the dispersion relation. Rewriting Equation 41 as
$F(\beta,\omega) = 0$ we have $V_g = \frac{\partial \omega}{\partial \beta} = -\frac{\partial F}{\partial \beta}/\frac{\partial F}{\partial \omega}$, which yields

$$V_g = [\mu_{33}\ d\alpha^2\ (1 + \coth(\beta t))\ \mathrm{cosec}^2\ (\beta\alpha d) + t\ \mathrm{cosech}^2(\beta t)\ \{\mu_{33}\alpha\ \cot(\beta\alpha d) +$$

$$\kappa\ \sin\theta\ \cos\phi - \mu_{33}^2\alpha^2 - \kappa^2\cos^2\phi\ \sin^2\theta\}]/$$

$$[-\beta\alpha'd\mu_{33}\alpha(1+\coth(\beta t))\ \mathrm{cosec}^2(\beta\alpha d)+\cot(\beta\alpha d)\ \{(1+\coth(\beta t))(\mu_{33}\alpha' + \mu'_{33}\alpha)\}-$$ $\quad$ [45]

$$\kappa'(1-\coth(\beta t))\sin\theta\cos\phi-2\coth(\beta t)\{\mu_{33}\alpha(\mu_{33}\alpha'+ \alpha\mu'_{33})+ \kappa\kappa'\ \cos^2\phi\sin^2\theta\}]$$

where primes denote derivatives with respect to ω

$$\alpha' = \frac{1}{2\alpha}\ [\{-2(1-\mu)\frac{(\sin\theta\cos\theta\sin\phi)^2}{\mu_{33}}\}\ (\frac{(1-\mu)\mu_{33}'}{\mu_{33}^2} + \frac{\mu'}{\mu_{33}}) + \frac{\mu_{11}\mu_{33}'}{\mu_{33}^2} - \frac{\mu_{11}'}{\mu_{33}}] \qquad [46]$$

$$\mu' = \frac{2\omega_o\ \omega_m\ \omega}{(\omega_o^2 - \omega^2)^2} \qquad\qquad [47]$$

$$\kappa' = \frac{\omega_m\ (\omega^2 + \omega_o^2)}{(\omega_o^2 - \omega^2)^2} \qquad\qquad [48]$$

$$\mu_{33}' = \mu'\ \sin^2\theta \qquad\qquad [49]$$

$$\mu_{11}' = (\cos^2\phi + \cos^2\theta\ \sin^2\phi)\ \mu' \qquad\qquad [50]$$

The group delay time per unit distance of propagation is the reciprocal of group velocity.

4.1.5 Specific Cases

When $\theta = 0^\circ$, Equations 41 and 45 reduce the relations obtained by Miller[20] and Bardai et al.[5] When $\theta = 90^\circ$ (ϕ arbitrary), Equations 41 and 45 reduce to the ones obtained by Miller[16] for the

case of arbitrary magnetization in the plane of the film. In the case when $\phi = 0^{\circ}$ (θ arbitrary), Equations 41 and 45 reduce to the corresponding expressions obtained by Miller[17] for the case of arbitrary magnetization in the transverse plane.

4.2 Experimental Results

Experiments were done using the computer-controlled network analyzer (HP 8409) and an electromagnet (Varian). The YIG film was 20 μm thick and 5 mm wide and a ground plane was separated from the YIG by a 635 μm thick alumina wafer. The transducers were 50 μm wide gold lines deposited on the alumina and separated by 1 cm. The sample was mounted on a two-axis rotating jig which had graduated drums and verniers. Angles between the external magnetic field and the normal to the YIG film could be set and measured to ± 1/2 degree. As is obvious from Equation 35, the internal angle and internal magnetic field are different for different orientation of applied magnetic field. Figure 45 shows the variation of internal angle and internal field with external angle for a fixed applied magnetic field.

4.2.1 Forward-Volume-to-Surface Waves

In this section, we present the experimental and theoretical results of the variation of delay and transmission loss with frequency, when the applied field is rotated in the plane containing the normal to the film and the in-plane normal to the direction of wave propagation. To correlate with theory, $\theta = 360 - \sigma$ in this plane.

Figures 46a to f show the variation of group delay with frequency for different orientations of applied magnetic field ($\phi = 0^{\circ}$, θ varying) in the plane. As θ varies, the orientation of the magnetic field changes, therefore the frequency limits of the passbands also shift. It is obvious from the delay curves that there is good agreement between computed and measured delay results in the regions of interest (i.e., slightly above the lower cutoff frequency, where delay has

84

Curve 741865-A
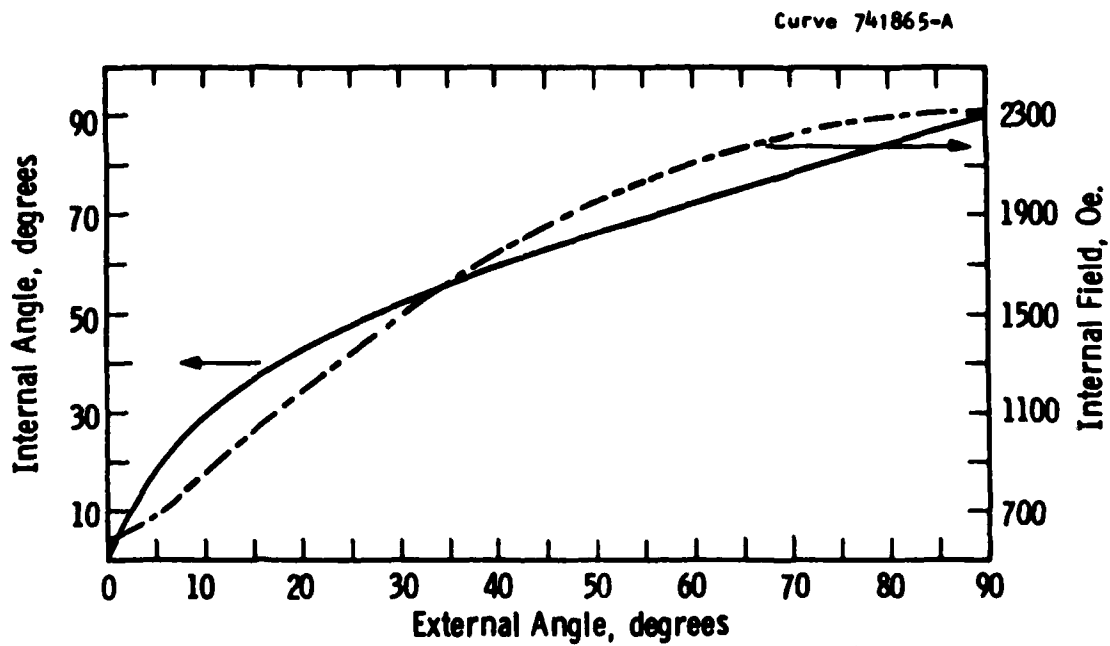
Figure 45. Variation of internal angle and internal magnetic field with external angle for applied magnetic field (H_o) = 2320G.

85

Curve 741886-B
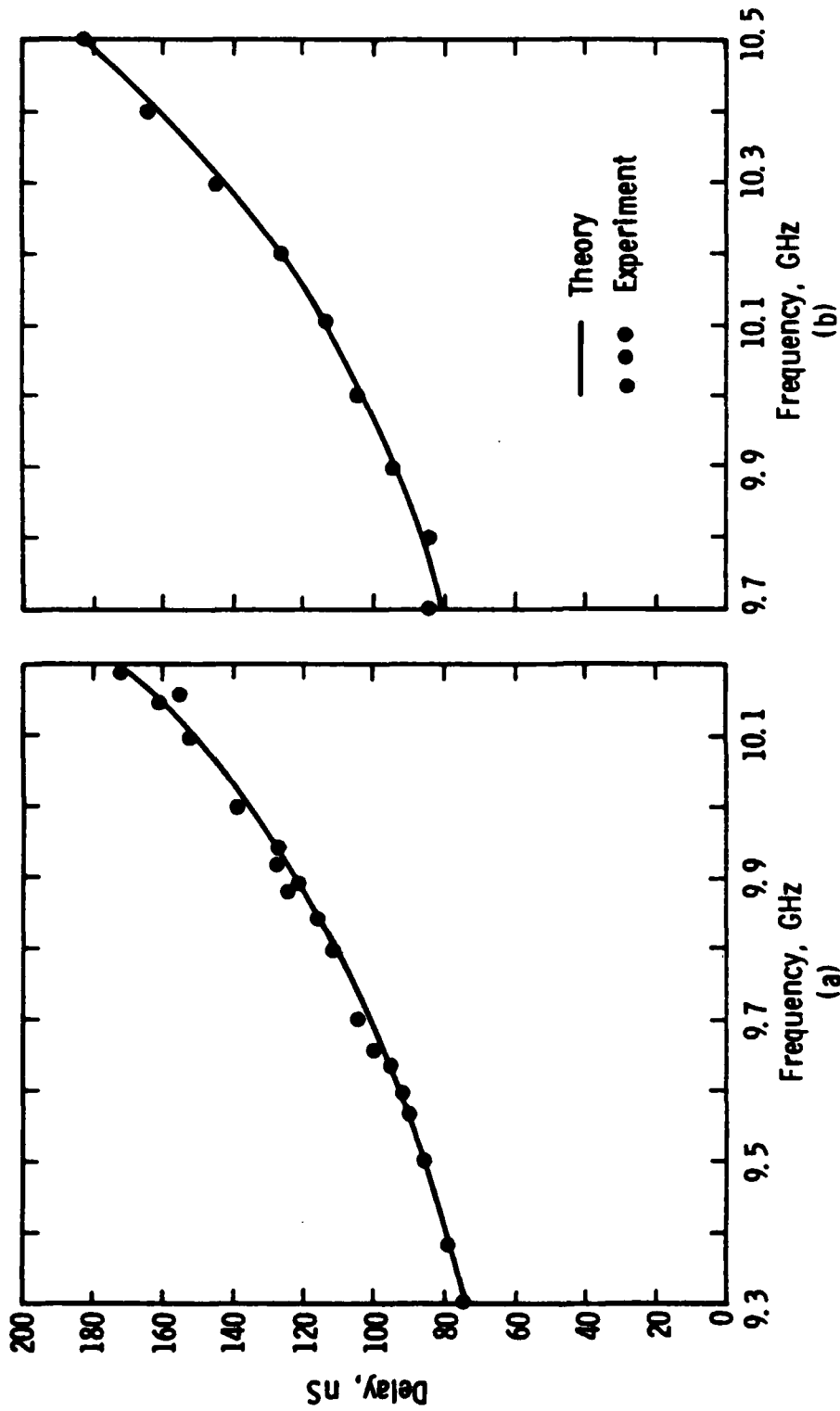
Figure 46a. Variation of calculated and measured delay with frequency for $\eta = 0$. The other parameters are: $H_o = 4975G$, $t = 635\ \mu m$, $d = 20\ \mu m$, and $4\pi M_o = 1750$ gauss.

Figure 46b. Variation of calculated and measured delay with frequency for $\eta = 10^o$ and $H_o = 4920G$. The other parameters are the same as for Figure 46a.

86
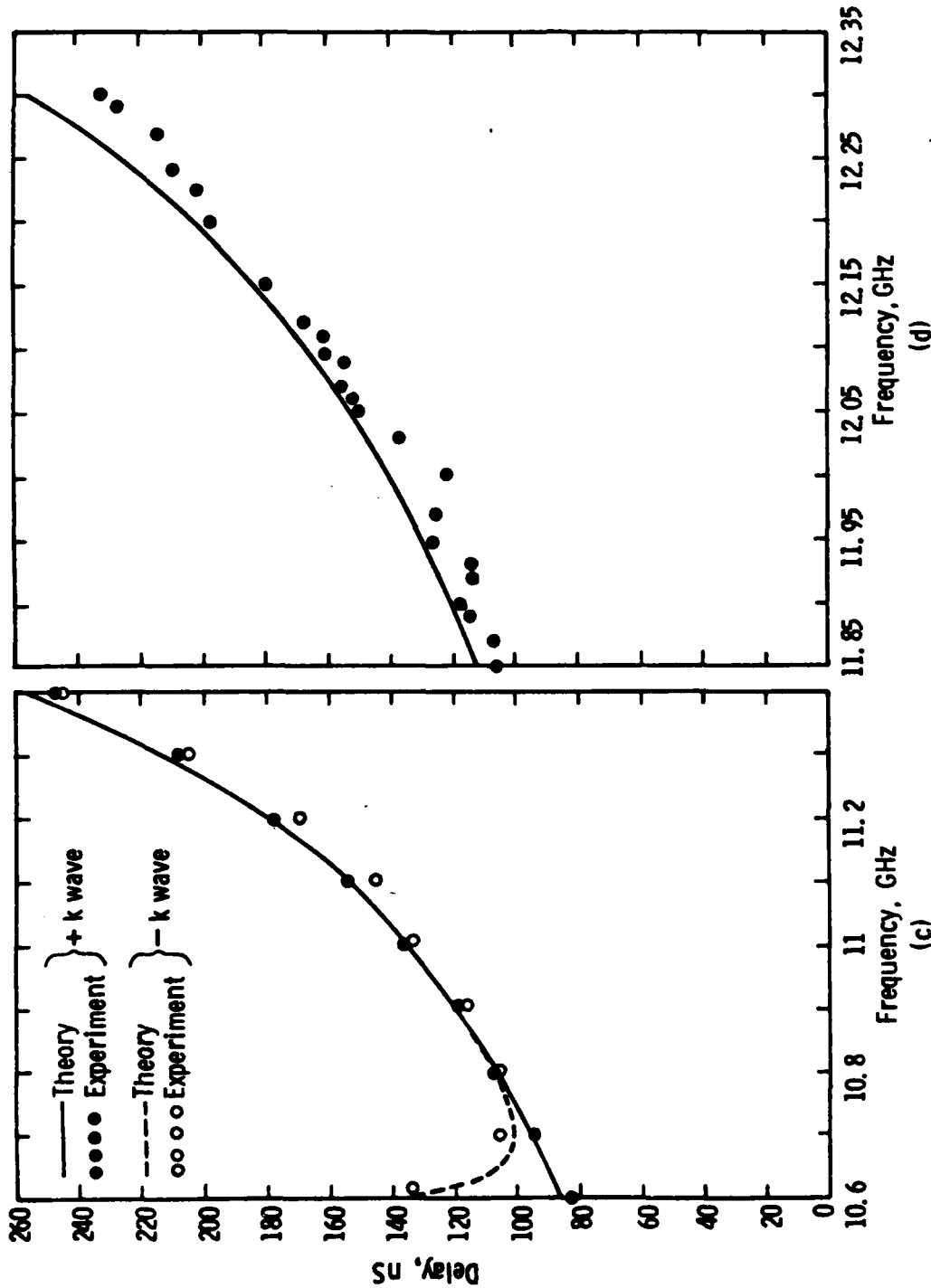
Figure 46c. Variation of calculated and measured delay with frequency for $\eta = 20°$ and $H_0 = 4905G$. The other parameters are the same as for Figure 46a.

Figure 46d. Variation of calculated and measured delay with frequency for $\eta = 30°$ and $H_0 = 4905G$. The other parameters are the same as for Figure 46a.

87

Curve 741884-B
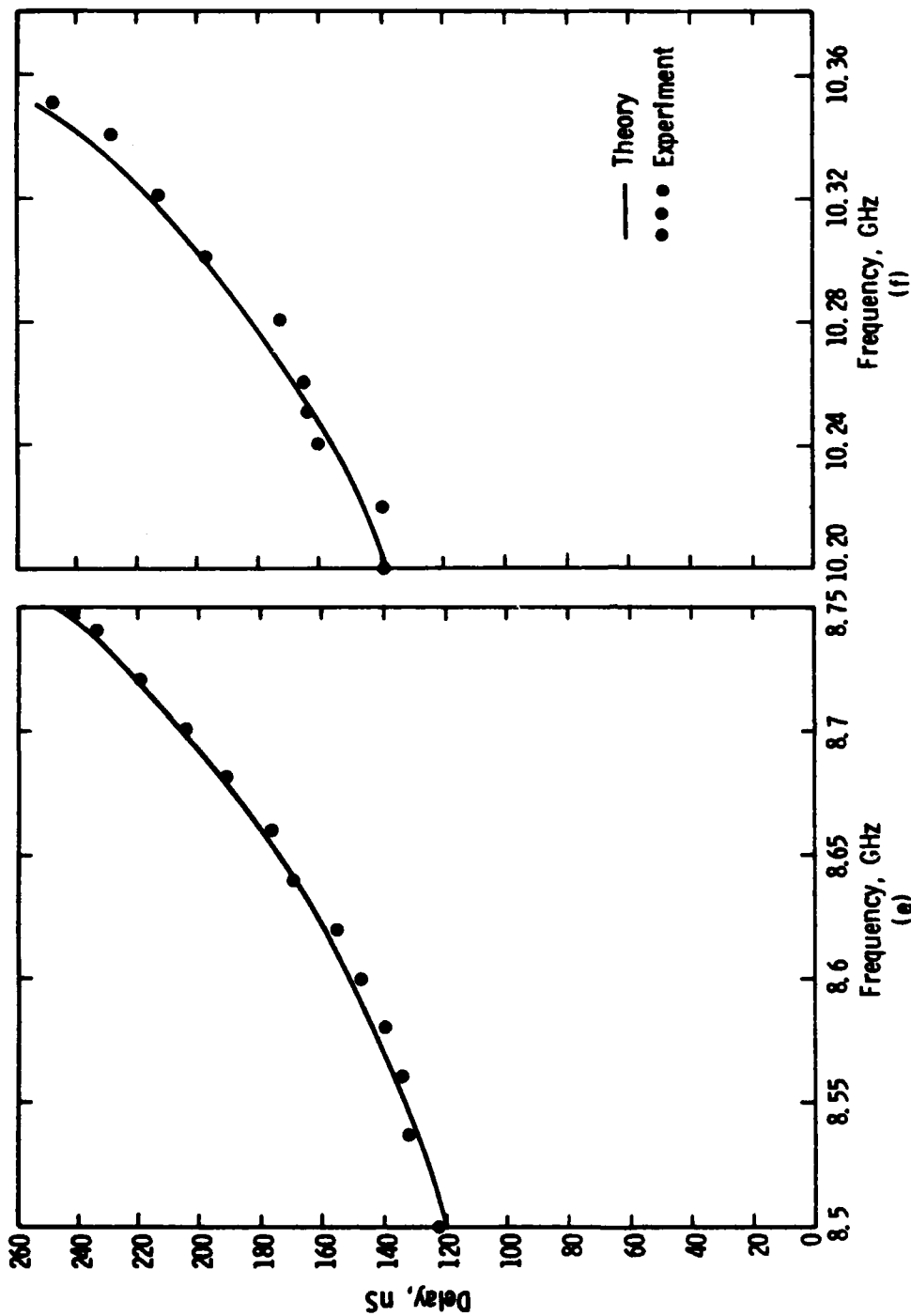
Figure 46e. Variation of calculated and measured delay with frequency for $\eta = 40°$ and $H_0 = 3140G$. The other parameters are the same as for Figure 46a.

Figure 46f. Variation of calculated and measured delay with frequency for $\eta = 60°$ and $H_0 = 3150G$. Other parameters are the same as for Figure 46a.

88

ripples). In this plane, the delay characteristics are nonreciprocal, as seen from Equation 45. The nonreciprocal delay is shown theoretically and experimentally in Figure 46c, where the positive wave propagation and negative wave propagation show different delay for the lower frequencies in the band.

The transmission loss for the different orientations of magnetic field for Figures 46a to f, as recorded on the HP 8910B network analyser, is shown in Figures 47a to f, respectively. It is obvious from the transmission photographs that the transition from volume to surface wave is continuous; this confirms the theoretical results obtained by Koike.[21] The internal magnetic field H used in the calculations was measured from the edge of the transmission loss response. It is necessary to mention here that theoretical results obtained by Miller[17] are correct and this is a correction to the statements made to Koike.[21]

4.2.2 Forward to Backward-Volume Waves

It is known that forward or backward waves are excited when the magnetic field is normal or lies in the plane (parallel to propagation vectors), respectively. But if the direction of magnetic field is arbitrary in the plane containing the normal to the YIG film and direction of propagation vector, backward and forward waves are excited. Thus, as θ increased from 0° to 90°, the dispersion characteristics should change from forward to backward. The backward (forward) waves occur in the lower (higher) frequency region. The transition from backward to forward waves is abrupt and occurs at frequency ω_2, given by Equation 44. The backward and forward waves are obtained in the range $\omega_1 < \omega < \omega_2$ and $\omega_2 < \omega < \omega_3$, respectively. It follows from Equation 44 that as θ increases from 0° to 90°, ω_2 increases from ω_1 to ω_3. Consequently, the backward wave region grows at the expense of the forward wave region.

89
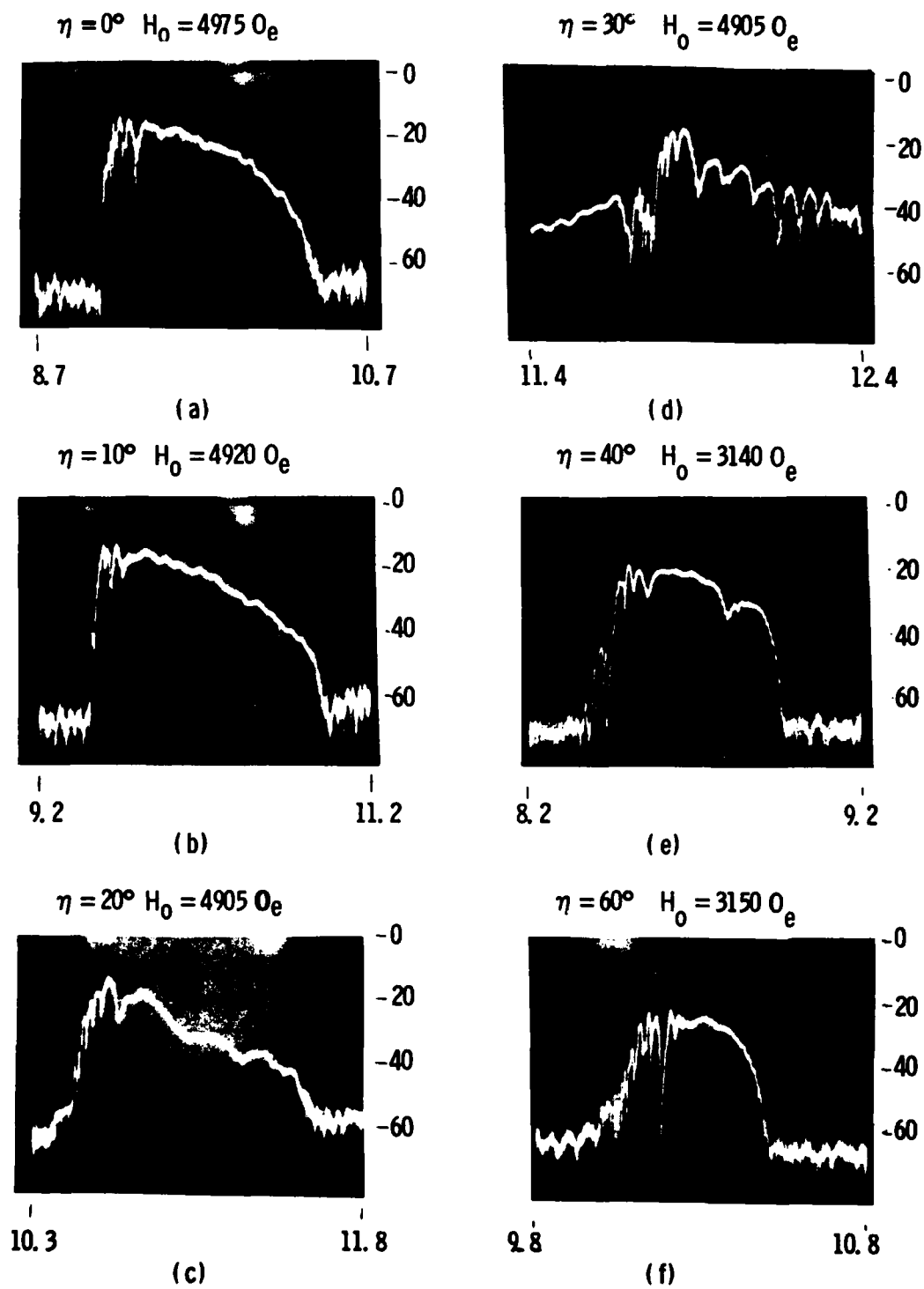
Figure 47. Transmission response, for various angles between the normal to the film and H_o, for the forward-to-surface wave plane. Horizontal axis: Frequency in GHz. Vertical axis: Transmission loss in dB.

90

Curve 741882-B

— Forward Wave (Theory)
---- Backward Wave
••• Experiment
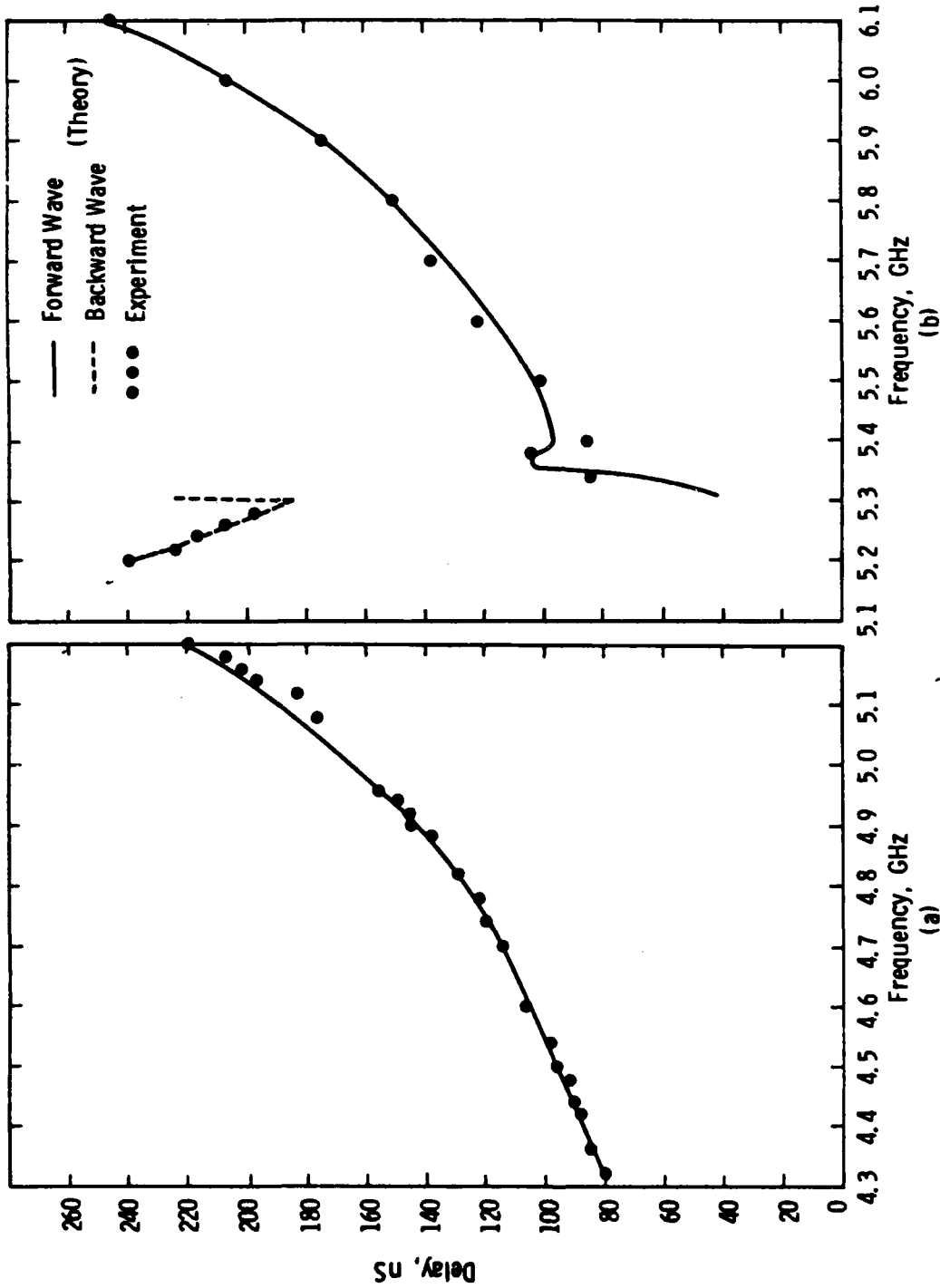
Figure 48a. Variation of calculated and measured delay with frequency for $\phi = 90^o$, $\eta = 0^o$ and $H_o = 3180G$. The other parameters are the same as for Figure 46a.

Figure 48b. Variation of calculated and measured delay with frequency for $\phi = 90^o$, $\eta = 15^o$ and $H_o = 3110G$. The other parameters are the same as for Figure 46a. $\omega_2 = 5.31$ GHz.

91
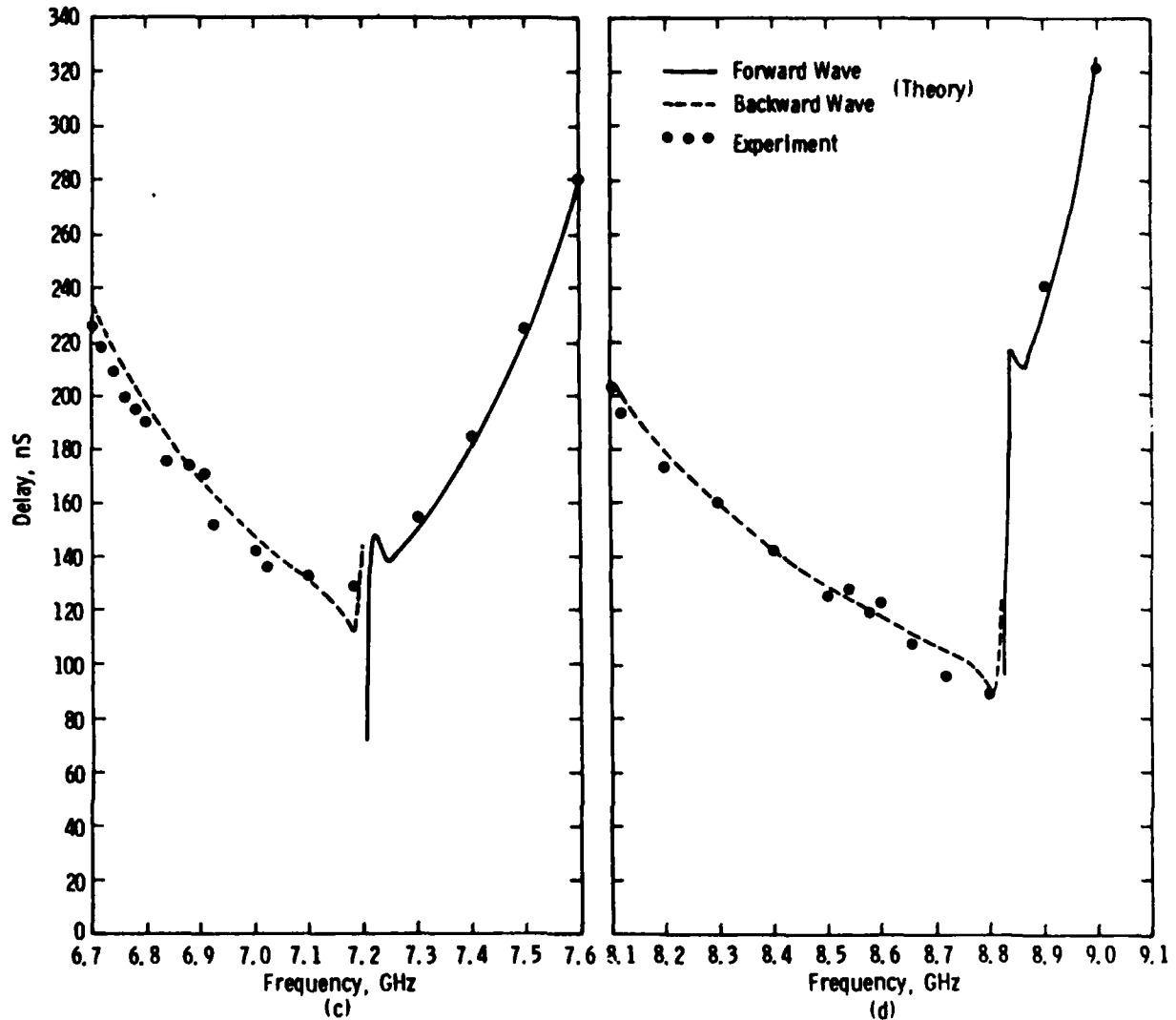
Figure 48c. Variation of calculated and measured delay with frequency for $\phi = 90^\circ$, $\eta = 30^\circ$ and $H_o = 3100G$. The other parameters are the same as for Figure 46a. $\omega_2 = 7.19$ GHz.

Figure 48d. Variation of calculated and measured delay with frequency for $\phi = 90^\circ$, $\eta = 45^\circ$ and $H_o = 3140G$. The other parameters are the same as for Figure 46a. $\omega_2 = 8.82$ GHz.
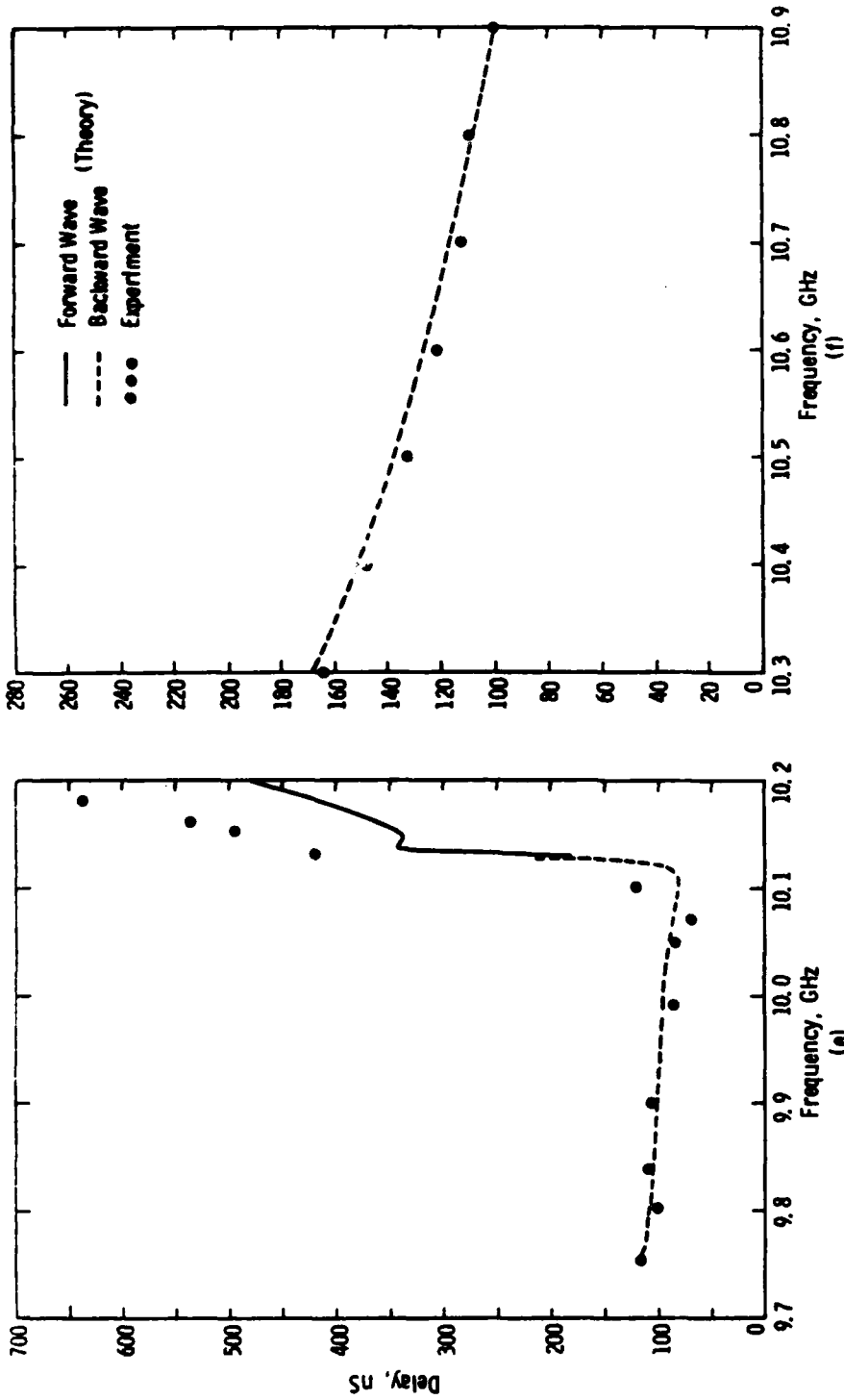
Figure 48e. Variation of calculated and measured delay with frequency for $\phi = 90°$, $\eta = 60°$ and $H_0 = 3170G$. The other parameters are the same as for Figure 46a. $\omega_2 = 10.13$ GHz.

Figure 48f. Variation of calculated and measured delay with frequency for ϕ, $\eta = 90°$ and $H_0 = 3170G$. The other parameters are the same as for Figure 46a.

93

Figures 48a to f show variations of group delay (nS/cm) with frequency when the applied magnetic field H_0 is applied at 0°, 15°, 30°, 45°, 60°, and 90° angles, respectively. As described above, the bandwidth contains forward waves at 0°, backward and forward waves for angles larger than 0° and less than 90°, and only backward at 90°. For the plane $\phi = 90^\circ$, $\theta = \sigma$, the propagation is reciprocal since the expression for group velocity, i.e., Equation 45, does not involve κ at all. It is seen from Figures 48a to f that there is good agreement between theoretical and experimental delay values. Moreover, the transition frequency (ω_2) calculated from theory also agrees with experiment. Overall, the physical nature of delay as predicted by theory is confirmed by experiment.

The transmission loss for the different orientations of magnetic field for Figures 48a to f as recorded is shown in Figures 49a to f, respectively. It is confirmed from these photographs that as η increases from 0°, the backward and forward regions appear. The backward wave region grows at the expense of the forward wave region.

4.2.3 Adjustable Delay

A pottially useful device which may result from the present study of magnetostatic wave propagation in an arbitrary magnetic field is a variable delay line. Figure 50 shows the measured and calculated variation of a "constant" delay line with magnitude and direction of the internal magnetic field. Here, the bias field strength was adjusted for each angle so as to maintain a "constant" delay region in a fixed frequency range (8.75 to 8.9 GHz). As can be seen, there is good agreement between calculated and measured delay.

These preliminary measurements have shown an approximately constant delay adjustable over a ± 20% range with a bandwidth of ~ 150 MHz and were obtained using a single YIG film device.

94
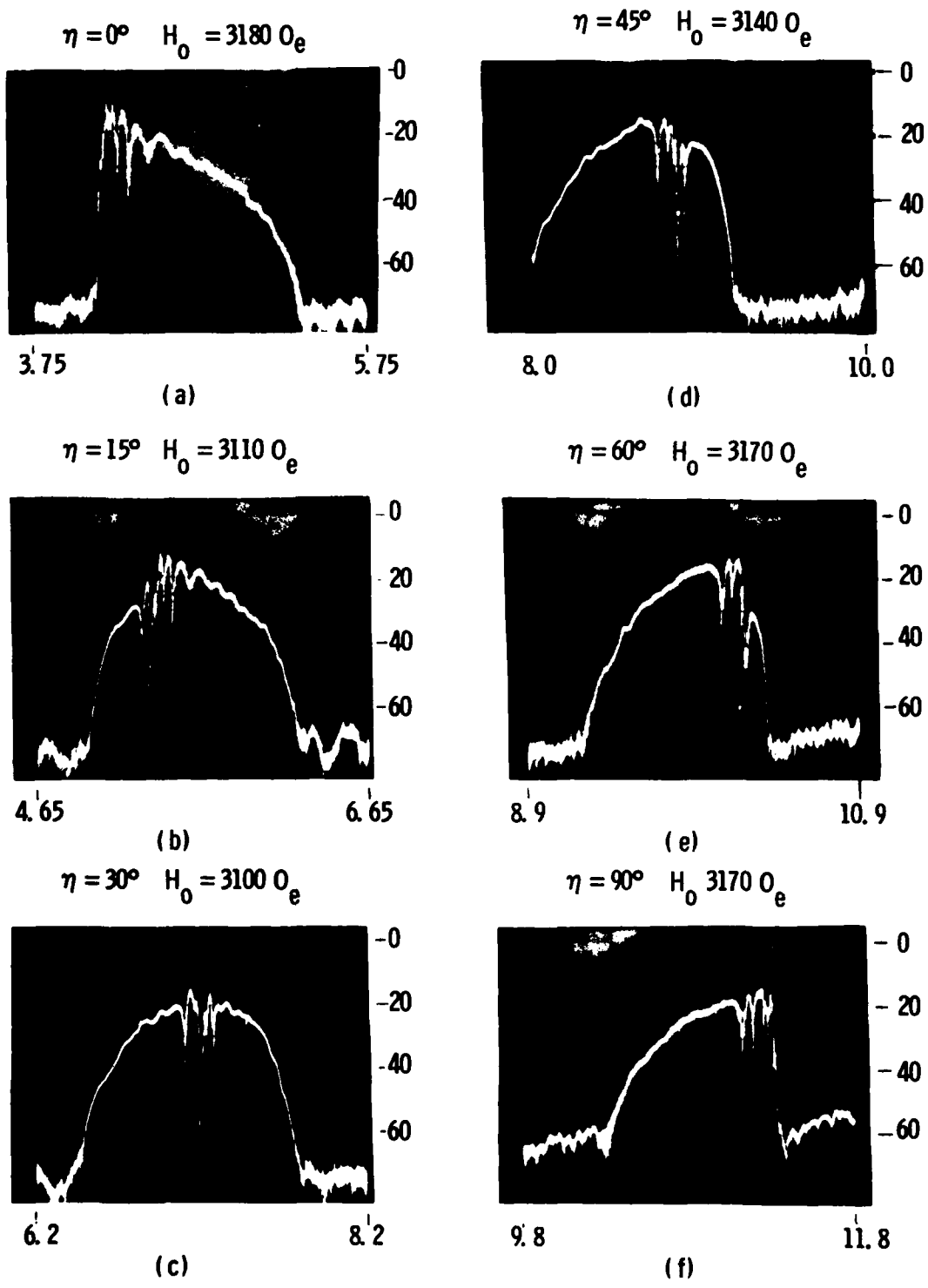
Figure 49.   Transmission response for various angles between the normal
             to the film and H_o for the forward to backward plane.
             Horizontal axis: frequency in GHz. Vertical axis:
             transmission loss in dB.
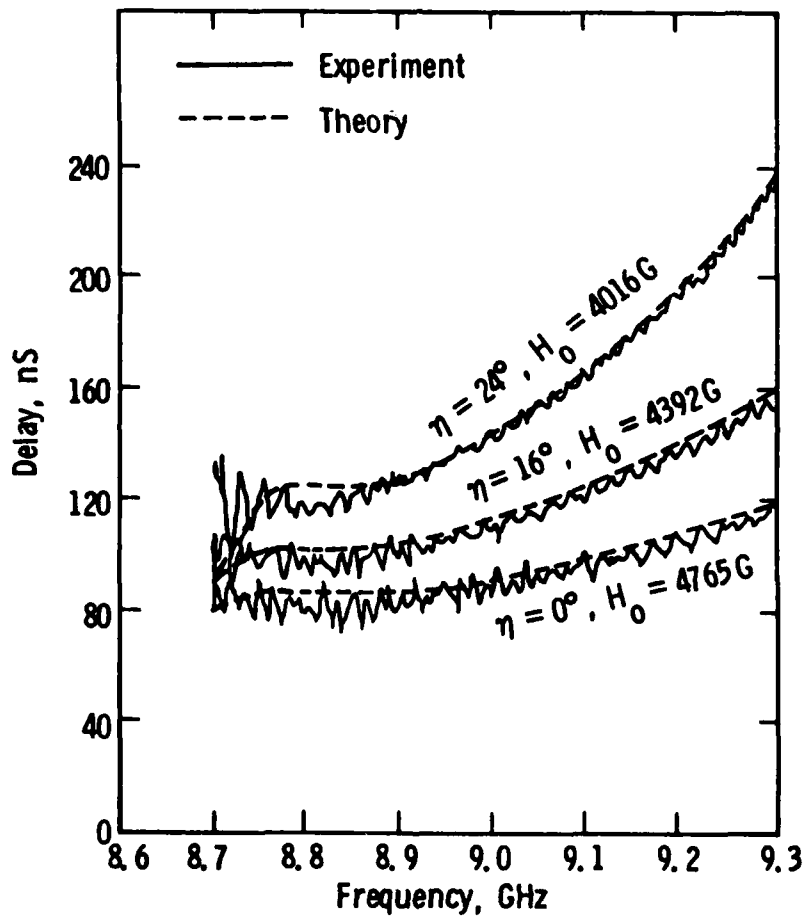
Figure 50. Variation of measured and calculated delay with the magnitude and direction of internal magnetic field at a frequency without changing t. The parameters are $t = 127$ μm, $d = 20$ μm, $4\pi M_o = 1750$ gauss.

5. BEAM STEERING

Magnetostatic forward-volume wave (MSFVW) delay lines commonly show undesirable amplitude and phase ripple. Several possible causes have been identified and steps taken to minimize their effects. However, there remains ripple with a long period which becomes more severe in thick films. Its origin is so far unexplained. In addition, measurements on as-grown YIG films showed an unexpected increase in transmission loss at low wave numbers. In this range, the return loss from the transducer and, hence, the transduction efficiency, was very large. This is illustrated in Figures 51a and 51b, which show the transmission response measured over a 1 cm pathlength on 2-inch diameter YIG films of thickness 10.1 μm and 75 μm, respectively. The transducers were each 1 cm long and 50 μm wide and were terminated by an open circuit. Note that the minimum transmission loss is approximately the same in both films, although the group delay in the 10.1 μm thick film is roughly seven times longer than in the 75 μm thick film. Assuming that a wave number dependent loss process is not present, it was concluded that magnetostatic waves were being efficiently launched, but the wave beam was not completely intercepted by the output transducer.

In recent years, the results of several investigations on the steering of magnetostatic waves have been reported in the literature.[3,22-26] Regarding MSFVW, an unexpected beam-steering angle of the order of 15° has been observed when the sample was aligned normal to the field. This observation has been explained in terms of the existence of an in-plane component of the internal magnetic field,[24] which would make the latter deviate from a direction normal to the YIG film.
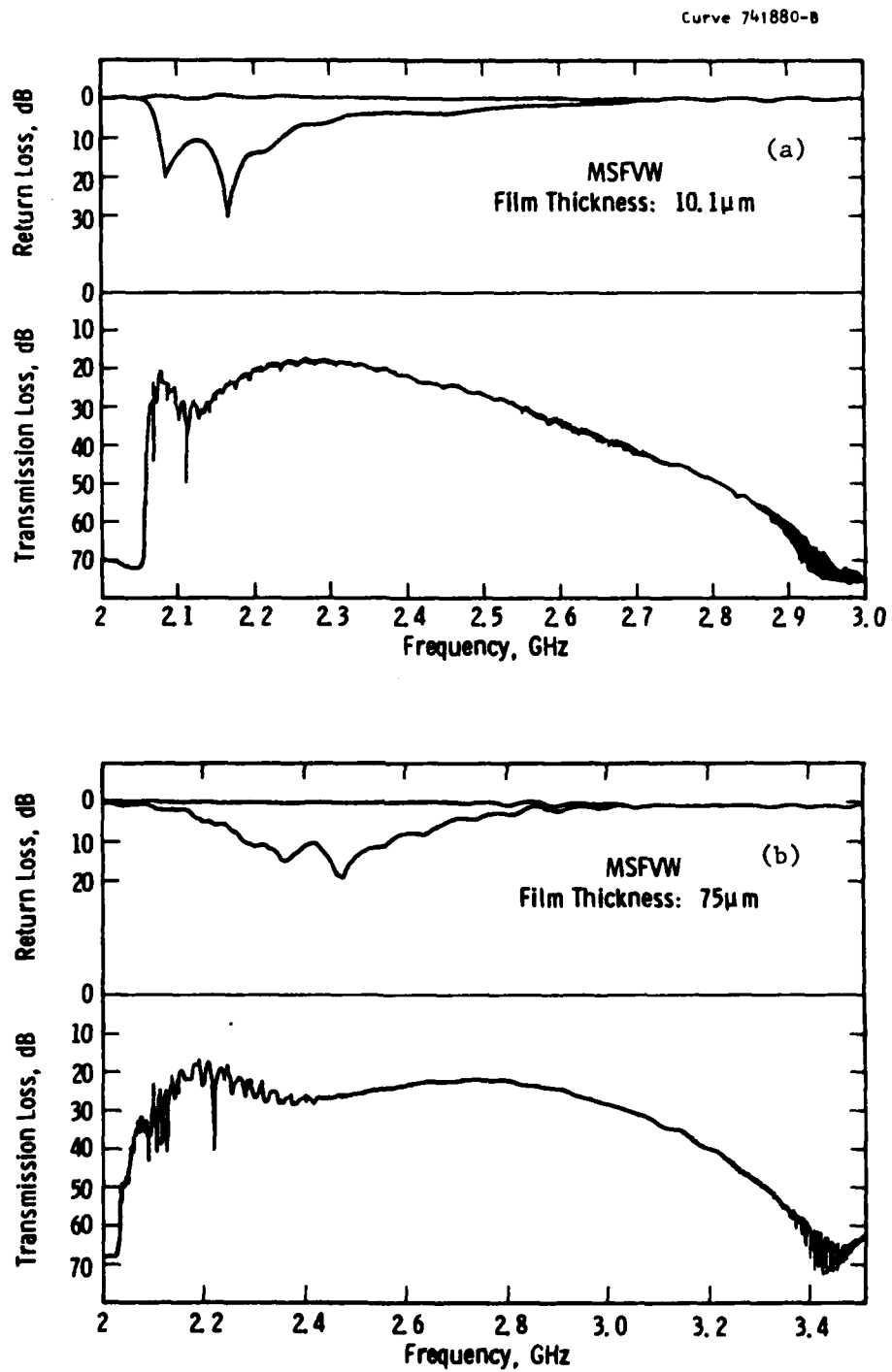
Figure 51. Reflection and transmission responses for MSFVW measured over a 1 cm pathlength on 2-inch diameter YIG films of two different thicknesses: (a) 10.1 μm, (b) 75 μm.

98

However, the presence of such an in-plane magnetic-field component has not been established as yet, nor is it clear at this point what the origin of such a component might be.

Moreover, other factors may contribute to beam steering as well, such as nonuniformities in the YIG film thickness, in the ground plane spacing, and in the applied magnetic-field strength. Also, the possibility exists that steering may be introduced at the transducer, perhaps due to a phase difference between the magnetostatic waves excited at opposite ends of the transducer or by diffraction effects.

In this section, we shall then be concerned with a study of the beam steering in magnetostatic forward-volume waves. As it has been demonstrated by Smith et al.,[3,24] a small component of the internal magnetic field on the plane of the YIG film would cause significant beam steering. Therefore, the different physical phenomena which could give rise to such an in-plane component are reviewed in the next subsection.

The greater part of this section, however, will be devoted to measurements of beam steering performed on a 2-inch YIG wafer by means of a 0.007-inch diameter loop-probe.

5.1 The In-Plane Component

In searching for the cause of an in-plane component of the internal magnetic field, we have examined the effects in YIG films of the magnetocrystalline anisotropy, the stress-induced anisotropy, and the shape anisotropy.

(a) The magnetocrystalline anisotropy energy in YIG is given by

$$E_{mag} = K_1(\alpha_1^2\alpha_2^2 + \alpha_2^2\alpha_3^2 + \alpha_3^2\alpha_1^2) + K_2(\alpha_1^2\alpha_2^2\alpha_3^2 + \ldots) \qquad [51]$$

where K_1 and K_2 are the first and second order anisotropy constants, respectively. The α's are given by

$$\alpha_1 = \sin\theta \cos\phi, \ \alpha_2 = \sin\theta \sin\phi, \ \alpha_3 = \cos\theta$$

99

where ϕ and θ are the first two Eulerian angles the magnetization makes with the cubic lattice's edges.

The direction in which this energy is minimum is obtained by differentiating equation 51 with respect to θ and ϕ. This direction is found to be perpendicular to the plane of the YIG film, i.e., <111>.

We conclude then that no in-plane component results from magnetocrystalline anisotropy effects.

(b) The stress-induced anisotropy energy in the plane of the film (i.e., the <111> plane) is given by[25]

$$E_{st} = \lambda_{111} \; \sigma [\alpha_1 \alpha_2 + \alpha_2 \alpha_3 + \alpha_3 \alpha_1] \qquad [52]$$

where the α's were defined in (a), λ_{111} is the saturation magnetostriction constant, and σ is the uniaxial stress in the film. An isotropic stress, which is anticipated in epitaxial films, can be represented as two orthogonal uniaxial stresses.

Again, the <111> direction is that of minimum energy so that stress does not contribute to an in-plane component of the internal magnetic field.

(c) The combined effects of magnetocrystalline, stress-induced, and shape anisotropies[26] was considered next for σ in the (111) plane. The shape anisotropy energy E_s arises from the demagnetizing effects of magnetic poles. For a thin film of magnetization, $4\pi M_o$, the shape energy is given by

$$E_s = 2\pi M_o^2 \; \cos^2 \zeta \qquad [53]$$

where ζ is the angle between $4\pi M_o$ and the normal to the film plane.

The minima of the total energy are found to lie on the three {110} planes which contain the <111> axis. It follows then, by symmetry,[26] that no in-plane component of the magnetic field can exist.

We see then that the anisotropies considered above do not appear to contribute an in-plane component of the magnetic field.

On the other hand, an in-plane component could be expected to arise from the misorientation of the GGG substrate surface with respect to its <111> direction. From the manufacturer's data on the GGG substrates, the misorientation is within $\pm 0.2^{o}$. For a magnetic field applied normal to the YIG surface, the internal field would then lie at an angle with the normal smaller than 0.2^{o}. This, however, results in an in-plane component of only 0.2 to 0.3% of the magnitude of the internal field. From the experimental results reported in reference 24, we conclude that this small value is not expected to give rise to appreciable beam steering.

5.2 Beam-Steering Measurements

Measurements of beam steering for magnetostatic forward-volume waves have been performed by means of a 0.007-inch diameter loop-probe. The loop has been made at one end of a 2-inch long coaxial cable, the inner and outer conductor diameters being 0.002 and 0.008 inch, respectively.

On the opposite end of the coaxial cable, a connection has been made to an OSM female connector (Figure 52a).

In order to provide mechanical protection to this arrangement, the coaxial cable has been placed inside an alumina tube of approximately 0.160 inch in diameter. The tube is slightly shorter than the cable, so that the loop is visible at one end and can be brought in close contact with the YIG surface. The loop-probe itself has been potted with a drop of "Duco" cement for mechanical protection. The layer of "Duco" cement directly above the probe is estimated to be around 1 to 2 mils thick.

At the opposite end of the alumina tube, a female OSM connector flange has been attached (Figure 52b), which is then bolted to the OSM connector at the end of the cable (Figure 52c).

101

Dwg. 7774A75

(a)
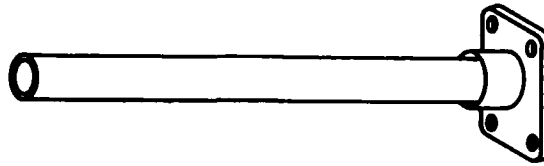
(b)
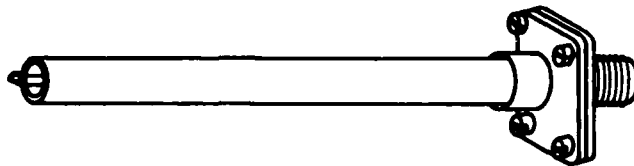
(c)

(d)

Figure 52.   The different components that make up the loop-probe setup:
(a) The coaxial cable has a loop on one end and a connection
to an OSM female connector on the other; (b) The alumina
tube with an OSM flange attached to one end; (c) The alumina
tube houses the coaxial cable; (d) The final version of the
probe setup.

RM-98200

Figure 52d shows a photograph of the final version of the probe. We have covered the alumina tube with a shielding wire sheath which was properly grounded. This was done in order to eliminate some of the feedthrough observed after preliminary measurements were made.

The alumina tube containing the probe (Figure 52d) was then passed through a hole at one end of a 0.5 x 24 inch aluminum rod and spring-loaded with a rubber band. In this fashion, the alumina tube can be positioned perpendicular to the YIG film to be measured. The spring loading insures that the tip of the probe setup of Figure 52d will remain in contact with the YIG surface when probing the fields.

The other end of the aluminum rod was attached to an XYZ micropositioner. The plane of the loop was placed parallel to the transducer for maximum coupling to the magnetostatic fields.

The magnetostatic waves were excited on a 2 inch diameter YIG wafer so as to avoid any boundary effects. The YIG film and the transducers were placed in a 2 inch x 2 inch box in a special arrangement, as shown in Figure 53a. A 1 inch x 1-1/4 inch rectangular opening was cut on the transducer alumina substrate so as to be able to probe the magnetostatic fields. We evaporated aluminum (300Å) on both the YIG and the alumina substrate around the edges of the area to be probed and the opening, respectively, in order to minimize reflections.

Probing of the fields was then performed by sliding the probe setup along the exposed YIG surface. This we coated with a layer of silicon vacuum grease to prevent abrasion of the "Duco" cement covering the probe.

The probing setup was characterized by means of swept-frequency transmission and reflection measurements in the 2 to 4 GHz range. A 50 µm thick YIG film was used. In Figure 54 we show the transmission (insertion loss) and reflection (return loss) responses for MSFVW between the transducers in the box. We see a great deal of ripple in the low to middle passband, a commonly observed feature of thick films, as pointed out in the introduction to this section.

103

Dwg. 7774A76
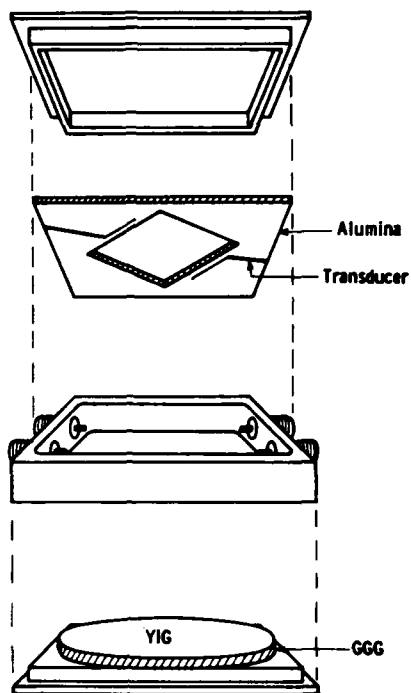
Figure 53a. The different components of the box used for beam-steering measurements.
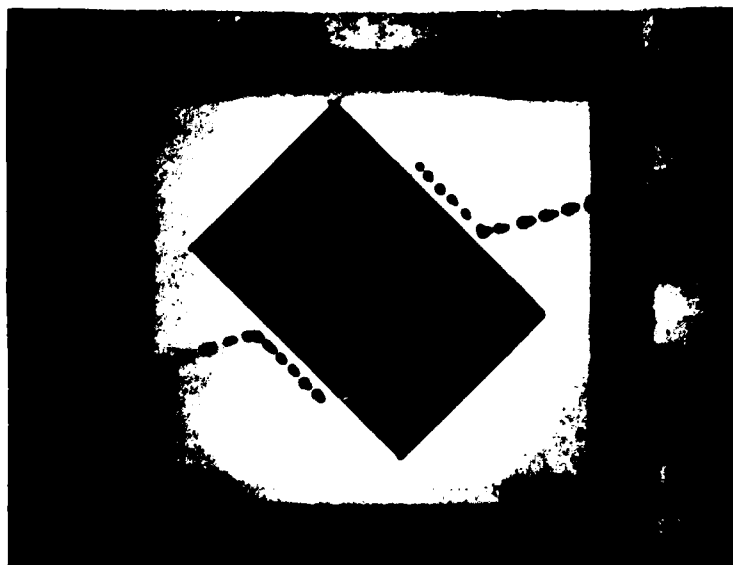
Figure 53b. Top-view photograph of the box. The black area is the YIG film. The dotted lines indicate where the transducers are on the opposite side of the alumina.

104
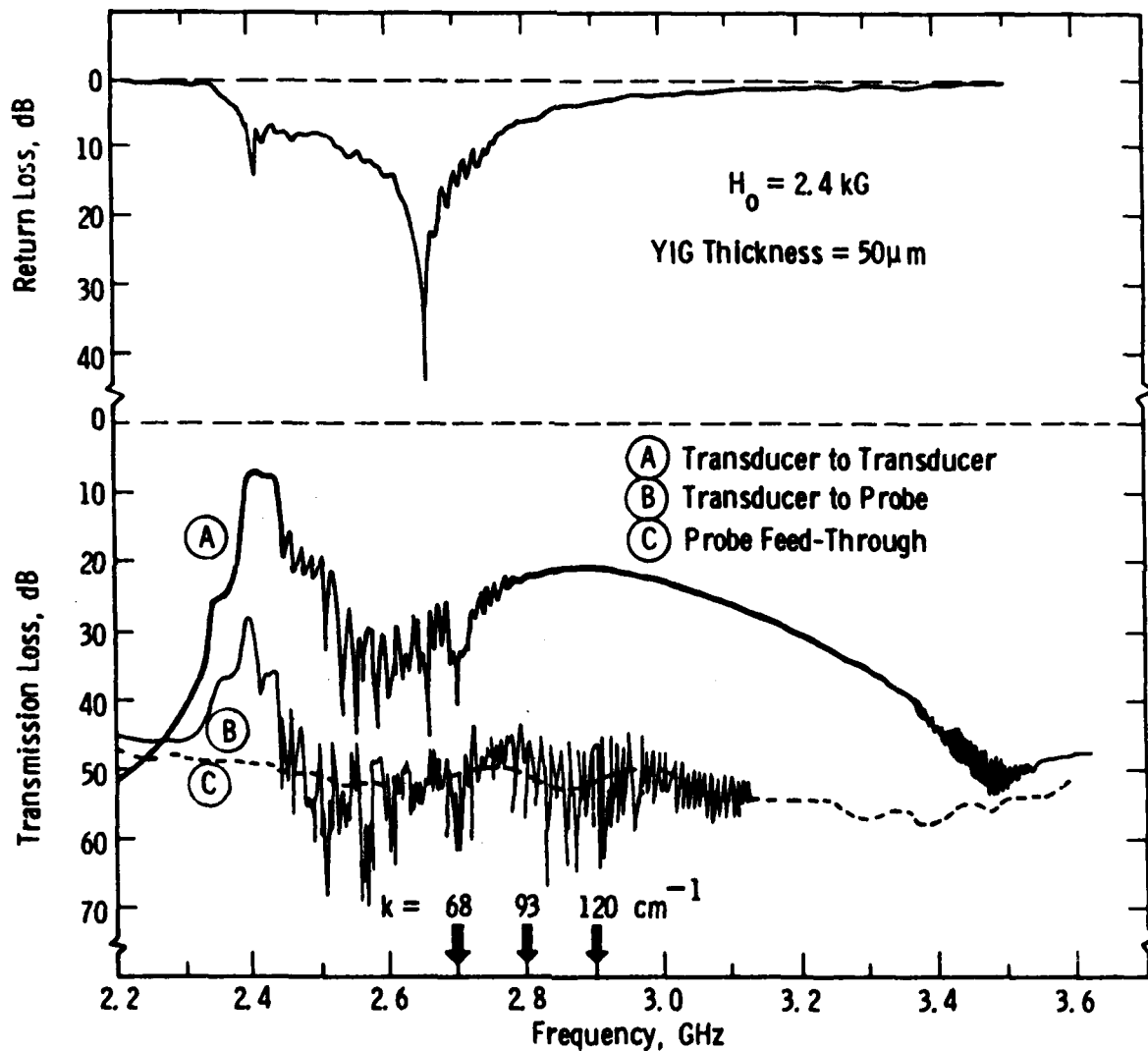
Figure 54. Return and insertion losses for the probing experimental
setup. Curves are obtained between transducers and from
transducer to probe when the latter is in the middle of the
sample. The arrows indicate those frequencies at which
beam-steering measurements were made. The corresponding
wave numbers are also indicated.

Superimposed to this curve is the transmission response between a transducer and the probe when the latter is placed in the middle of the sample. We also show the response of the probe when the d.c. magnetic field is turned off, i.e., the electromagnetic energy fed through directly from the transducer to the probe. We observe from Figure 54 that at the lower end of the band, the insertion loss of the probe is 30 to 40 dB, an acceptable value for measurements. For higher wave numbers, however, the insertion loss increases considerably, oscillating around the feedthrough curve. Nevertheless, we were able to perform measurements in this range, as will be explained in the next subsection.

A simple calculation allows us to estimate the bandwidth of the probe. The loop itself is separated from the YIG surface by a layer of "Duco" cement ($\simeq$ 1 mil) and the thickness of the wire forming the loop (2 mils). The voltage induced in the loop is equal to the magnetic flux through the loop area. Assuming that the magnetostatic fields decay away from the YIG film as e^{-kx}, where k is the propagation constant, the most significant contribution to the voltage will come from the fields at the bottom of the loop where the exponential factor e^{-kx} is highest. For x = 3 mil, the value of k that makes the exponential become e^{-1} is k $\cong$ 130 cm^{-1}. As will be seen shortly, we performed CW pulse measurements at frequencies corresponding to wave numbers below this cutoff value. These are indicated with arrows in Figure 54. The reason for the use of CW pulses to measure the beam position was to avoid the effects of reflection from the edges of the sample. We must add that it was not possible to do the measurements in the swept-frequency mode since the angle of steering is a function of frequency.

5.2.1 Pulse Measurements

The experimental setup used to measure the beam steering with pulses is described schematically in Figure 55. The microwave switch, in conjunction with the microwave source, generates bursts of a single frequency. The switch also generates a synchronizing signal for the

106
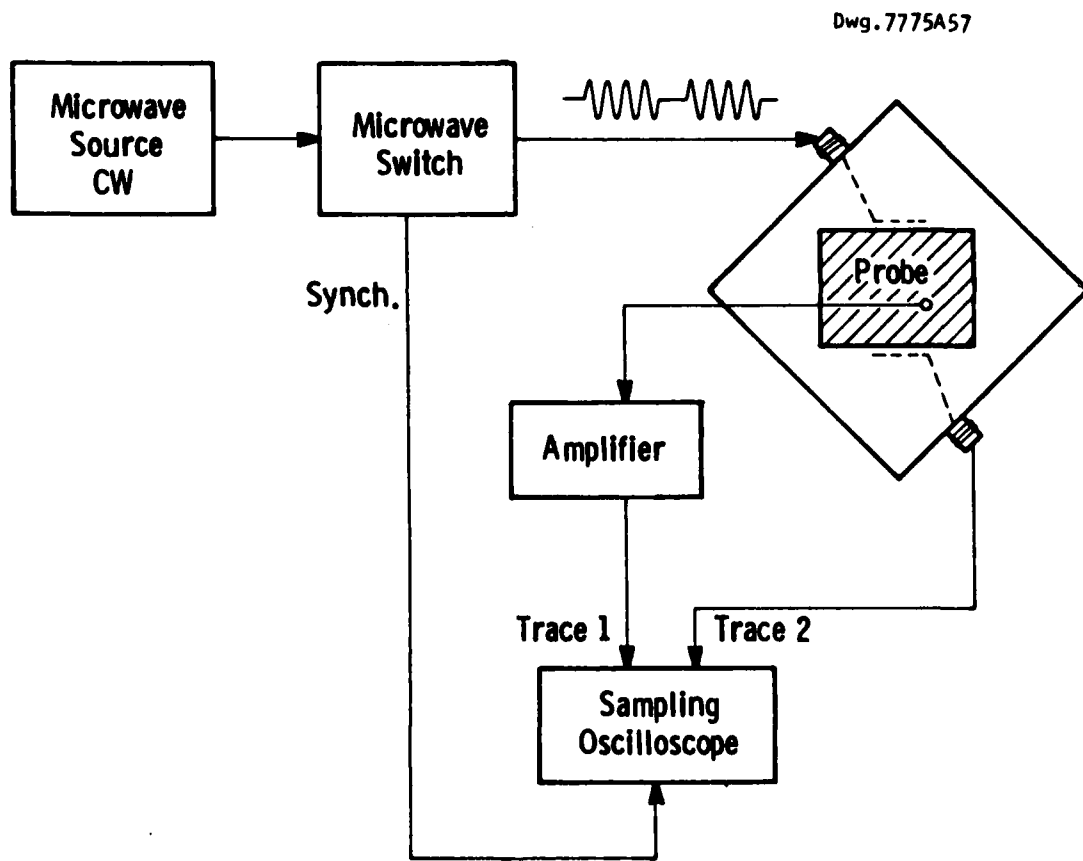
Figure 55. Block diagram of the experimental setup used for CW pulse measurements.

107

sampling oscilloscope. The signal from the probe was amplified and displayed on the screen of the sampling scope.

For pulses much narrower than the total delay between transducers, we were able to observe in a single trace the pulse at the input transducer, which fed through to the probe, and the pulse read by the probe, time delayed according to its distance from the input transducer. The second trace of the dual beam oscilloscope was used to display the pulse received by the output transducer, which marked the maximum delay that could be measured with the probe.

Measurements of the beam position were then performed by probing the fields along straight lines at fixed distances from the input transducer. Since the oscilloscope used has a storage capability, we were able to measure the relative amplitude of the pulses with an acceptable degree of accuracy.

5.2.2 Results

We present beam position measurements at three different frequencies 100 MHz apart, i.e., 2.7 GHz, 2.8 GHz, and 2.9 GHz. The applied magnetic field is 2.4 kG, and the film thickness is 50 μm. The YIG film was positioned so that MSFVW propagation is along the $(1\bar{1}0)$ axis (hard axis), which, according to other workers,[3,24] maximizes the beam-steering effect. Our results are shown in Figures 56 through 58.

Figures 56a, 57a, and 58a show the points where the maximum amplitudes are found at different distances from the input transducer. Distances are in mils. The transducer is 400 mils long (1 cm) and 2 mils wide (50 μm). The figures include a sketch of the transducer at the region of the diagram it occupies.

We see that at 2.9 GHz (Figure 56a), there is small ($\simeq 2.5^{\circ}$) steering of the beam from a direction perpendicular to the transducer. However, as we lower the frequency (Figures 57a and 58a), increased beam steering is observed. This behavior is in agreement with that previously reported in the literature by Smith et al.[24] At 2.8 GHz
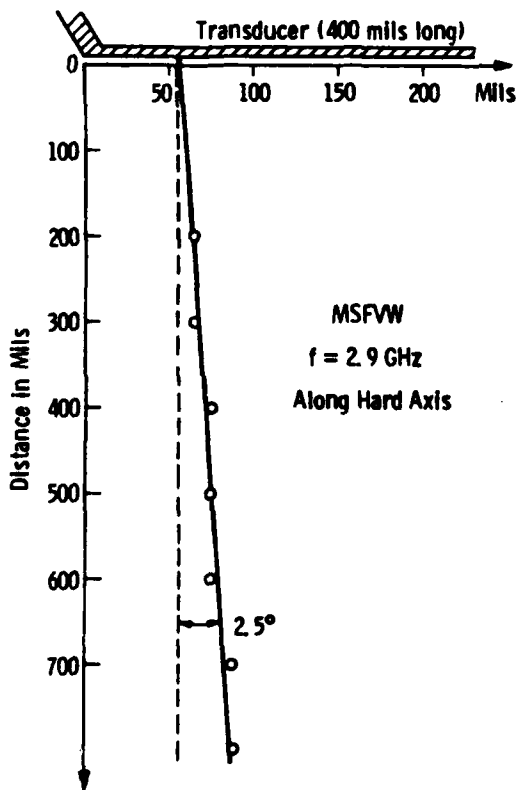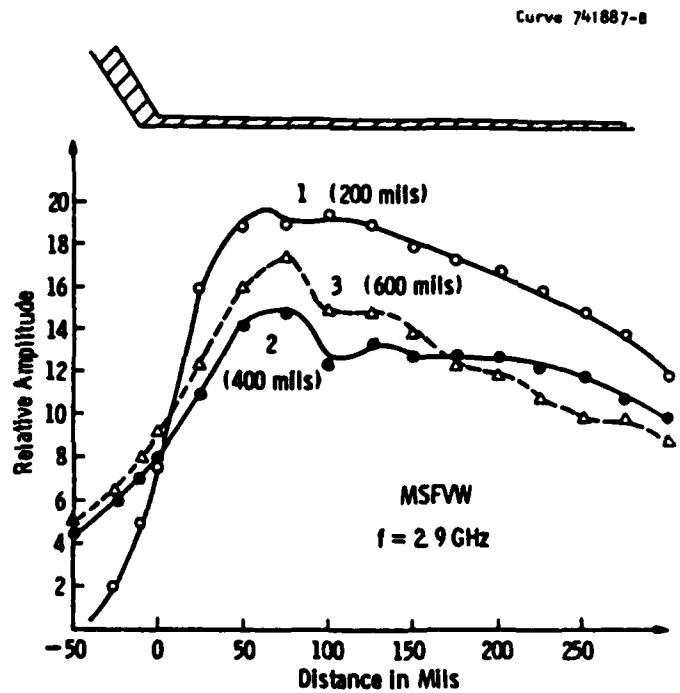
Figure 56. (a) Location of the field maxima at different distances away from the transducer. Frequency is 2.9 GHz. (b) Amplitude profile measured along straight lines parallel to the transducer and at different distances away from it. This distance is indicated in parentheses next to the curve number.

109
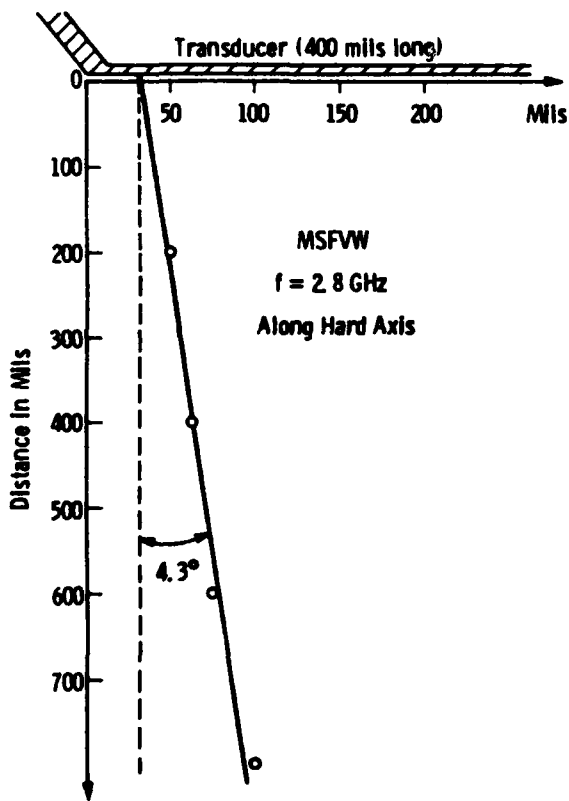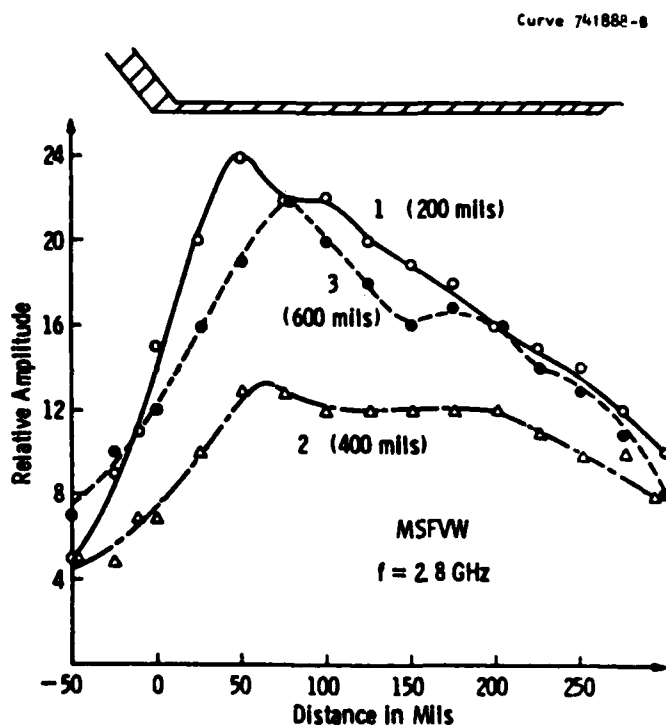
Figure 57. (a) Same as for Figure 56a. The frequency is 2.8 GHz.
(b) Same as for Figure 56b.

110
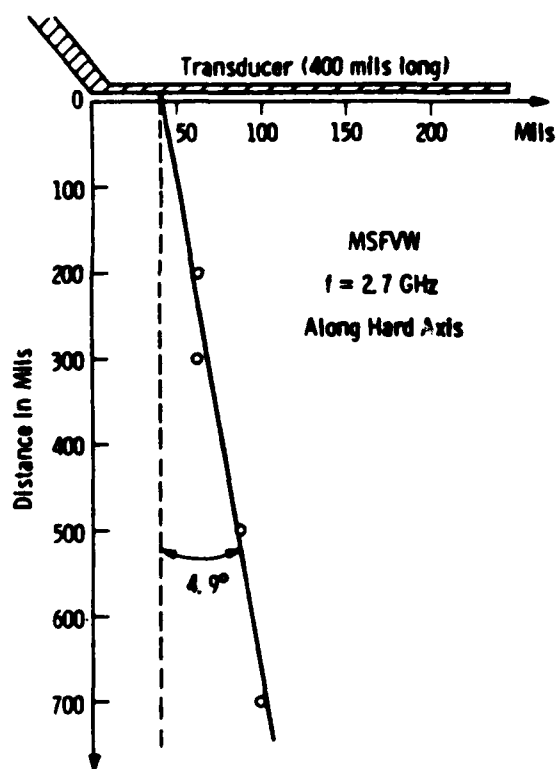
(a)
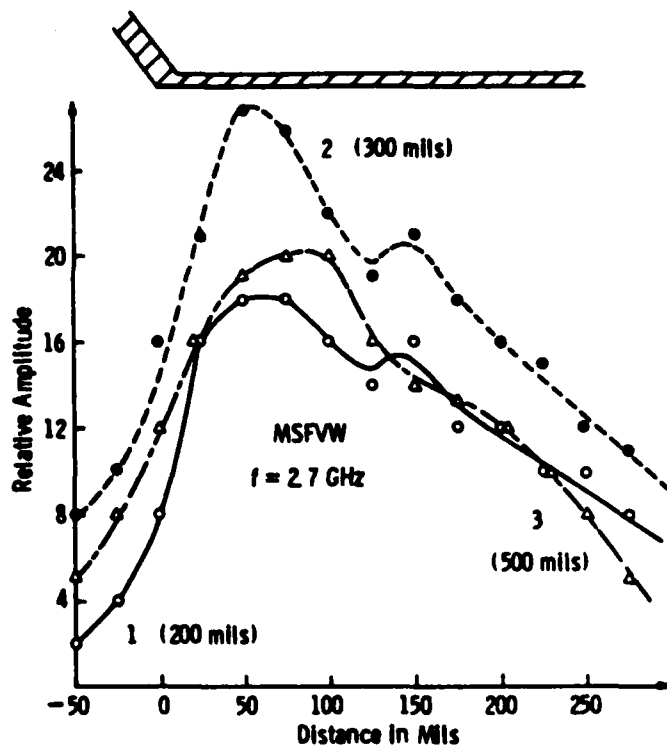
(b)

Figure 58.   (a) Same as for Figure 56a.   The frequency is 2.7 GHz.
             (b) Same as for 56b.

we measure a beam-steering angle of 4.3°, whereas at 2.7 GHz the angle is 5°.

Figures 56b, 57b, and 58b show amplitude profiles at different distances from the input transducer. Measurements were made at points 0.025 inch apart. The observation must be made that the transducers are approximately one-quarter wavelength long (1 cm) at these frequencies. That is, for zero coupling of electromagnetic energy into magnetostatic waves, the current distribution in the microstrip would be a quarter wavelength sinusoidal standing wave with a null at the open-circuit end and a maximum at the opposite end. As the coupling increases, the sinusoidal standing wave pattern is modified by an exponential decay of the current as it travels toward the open circuit and back.

In Figure 54, we see that the return loss diminishes as the frequency at which beam-steering measurements were made increases. These are marked with arrows in the figure.

Going back to Figures 56b to 58b, the amplitude profiles measured seem to confirm these theoretical considerations. Indeed, the rounder shape of curve 1 in Figure 56b resembles a sinusoidal standing wave which contrasts with the increasingly rapid decay observed in analogous curves of Figures 57b and 58b. However, superimposed to these modified quarter-wave sinusoidal curves, an oscillatory pattern of the points measured is observed, especially at distances from the transducer greater than 200 mils (see Figures 56b to 58b).

5.3 Other "Beam-Steering" Mechanisms

5.3.1 Diffraction

The obviously strong edge effect created at the beginning of the transducer, where the current is highest, led us to think of this as a two-dimensional diffraction problem, where the transducer acts as an analog to an optical aperture.

Figure 59 is a plot of the wave amplitude for light diffracted by a two-dimensional infinite aperture as a function of a normalized variable w dependent upon the distance x in the direction parallel to the aperture, the distance a, normal to the aperture, and the light wavelength. The dashed line corresponds to the ideal case of light of zero wavelength.[27]

The significance of Figure 59 is clarified in Figure 60, where a plot is presented showing the displacement of the maximum in Figure 59 as a function of the distance to the aperture (transducer). In other words, it is a plot of x versus a from the expression

$$w = \frac{x}{\sqrt{\lambda a/2}}$$

(see Figure 59) for the case of w = 1. The assumption was made that the maximum occurs at approximately w = 1. In Figure 60, we have used as parameters the MSFVW wavelengths corresponding to the three frequencies at which measurements were made (see Figure 54). Notice also that the range of values for the distance a to the aperture is the same as that in our measurements.

From the curves of Figure 60, the displacement of the maximum can be approximately described by a straight line making a certain angle with the normal to the aperture (transducer). This is shown in the figure. These deflection angles have comparable values to those of our beam-steering measurements (see Figures 56a to 58a).

The foregoing considerations suggest that the results shown in Figures 56 to 58 may indeed be due to a diffraction phenomenon. The magnetostatic forward-volume fields have a basic quarter-wave sinusoidal distribution in a direction parallel to the transducer. But this distribution seems to be modified by a function such as that of Figure 59, thus resulting in the oscillatory pattern described before. Moreover, the calculated deflection of the field maximum due to diffraction agrees well with our measurements.

113
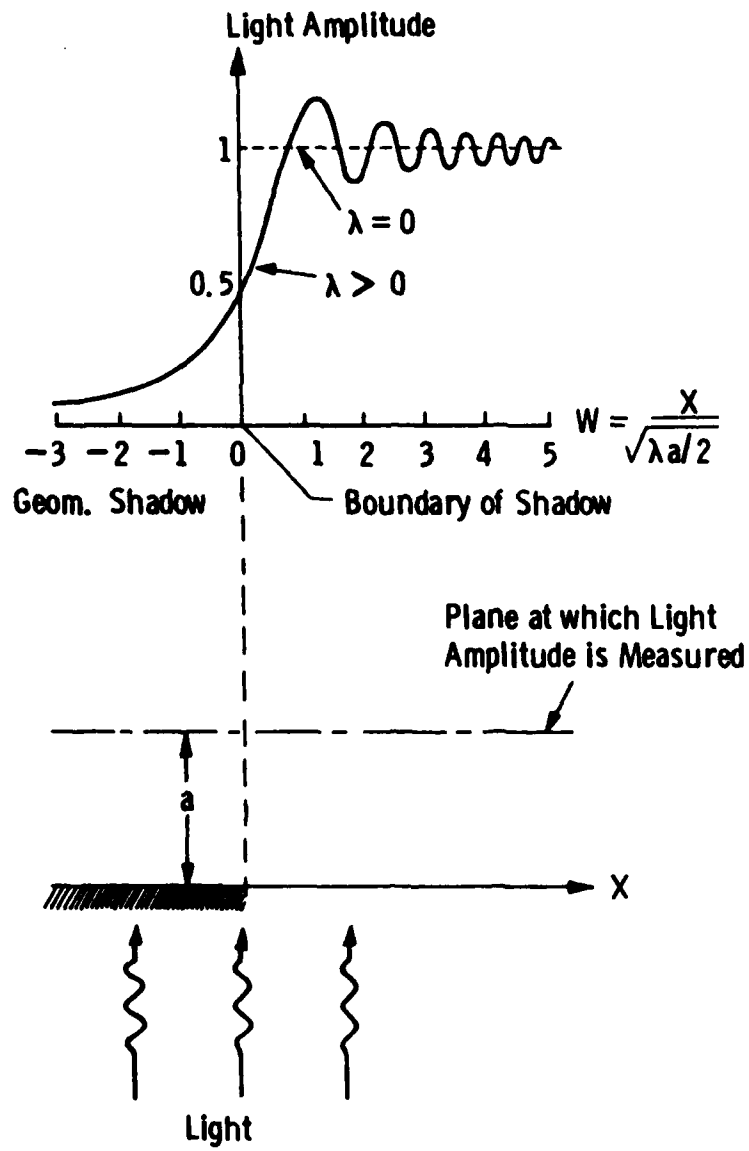
Figure 59. Light amplitude profile measured at distance "a" from an infinite two-dimensional aperture.

114
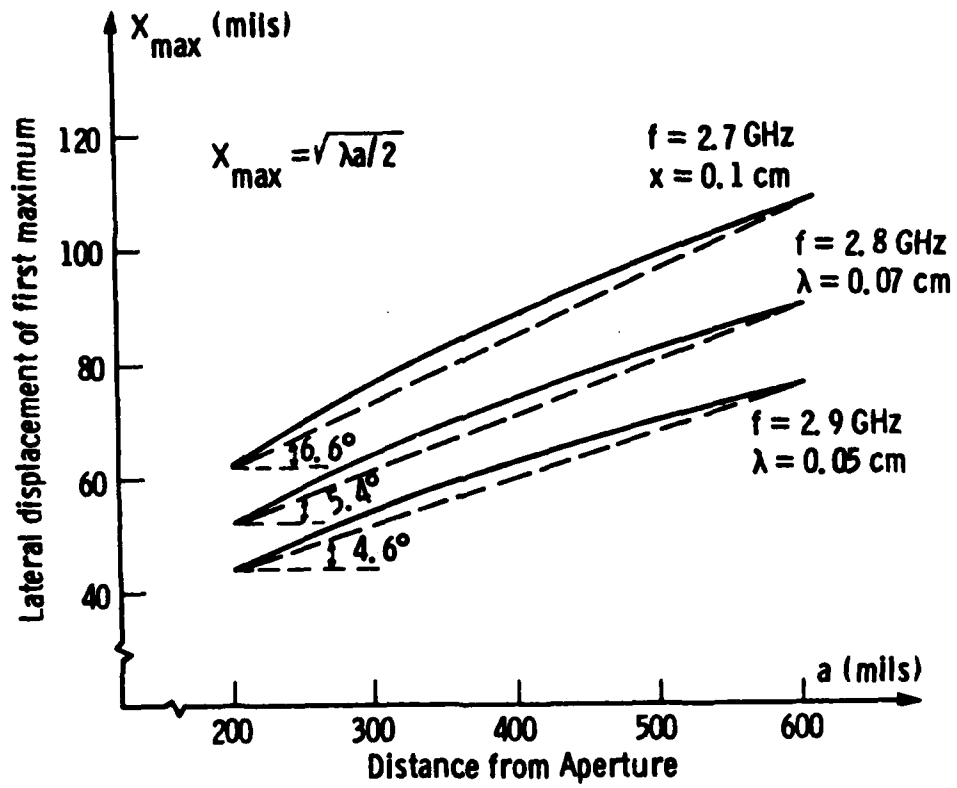
Figure 60. Displacement of the maximum in Figure 59 as a function of the distance "a" to the aperture.

115

We have not been able to account, however, for an observed nonuniformity in the amplitudes of the different curves relative to each other. For example, in Figure 56b, the amplitudes of curve 2 are lower than those of curve 3, even though 2 is measured closer to the transducer than 3. The possibility of having taken measurements only at the vicinity of the minima of Figure 59 is ruled out since the distance between two consecutive extrema is about 0.040 inch and measurements were made at points 0.025 inch apart.

5.3.2 Transducer Phase Shift

The finite phase shift along an MSW transducer may be expected to produce beam steering in a manner similar to a phased array antenna. If it is assumed that there are no reflections from the end of the transducer, i.e., it is electrically long, then the angle between the transducer normal and the MSW beam direction is $\theta = \sin^{-1} \beta/k$, where β is the wave number of the electromagnetic wave in the microstrip transducer and k is the MSW wave number.

Figure 61 shows a calculated plot of beam angle as a function of frequency. The film thickness was assumed to be 50 µm and the alumina substrate thickness was 250 µm. The transducers were 50 µm wide by 1 cm long and were terminated by an open circuit at one end. The internal field and saturation magnetization were 800 Oe and 1800 G, respectively. Note that $\theta \rightarrow 90^{\circ}$ when $\beta = k$. β was approximately 1.5 cm^{-1} over the frequency range considered. Although very large beam angles can be obtained close to $k = 0$, the experimental observations cannot be explained in terms of this phenomenon. However, since beam steering due to this mechanism is proportional to frequency, through β, its effect will be more significant in X-band.

116

Curve 741866-A
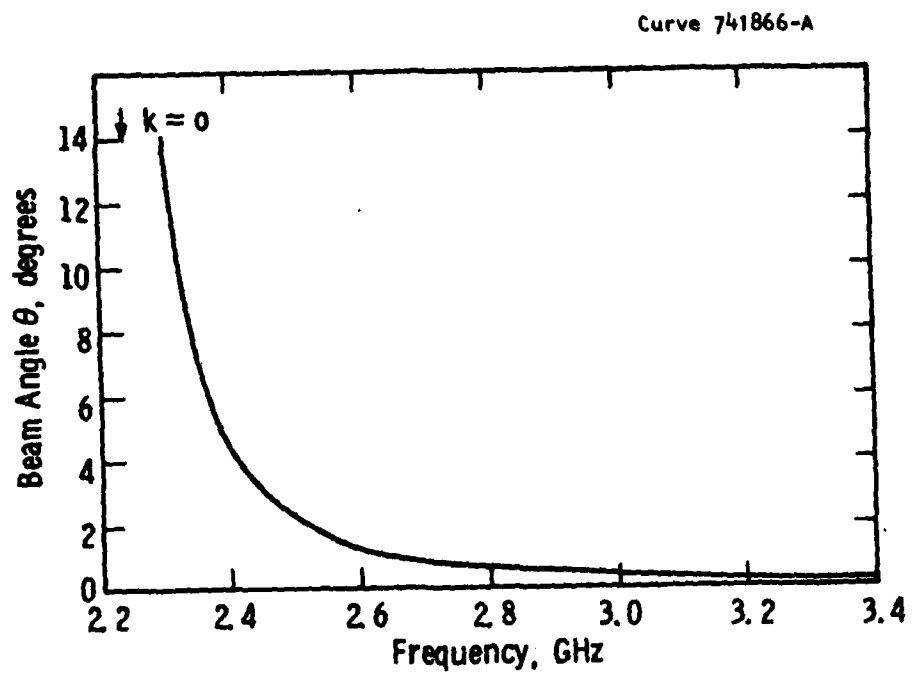
Figure 61. Beam steering of FVW due to phase shift along transducer
length. Internal field 800G.

117

6. MAGNETOSTATIC WAVES IN DOUBLE LAYERS

The equations of propagation for magnetostatic waves in separated double layers of ferrite have been derived by the authors[28] in a paper where they are applied to the particular cases of forward- and backward-volume waves (see Appendix II).

Here, we state our results in general form; for two films, (1) and (2), backed by ground planes, the dispersion relation can be given in the form of a product of forward and backward dispersion relations for each film separately (together with the associated ground plane), linked by coupling through the thickness t of the space between them. For wave number k, we find

$$D_1(+)D_2(+) = D_1(-)D_2(-)e^{-2kt}, \qquad [54]$$

where $D_i(\pm)$ is the secular equation for film i, for waves with positive or negative wave numbers.

In particular, when t is very large and k is positive, it is evident that the roots of Equation 54 are the solutions of $D_1(+) = 0$ or of $D_2(+) = 0$; i.e., they are solutions for unlinked films, as expected. Equally, when t is very large and k is negative, the roots of Equation 54 are the solutions of $D_1(-) = 0$ or of $D_2(-) = 0$.

Note that D_1 and D_2 include the associated ground plane but not the other ground plane, so that the roots of $D_i = 0$ involve only one ground plane, as must be the case when the films are far separated.

For a wave travelling along the x direction on a film characterized by permeability (μ), with a ground plane at a distance s_i, define

$$\beta = (\mu_{11}/\mu_{22})^{1/2}, \qquad [55]$$

118

$$T_{di} = \frac{1}{\beta} \tanh \beta k d_i,$$

$$T_{si} = \tanh k s_i, \qquad [56a]$$

where d_i is the thickness of the film. It will be noted that when μ_{11}/μ_{22} is negative, as is the case for volume waves, T_{di} remains real; i.e., if

$$\mu_{11}/\mu_{22} = -\alpha^2, \text{ then } T_{di} = \frac{1}{\alpha} \tan \alpha k d_i. \qquad [56b]$$

Equations for the dispersion relations are, for the upper film, with ground plane a distance s_1 above it,

$$D_1(\pm) = (T_{s1} \pm 1)\mu_{22} + [\mu_{11}\mu_{22} - \mu_{12}^2 - \mu_{12}(T_{s1} \mp 1) \pm T_{s1}]T_{d1}, \qquad [57a]$$

and for the lower film, with ground plane a distance s_2, below it,

$$D_2(\pm) = (T_{s2} \pm 1)\mu_{22} + [\mu_{11}\mu_{22} - \mu_{12}^2 + \mu_{12}(T_{s2} \mp 1) \pm T_{s2}]T_{d2}. \qquad [57b]$$

The relative permeabilities μ_{ij} need not be the same in the two films.

6.1 Volume Waves

Volume waves are characterized by $\mu_{11}/\mu_{22} < 0$ and $\mu_{12} = 0$. The first condition implies that each film carries by itself an infinite set of modes (exchange effects being ignored). In the absence of ground planes, the secular equation for a single film is

$$\tan \alpha k d = \frac{2\alpha \mu_{22}}{\alpha^2 \mu_{22}^2 - 1} \qquad [58a]$$

If the fundamental mode has wave number k_o, then other modes with $kd = k_o d + n\pi/\alpha$ are also solutions, n being an integer.

For a double film, therefore, we expect a doubly infinite set of modes; when two equal films are brought together ($t = 0$), we expect (and find) modes for a single film of thickness $2d$.

119

The system is greatly simplified by the fact that $\mu_{12} = 0$. For equal films ($M_1 = M_2$, $d_1 = d_2$, $s_1 = s_2$), we have $D_1(\pm) = D_2(\pm)$, and Equation 54 simplifies to

$$D(+) = \pm D(-)e^{-kt}. \qquad [58b]$$

(The $\pm$ sign here corresponds to the square root of Equation 54, not to the direction of k.) The secular equation becomes, for equal thicknesses d,

$$\tan \alpha kd = \frac{\mu_{22}\alpha(\tanh ks + c)}{\mu_{22}^2\alpha^2 - c^2\tanh ks} \qquad [59a]$$

in which

$$c = \tanh (kt/2) \text{ for modes even in } h_x,$$
$$= \coth (kt/2) \text{ for modes odd in } h_x.$$

Here, h_x is the rf magnetic field, and the modes are odd or even about the center of the system. When t is very small, the modes are merely the alternating odd and even modes of a single film.

The fundamental mode can be either the first even mode or the first odd mode. For forward-volume waves, h_x and m_x are the principal force and excitation of the system, so the fundamental is the first mode even in h_x. For backward-volume waves, h_y and m_y are the principal force and excitation, and their symmetry is opposite to that of h_x; the fundamental is therefore the first mode odd in h_x.

6.2 Surface Waves

Surface waves differ strongly from volume waves in two respects:

1. A single film supports only a single mode. No true system of linked symmetric and asymmetric modes can therefore exist; when the spacing t is made indefinitely small, any second mode must vanish from the system.

ii. The secular equation, Equation 45, can no longer be factorized because $\mu_{12} \neq 0$; from Equations 57a and b, we see that it is now no longer the case that $D_1(\pm) = D_2(\pm)$ for equal films. This fact reflects the absence of any second solution when $t = 0$.

Most results must be obtained by computation, but some simple results can be obtained analytically.

When kt is large, we obtain "odd" and "even" modes with wave numbers separated from the single film wave numbers by a small amount δk, where $\delta k \sim \pm\ e^{-kt}$.

When the separation t is small, there are two modes with very different characteristics. For frequencies near the band edge, f_{min}, the fundamental mode is of the type

$$k(d_1 + d_2) \sim \quad f-f_{min}. \qquad [60a]$$

This mode is essentially a surface magnetostatic wave for the two films together.

The second mode, near f_{min}, has the characteristic

$$k^2 \sim (f-f_{min})/t. \qquad [60b]$$

Thus, when t is very small, k becomes very large except at the lowest frequencies, and no second mode exists when t vanishes.

6.2.1 Coupling to a Current

Here, we outline the nature of the coupling constants used to describe the radiation of magnetostatic waves by a current; algebraic results are given in Appendices II and III.

The radiation of surface waves has been calculated for a central conductor between the two films, and for a single transducer outside the two films. The power radiated into the waves is conventionally expressed in terms of a radiation resistance R per unit length of

121

transducer. For current J, the powers radiated in the forward and backward directions are

$$p^{\pm} = R^{\pm}J^2 \qquad [61]$$

where

$$R^{\pm} = \mu_o \omega K^{\pm} \qquad [62]$$

Here, K^+ and K^- are dimensionless coupling constants which, in strong coupling cases, are of order unity. All discussion of coupling will be cast in terms of such constants.

For external excitation of surface waves, it is found that $K^+ \gg K^-$, as is usual, when the "even" mode is excited. The "odd" mode, which cannot be supported by a single film, is more weakly excited, and the disparity between K^+ and K^- is less.

For central excitation of surface waves, $K^+ = K^-$, from arguments of symmetry, and we shall show later that the "odd" mode is the more strongly generated.

The symmetry of volume modes in equal films gives rise to the possibility of selective excitation of odd or even modes. We have therefore considered currents J_1 and J_2 flowing in two symmetrically placed transducers. It is found that the radiated energy has the form

$$p^{\pm} = 1/2 \; \mu_o \omega \; [(J_1+J_2)^2 K_e + (J_1-J_2)^2 K_o]. \qquad [63]$$

Here, K_e and K_o are coupling constants for even and odd modes, respectively. The powers in forward and backward directions are equal, and for widely separated films $K_e = K_o$. The factor 1/2 is inserted in Equation 63 so that the power generated by a single current near one of two distant films will be $\mu_o \omega J^2 K$, in agreement with Equation 62.

It is clear from Equation 63 that only even modes are excited if $J_1 = J_2$, and only odd modes if $J_1 = -J_2$. In practice, selective excitation is not always easy, or even possible, when the desired mode

122

has the lower coupling strength, because the transducers cannot be made perfectly symmetrical.

6.2.2 Computed Results for Surface Waves

In all the results that follow, the terms symmetric and antisymmetric will be used to denote the first or fundamental solution and the second solution, respectively, for surface waves. This is to maintain a consistent terminology for all the double-film results. Additionally, the surface wave rf field components of magnetization, $m_x(y)$, do at least show a quasisymmetry or antisymmetry for their respective modes and, therefore, the terms do have some geometric validity. Figure 62 shows the dispersion results for two 20 μm films spaced 5 μm apart. Because the films are closely spaced, the two solutions are well separated, and the trend of the antisymmetric mode to approach the horizontal axis as the films get closer and closer together is evident in Figure 62. Figures 63a and 63b show some representative rf field amplitudes for the two modes. Two 20 μm films spaced 40 μm apart were chosen. The coordinate system chosen had SW propagation along x, y normal to the films, and the bias field H along z. The rf magnetization $m_x(y)$ and magnetic field $h_x(y)$ values were derived from a magnetostatic potential function normalized to 1 on the YIG film face at the -40 μm location of Figures 63a and 63b. The approximate symmetry of $m_x(y)$ in Figure 63a and approximate antisymmetry of $m_x(y)$ in Figure 63b is evident. Figures 64a and 64b show representative curves of delay versus frequency for two 20 μm films at spacings ranging from 5 to 80 μm. As with the FVW and BVW double films, the SW antisymmetric mode shows a region of quasi constant delay over bandwidth of up to 400 MHz at S-band. Successive curves also show some reasonable degree of parallelism suggesting a constant-but-adjustable delay could be achieved by controlling the film separation in some manner. This has been tried for various waves in the experimental results reported on later (see Section 6.3). The surface wave symmetric mode was disappointing compared to the corresponding volume wave results in that no substantial

123
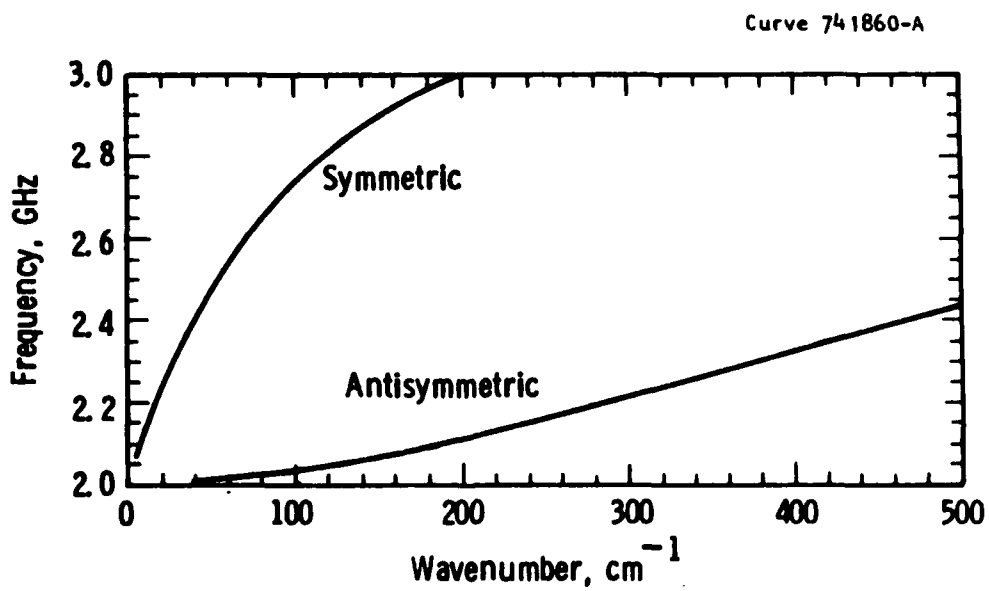
Figure 62. Dispersion relations for the SW symmetric and antisymmetric modes propagating in two 20 µm YIG films spaced 5 µm apart; H = 250G, ground plane spacings 1 cm.
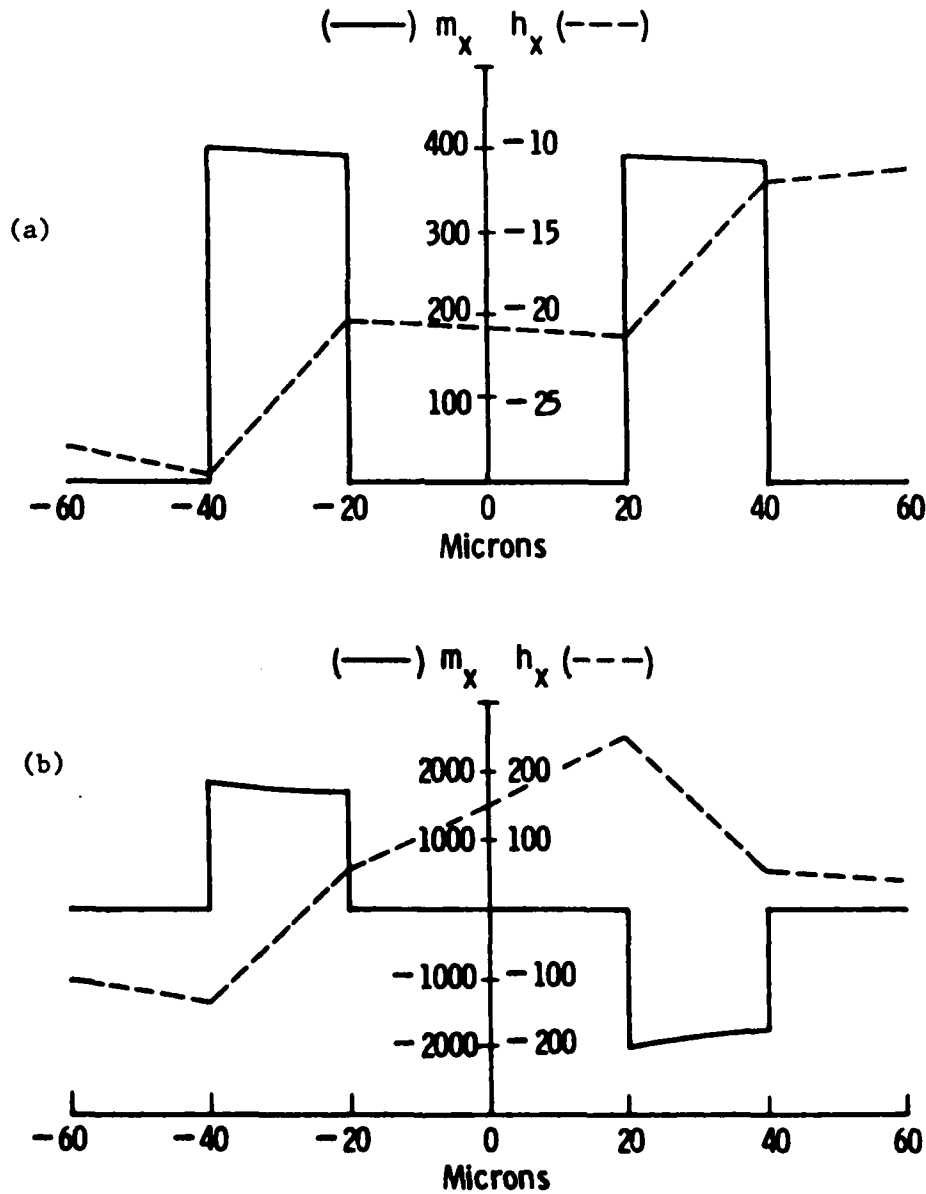
Figure 63. (a) The y-variation of the x-component of rf magnetization $(m_x(y))$ and rf field $(h_x(y))$ for a symmetric SW in two YIG films 20 μm thick spaced 40 μm apart; $f = 2.3$ GHz, $k = 29.59$ cm^{-1}, $H = 250G$, ground plane spacings $\rightarrow \pm \infty$. (b) As in Figure 63a except for an antisymmetric SW with $k = 135.25$ cm^{-1}; all other parameters the same.

125
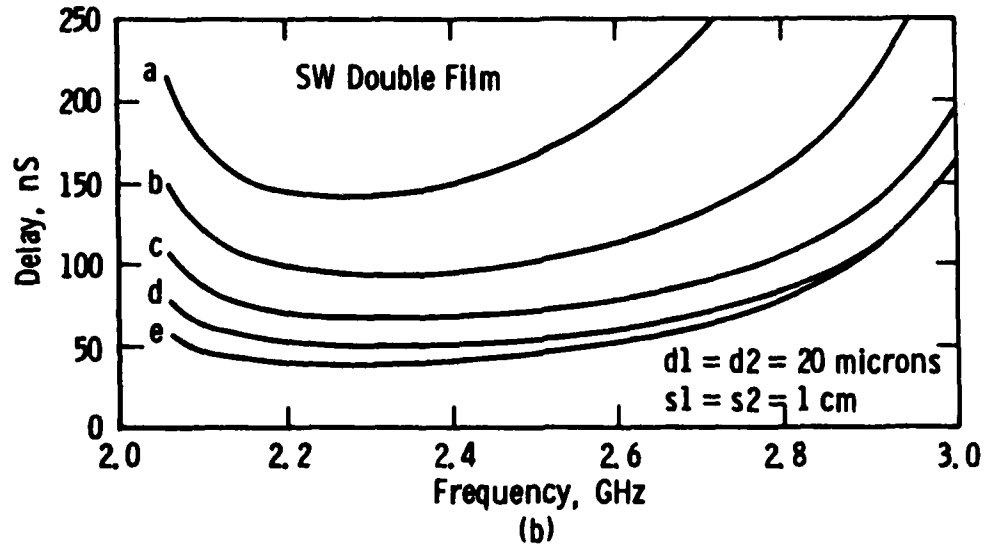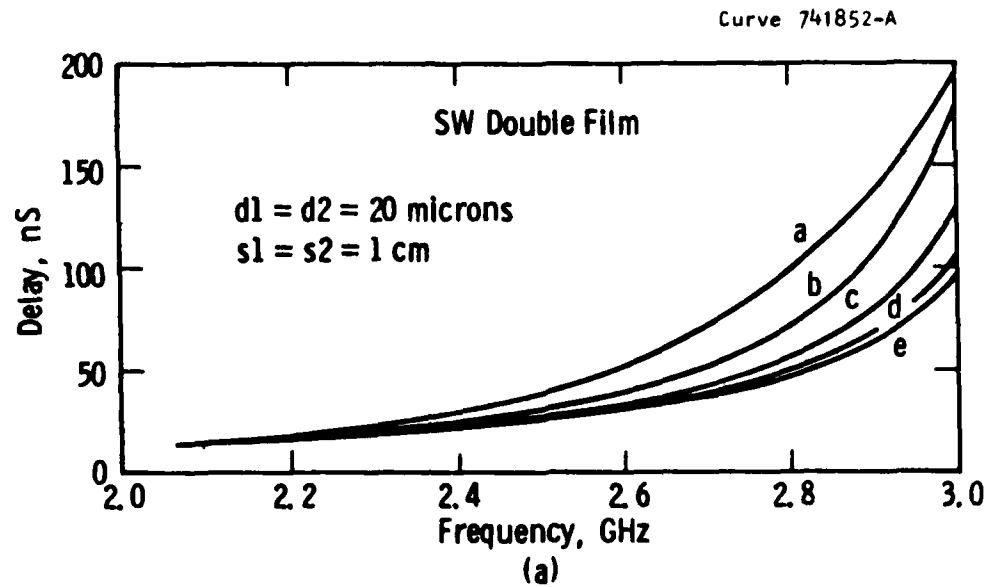
Figure 64. (a) Computed delay versus frequency for a symmetric SW in two 20 μm thick YIG films; H = 250G, ground plane spacings 1 cm, film spacings (a) through (e) are, respectively, 5, 10, 20, 40, and 80 μm. (b) As in Figure 63a except for antisymmetric SWs; all other parameters the same.

126

region of linear delay was found. If the curves of Figure 64a are expanded in the frequency range 2 to 2.6 GHz, significant curvature is still evident. Ground plane influence was made negligible for these results. Thus, SWs in double films are qualitatively similar to those of volume waves in terms of the delay characteristics, but there does not appear to be any desirable linearly dispersive behavior without ground plane influence. However, possible effects of interest due to ground planes or from two films of different magnetization have not been explored.

Figures 65 and 66a and b show the results of coupling constant calculations for internal and external transducers (see Figure 7a and 7c, respectively, of Appendix II). In the experiments to be described, it would thus be expected that a single transducer sandwiched between films should excite the antisymmetric mode (K_{int}). In contrast, a transducer external to the film would excite the symmetric mode. Coupling to $-k$ surface waves should be weak (Figure 66b).

6.3 Experimental Results

The measurements described in this section were made on two types of double film. The first, which can be described as measurements on synthesized double films, was done with two rectangular bars 25 mm x 5 mm of single films. These single films sandwiched transducers which were made of Au wire; thus, the wire diameter determined the film separation and was from 1/2 mil (12 μm) up to 2 mils (50 μm). Amplitude (S_{21}) and delay (D) results were taken on an automatic network analyzer (HP model 8409C). The computation of S_{21} and D versus frequency was derived from data using an eight-term error model but with an improved phase calibration accuracy of $\pm 0.5^{\circ}$. The static bias field (H) was provided by a 12 inch Varian electromagnet or occasionally by purchased Sm-Co permanent magnets. The second type of measurement was made on epitaxially grown double films in which the film separation was by a grown layer of GGG (see Section 6.4). In these films, coupling could be made to the outer surface of the top film only.

127
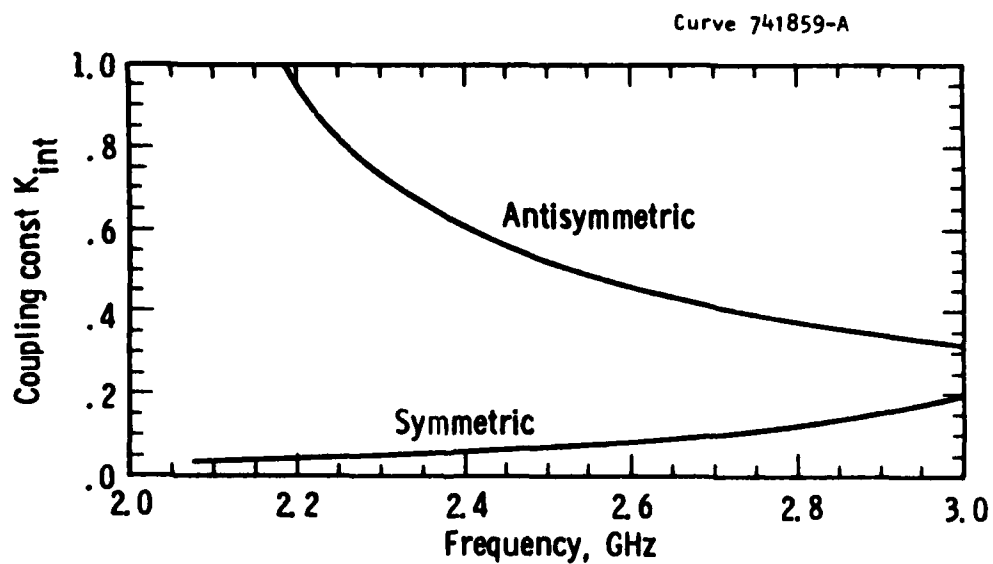
Figure 65. Internal coupling constant for SWs versus frequency for a
single mid-plane line-element transducer located midway
between two 48.3 μm thick YIG films spaced 52 μm apart;
H = 250G, ground plane spacings → ± ∞.

Curve 741849-A
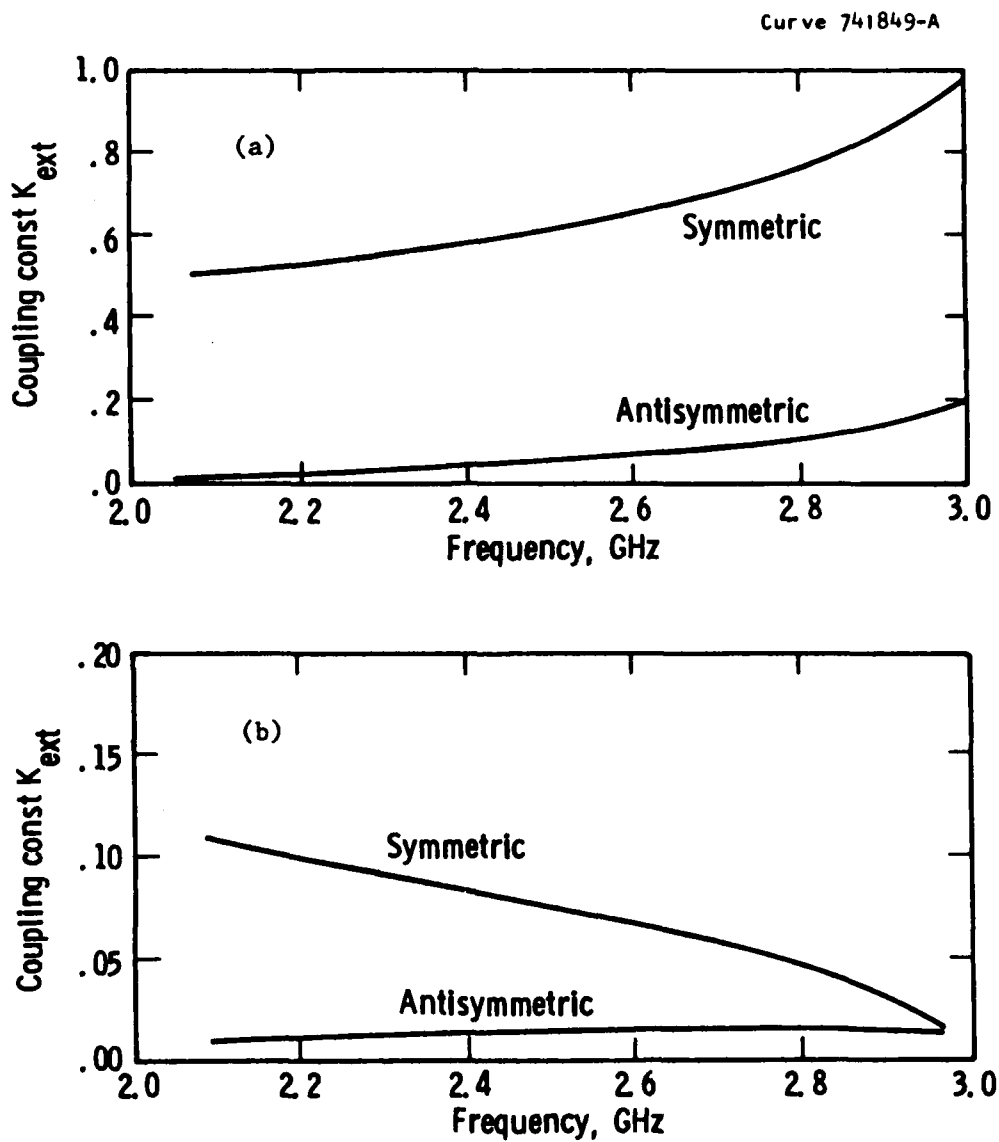
Figure 66. (a) External coupling constant for SWs versus frequency for
a single line-element transducer located on the top surface
of two 48.3 μm YIG films spaced 52 μm apart; H = 250G,
ground plane spacings → ± ∞. (b) As in Figure 66a except
for -k surface waves.

129

6.3.1 Surface Waves

Figure 67 shows the results of SWs propagating in two 20 μm films separated by a 40 μm GGG layer. The transducers are necessarily external to the films, therefore, and the measurements are clearly consistent with the excitation of a symmetric mode. This is in qualitative agreement with the computed coupling strength of Figure 66a. Figure 68 shows results using two separate 48.3 μm films sandwiching 2 mil diameter Au wires. Figure 65 shows that this geometry should excite the antisymmetric mode, and the experimental data of Figure 68 are generally in agreement with this. However, the data are subject to fairly large delay measurement error. In fact, the raw data showed evidence of an interference-like ripple to it, suggestive of at least some contribution from the symmetric mode. The predominant mode, though, was the antisymmetric one.

6.3.2 Volume Waves

Some early results on volume waves have already been published (see Appendix II). We report here on recent ones mostly taken on the compositely grown double films. Figure 69 shows results for FVWs in films of YIG, respectively measuring 20.5 μm and 19.8 μm separated by 18.6 μm of GGG. Agreement with the delay values calculated for the symmetric mode is good. Figure 70 shows the same films with BVW excitation, and here the agreement with calculation for the symmetric mode is very good. The delay "spikes" seen near the top of the band could be correlated with "spikes" in the amplitude response (S_{21}). However, at this time their origin has not been identified; possible sources are width mode effects or walk-off effects due to a ground plane (see Section 2.6). Figures 71 and 72 show a similar set of results for two 20.2 μm thick films separated by 11.4 μm of GGG. In both cases, coupling to the symmetric mode is unequivocal with good agreement between calculated and measured delay values. Overall, the FVW results show the most delay noise, but the BVW results have prominent "spikes"

Curve 741858-A
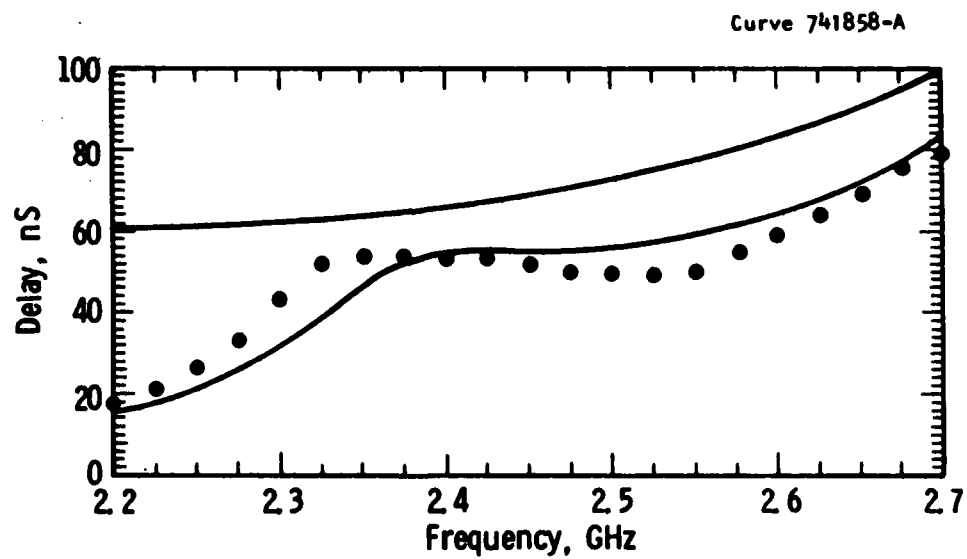
Figure 67.   Calculated and measured (.) delay values versus frequency
for +k SWs propagating in two 20 μm thick YIG films spaced
40 μm apart; H = 230G, transducer separation 1.27 cm, ground
plane spacings, respectively, 250 μm and 0.5 cm.

131
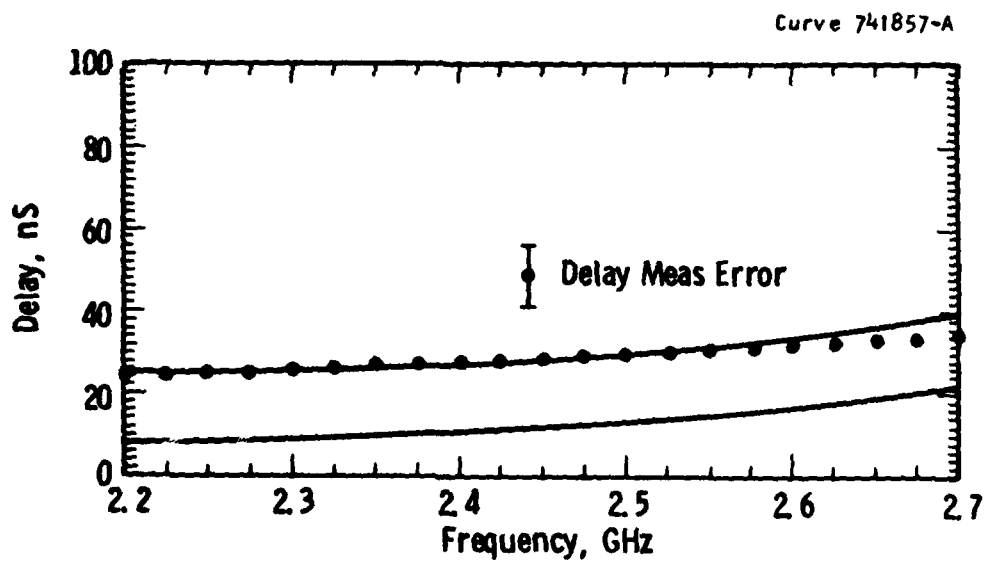
Figure 68. Calculated and measured (.) delay values versus frequency
for +k SWs propagating in two 48.3 μm thick YIG films
separated by 2 mil (52 μm) diameter Au wires; H = 230G,
transducer separation 1 cm, ground plane spacings,
respectively, 550 μm and 0.5 cm.

132
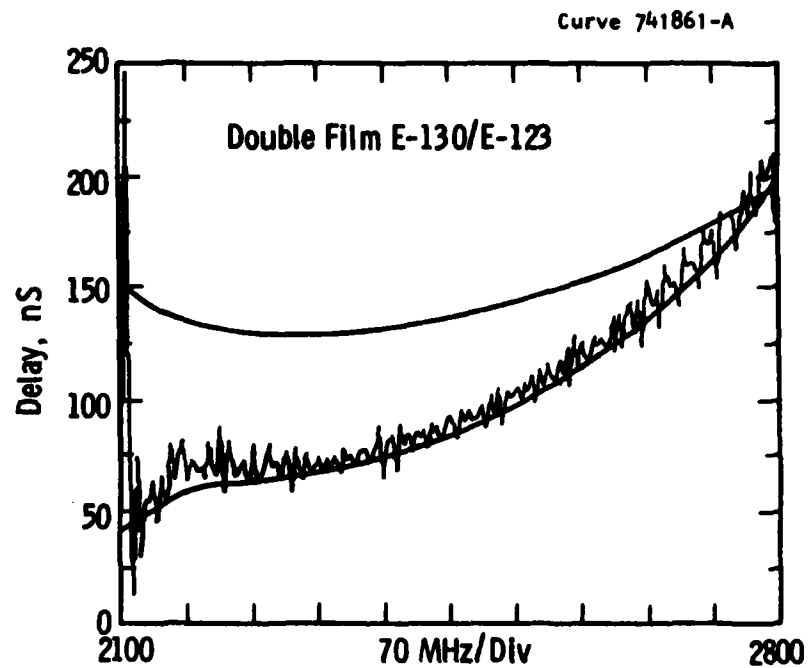
Figure 69. Group delay versus frequency for forward-volume waves in a YIG double film, respectively, measuring 20.5 μm and 19.8 μm separated by 18.6 μm of GGG. Smooth curves are calculated results for the symmetric mode (lower curve) and the antisymmetric mode (upper curve). Jagged curve is measured result.

133

Curve 741869-A
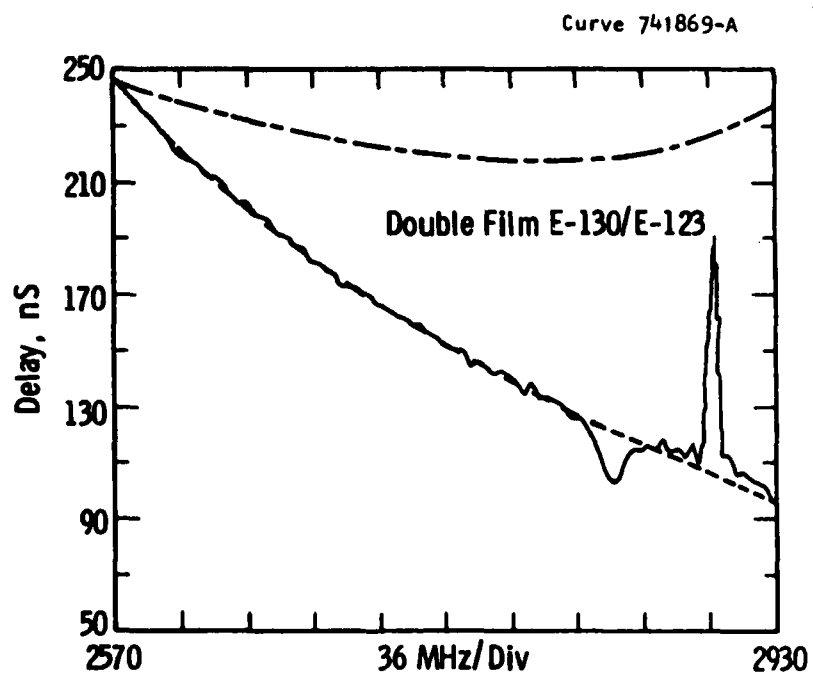
Figure 70. The same as Figure 69 except results are for backward-volume
waves. Broken curves were calculated.

134
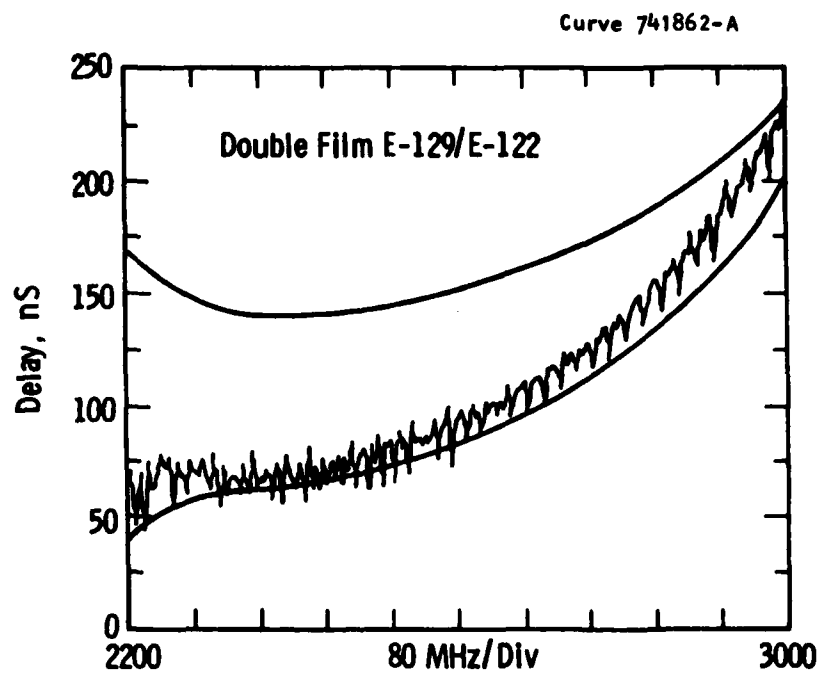
Figure 71. Group delay versus frequency for forward-volume waves in a YIG double film, respectively, measuring 20.2 µm each and separated by 11.4 µm of GGG. Smooth curves are calculated results for the symmetric mode (lower curve) and the antisymmetric mode (upper curve). Jagged curve is the measured result.
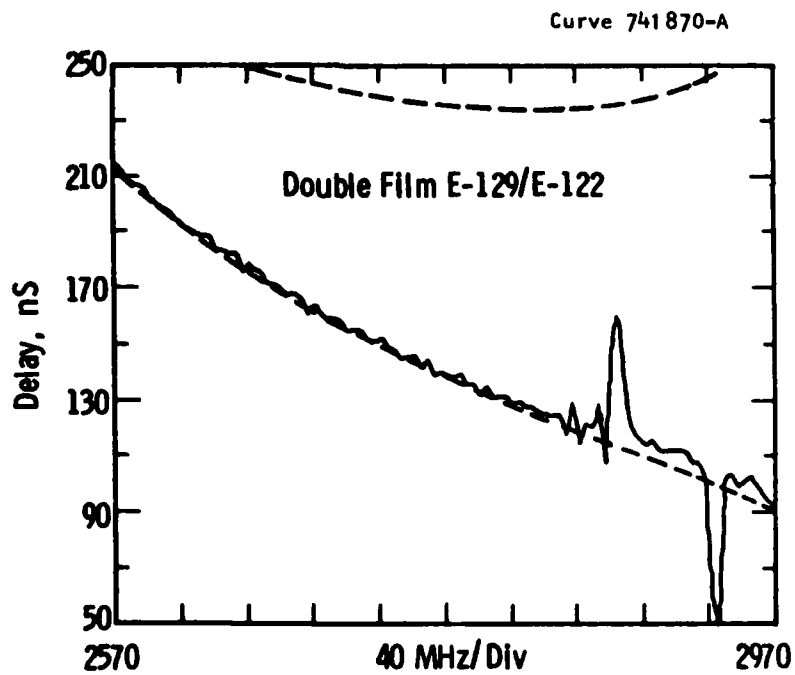
Figure 72. The same as Figure 71 except results are for backward-volume waves. Broken curves were calculated.

evident near the band edge. It should be noted that the calculated results contain an assumed parameter in the form of $4\pi M = 1.800$ kG. Plans are in hand to measure this parameter in future programs. Additionally, the internal bias field (H) is always inferred from the frequency location of the band edge in the S_{21} data, i.e., γH for FVWs and $\gamma\sqrt{H(H+4\pi M)}$ for BVWs. Lack of precise knowledge of the anisotropy fields dictated this approach.

6.3.3 Adjustable Delay

Results of potential device value were taken on 48.3 μm YIG films sandwiching Au wire transducers. These excite the antisymmetric mode of FVWs, and calculations had shown this mode to have a region of quasiconstant delay which could further be made adjustable by varying the spacing between the films. Thus, Figure 73 shows results respectively employing 1/2 mil and 2 mil diameter wire transducers. Agreement with calculation is good, but the degree of parallelism of the results over this large range of spacings was not adequate for consideration as a practical variable delay device. However, if the spacing range is restricted, more useful characteristics can be obtained. Figure 74 shows calculated results with the film spacing at 20 and 30 μm, respectively. This choice of parameters is better but requires some mechanical ingenuity to implement the controlled close separation of the YIG films. The surface wave calculated results shown in Figure 64b suggest that this too may be a suitable geometry for variable delay.

6.3.4 Linearly Dispersive Delay

Calculations performed previously (see Appendix II) had shown that the FVW symmetric mode in a double film could display an optimum degree of delay linearity over approximately 1 GHz of bandwidth if the film thickness-to-spacing ratio was 1:2. With this in mind, sample E-146/E-138 was grown having 20 μm thick YIG films separated by 40 μm of GGG. Figure 75 shows the delay measurements and calculation for this

Curve 741864-A
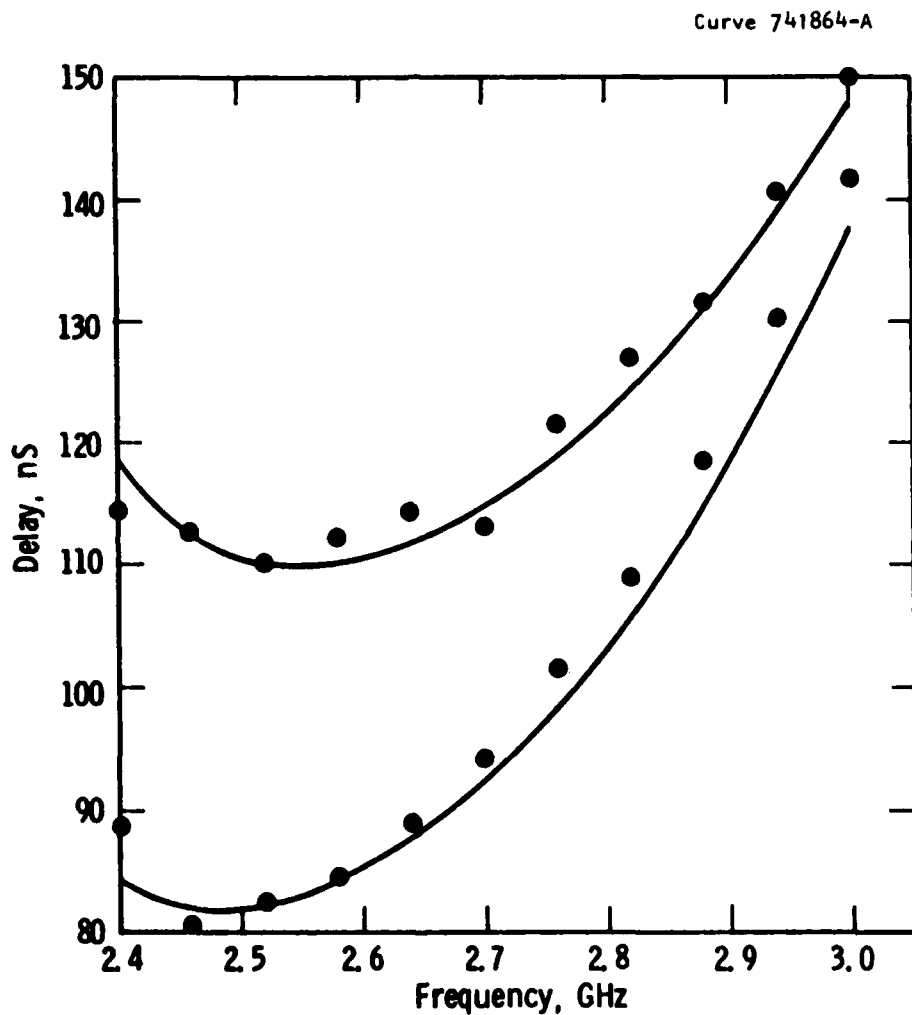
Figure 73. Calculated and measured (.) group delay values versus
frequency for antisymmetric FVWs propagating in two 48.3 μm
thick YIG films separated, respectively, by 12 μm (upper
curve) and 50 μm (lower curve); H_o = 2510G, transducer
separation 1 cm, ground plane spacings, respectively, 550 μm
and 0.5 cm.

138
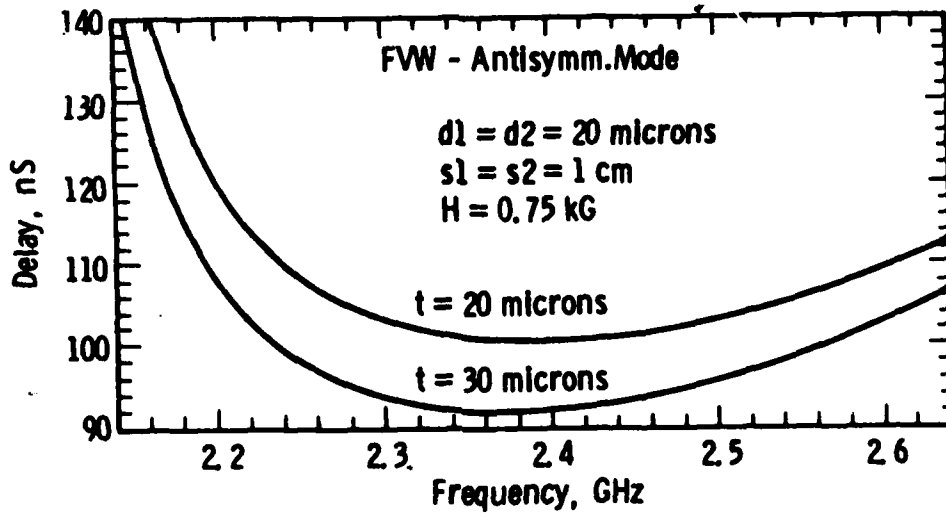
Figure 74. Calculated delay versus frequency for antisymmetric FVWs propagating in two 20 μm thick YIG films spaced, respectively, 20 and 30 μm apart; H = 750G, ground plane spacings 1 cm.

139
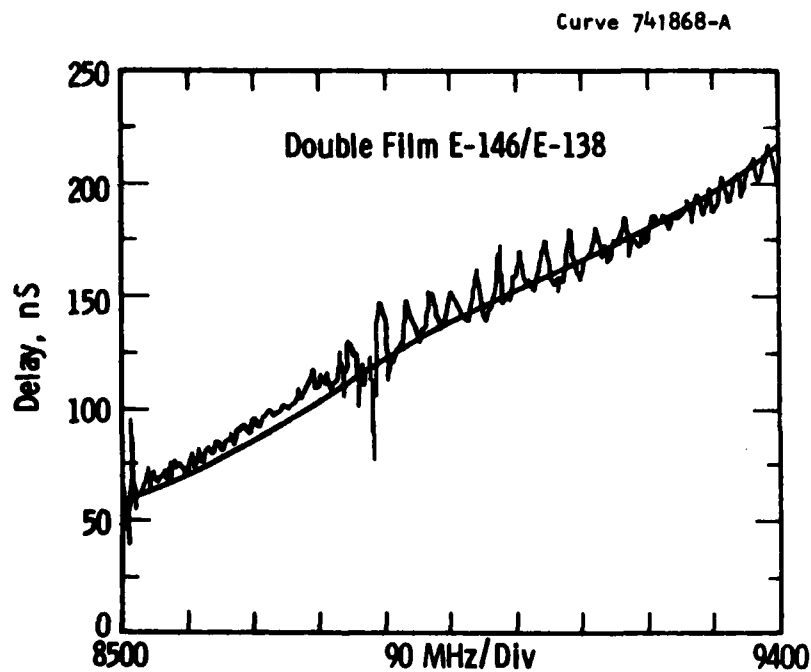
Figure 75. Calculated and measured (jagged curve) delay versus
frequency for symmetric FVWs propagating in two 20 μm thick
YIG films spaced 40 μm apart; H = 2910G, ground plane
spacings, respectively, 635 μm and 0.5 cm.

140

sample. As with previous measurements, the agreement with calculation
is good and an approximately linear delay variation is seen over 0.9 GHz
of bandwidth. As with the single-film-plus-ground-plane, there is a
slow W-shaped variation in delay superposed on the linear response.
However, the main source of present concern is not this but the more
rapid delay ripple most evident in the upper two thirds of the graph.
This type of rapid delay variation seems to be a common feature of many
of the measurements using FVWs and is mirrored in the amplitude
response. At present, its source cannot be identified with certainty,
but it is not due to any interference effect between symmetric and
antisymmetric modes, for example. Calculations show these modes to have
much too dissimilar wave numbers to give an interference pattern of the
periodicity shown in Figure 75. Their wave numbers differ by about one
order of magnitude more (100 cm^{-1}) than that required (10 cm^{-1}) to
produce the observed modulation effects.

6.4 Epitaxial Growth of GGG Films

Previous work[29] on the growth of multiple YIG films used a
lanthanum- and gallium-doped YIG layer, with low $4\pi M$, as a nominally
nonmagnetic spacer between two high $4\pi M$ layers. Here, work is described
on the epitaxial growth of gadolinium gallium garnet (GGG) by l.p.e. as
a possible nonmagnetic, dielectric spacer medium between two YIG films.
Initial epitaxial growth was performed using one inch diameter GGG
substrates and the first of the melt compositions listed in Table 3.
Melt 1 is approximately the same as that reported previously[30] as a
polish for GGG. Films were grown from melt 1, but it was not possible
to supersaturate the melt by more than a few °C without the formation of
crystallites which floated on the melt surface and caused defects in the
epitaxial film. The composition of the crystallites was not determined,
but a comparison of the Ga_2O_3/Gd_2O_3 molar ratio (2) with the Fe_2O_3/Y_2O_3
ratio (>12) in a YIG melt indicated that the crystallites may possibly
be a second phase. Because of this, the amount of Ga_2O_3 in the melt was
doubled in composition 2 of Table 3. It was possible to supersaturate

Table 3

MELT COMPOSITIONS FOR GGG EPITAXIAL GROWTH

Melt Composition	Weight in grams					Saturation temp. °C	Film/Substrate lattice Mismatch Å
	PbO	B_2O_3	Ga_2O_3	Gd_2O_3	Sm_2O_3		
1	2753.1	73.50	87.90	85.50	--	946	
2	2753.1	73.50	175.82	85.50	--	1065	~.006
3	3207.1	85.60	175.82	85.50	--	998	
4	3000.0	80.50	128.18	62.33	--	950	
5	3165.0	84.91	135.23	62.33	3.320	946	~.004
6	3360.0	88.86	142.28	62.33	6.630	941	~.002
7	3555.0	93.27	149.33	62.33	9.945	960	~ 0
8	3555.0	93.27	213.42	62.33	9.945	936	

142

for l.p.e. owing to rapid PbO evaporation. In melts 3 and 4, the PbO/B_2O_3 ratio was kept constant but the $(PbO + B_2O_3)/(Gd_2O_3 + Ga_2O_3)$ ratio was increased. This decreased the saturation temperature to below $950^{\circ}C$ as desired. The dependence of growth rate on melt temperature is shown in Figure 76 for compositions 1 to 6.

X-ray measurements showed a lattice mismatch of approximately 0.006Å for films of melts 1 through 4. This was anticipated since the Czochralski-grown GGG substrate material is nonstoichiometric and has a lattice parameter of 12.382Å compared with the stoichiometric value of 12.376Å. An epitaxial GGG layer 39 μm thick was grown on a 20 μm thick epitaxial YIG film which had been grown on a GGG substrate. The GGG and YIG films were cracked on cooling to room temperature after growth. Possible dopants which would decrease the GGG film to substrate mismatch were, therefore, investigated.

Flux-grown GGG, SmGG $(Sm_3Ga_5O_{12})$, and NdGG $(Nd_3Ga_5O_{12})$ have lattice parameters of 12.377, 12.433, and 12.502, respectively. Thus, a lattice parameter of 12.382 to match Czochralski-grown GGG should be obtained with films of composition $Gd_{2.7}Sm_{0.3}Ga_5O_{12}$ or $Gd_{2.86}Nd_{0.14}Ga_5O_{12}$, assuming Vegard's rule applies. The growth of Sm-doped GGG was investigated with melts of compositions 5, 6, and 7. Sm:GGG films grown from composition 7 showed a lattice mismatch of approximately zero. Accurate matching of the lattice parameters of the film and substrate was necessary since calculations showed that interesting and potentially useful results are obtained with double YIG-film structures when the dielectric spacing between the YIG film is approximately twice the YIG film thickness. Thus, using 20 μm thick YIG films, we have a total epitaxial growth thickness of 80 μm. This thickness of film will crack when cooled to room temperature unless the lattice mismatch is <0.002Å.

Surface quality of the Sm:GGG films is very important since a second YIG layer will be grown over the Sm:GGG film. Two types of defects were observed in the Sm:GGG films. The first, which was initially found both on thick and thin films, resulted in areas which

Curve 730420-A
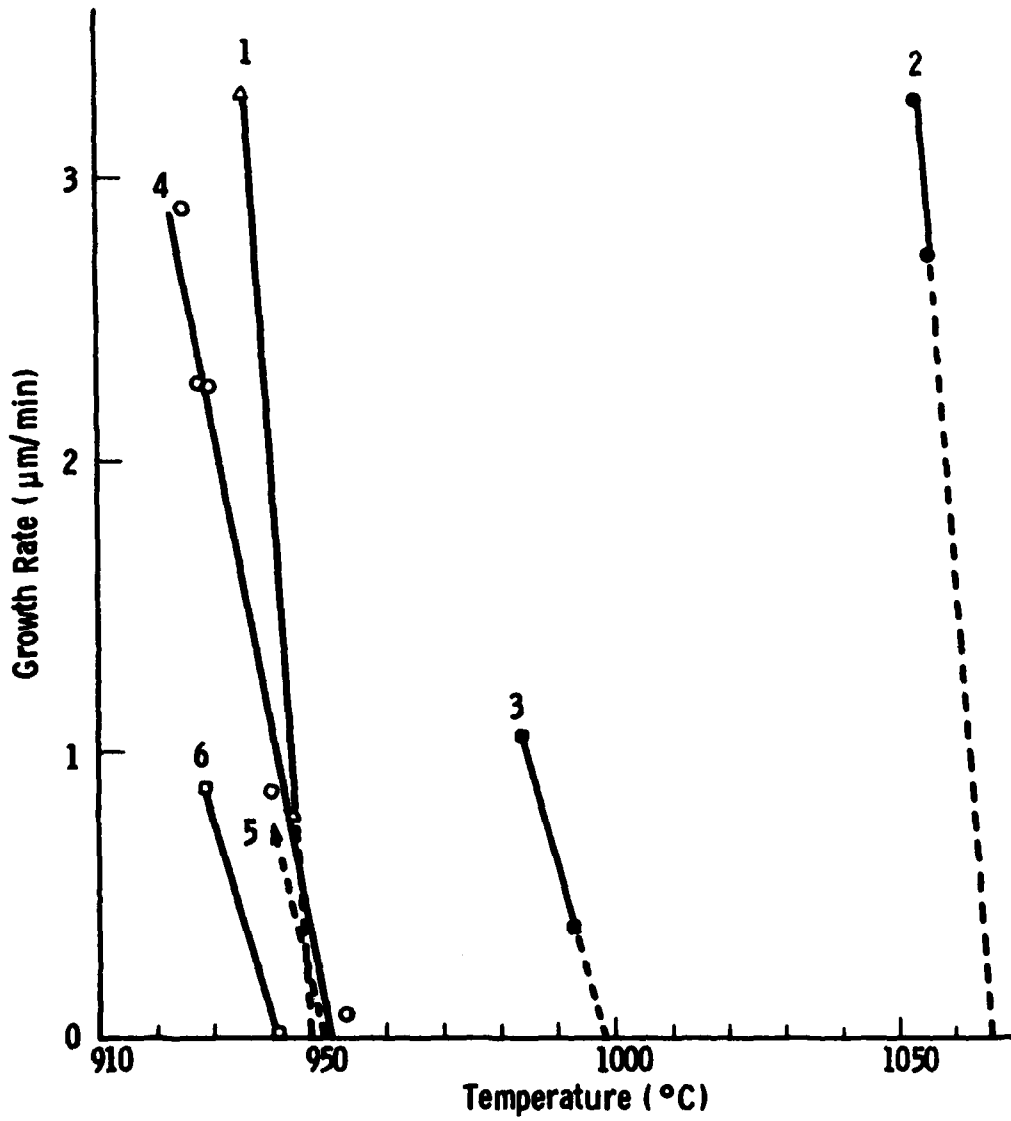
Figure 76. Growth rate as a function of temperature for melt
compositions listed in Table 3.

appeared "hazy." This appeared to be independent of melt composition and growth temperature at least for the ranges covered in Table 3. After considerable time and effort, the "hazy" effect was found to be dependent upon the angle of the substrate relative to the melt. Initially, substrates were held at an angle of 10° to the horizontal in the l.p.e furnace to allow good drainage of flux from the substrate following growth. This technique works successfully with epitaxial YIG growth. However, it was found necessary to reduce the substrate angle to $< 2^{o}$ in order to obtain haze-free GGG films on 2 inch diameter substrates. Using such small substrate angles, the flux was not cleared from the substrate until spinning commenced. The "haze" could be due to finely divided particles on the melt surface which adhered to the substrate as it was withdrawn, although examination of the melt surface showed it to be clear with no evidence of crystallized particles on the melt surface.

The second type of defect was a problem only on thick films, > 30 μm, and appeared to be due to garnet crystallites nucleated or attached to the film surface during the growth period. This effect may have been caused by spontaneous nucleation of garnet in the GGG melt, which is possible since the melt may be below saturation temperature for two hours or more during a growth run. Reliable techniques to minimize this second type of defect were not developed, although it appeared that the defect density was dependent upon the total time below the saturation temperature.

Recently published work[31] has shown that GGG will crystallize out of a PbO, B_2O_3, Gd_2O_3, Ga_2O_3 melt over a very wide range of Ga_2O_3/Gd_2O_3 ratios, i.e., $1.33 < Ga_2O_3 < 25$. Future work should investigate the optimum melt composition for the growth of low-defect, thick Sm:GGG films.

The YIG films grown for these experiments were typically 20 μm thick and had a lattice mismatch of approximately 0.003Å. The fmr linewidth measured on samples grown under the same conditions was < 0.5

145

Oe. Forward-volume wave transmission measurements[32] were performed on the complete film after each growth step. It was found that the growth of a Sm:GGG layer on top of the first YIG layer produced no detectable change in the transmission loss except for those due to spacing the YIG film further from the transducer. Several double YIG films each 20 μm thick but separated by Sm:GGG layers of thickness in the range 10 μm to 40 μm were produced to enable delay line measurements to be performed over a wide range of YIG film spacings. The Sm:GGG films were grown from a melt of composition 8 in Table 3. Note that with the growth of thick multiple layers the tolerance to thermal shock decreases, and it was found necessary to reduce the withdrawal rate from the furnace to prevent breakage.

A photograph of a smooth broken edge of a YIG/Sm:GGG/YIG/GGG substrate structure is shown in Figure 77 at 320X magnification. The first YIG layer, i.e., the lowest light band in the figure, was measured by an optical interference technique to be 19 μm thick. Based on this calibration, the thickness of the Sm:GGG and top YIG layers are 39.6 μm and 18.9 μm, respectively. Following growth of the top YIG, film samples for delay line measurements were cut to be 25 mm long and 5 mm wide. The ends of the YIG strips were bevelled at an approximately 1/2° angle to prevent reflections. The polished ends of two samples are shown in Figure 78. In both cases the thickness of the first YIG layer was measured by an optical interference technique and the thickness of the Sm:GGG and the top YIG layer were estimated from measurements of weight gain. In this figure the YIG layers appear as two bright horizontal bands. Device measurements performed on these films were described in the preceding sections.

146

Figure 77. Photograph (320X) of edge of broken YIG/Sm:GGG/YIG/GGG substrate. GGG substrate is in bottom half of photograph. The YIG layers show as light bands. The first YIG layer, i.e., lowest light band in figure was 19 μm thick measured by optical interference.

147
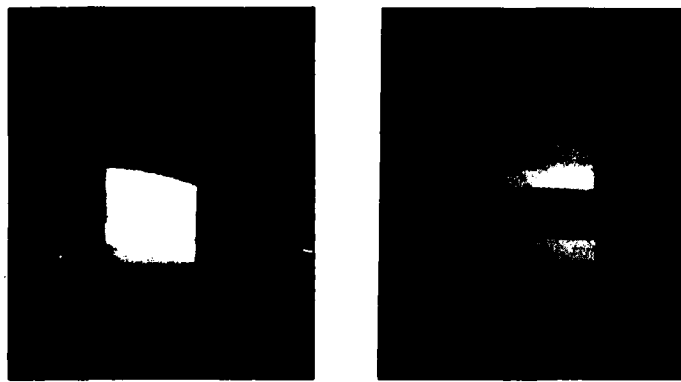
(a)   (b)

Figure 78.   Polished ends of two double YIG film samples. (a) YIG
             (19.6 µm), Sm:GGG (27.8 µm), YIG (19.8 µm). (b) YIG (20 µm),
             Sm:GGG (40.4 µm), YIG (20.8 µm).

148

7. CONCLUSIONS

Magnetostatic wave delay lines have the potential for implementation of low phase error ($<20^o$) variable delay lines using an "up-chirp" and "down-chirp" delay line in cascade. Calculations on simple single film devices indicated that they will be suitable for use where the delay variation is less than 10 nS with bandwidth of >200 MHz. Techniques, such as variable ground plane spacings and compensating transducer structures, which will further reduce the phase error due to the MSW dispersive characteristics, have been developed. These new techniques will allow construction of variable delay lines with an approximately 100 nS delay range, required for large phased array antennas, and also dispersive delay lines for use in compressive receivers where differential delays of >200 nS over bandwidth in the range 500 MHz to 1 GHz are desired.

Experimental verification of the predicted low phase errors has been prevented by the presence of amplitude and phase ripple arising from multimode propagation, triple transit, etc. Reduction of ripple to acceptable levels is seen as the most important direction for future work. Ripple is discussed in more detail later in Subsection 7.1 of these conclusions.

Studies of MSW propagation in arbitrary magnetized YIG films has shown that electronically variable delay can be achieved in a single MSW device. A delay variation of $\pm$ 20% was achieved by a 24° change in bias-field orientation. The device bandwidth was 150 MHz at a center frequency in X-band.

Beam steering of FVW has been studied experimentally and explanations for this phenomena sought. Diffraction of the FVW at a transducer edge is seen as the most likely cause. Beam steering is a

149

potential cause of ripple on FVW delay lines but further work is required to confirm this.

MSW propagation in double YIG films was studied both theoretically and experimentally using both separate YIG films and epitaxially grown YIG/Sm:GGG/YIG/GGG substrate structures. Agreement between theory and experiment was very good. At present, double YIG film structures show phase errors which are similar in magnitude to those of single films with an appropriately spaced ground plane. Double films, however, have the potential for lower insertion loss since the resistive losses due to the ground plane can be reduced. Multifilm techniques can also be extended to larger numbers of layers, e.g., three or four YIG layers separated by GGG spacers yielding low phase error delay lines. Multiple YIG film structures have the potential problem of multiple mode propagation since the number of possible modes increases with the number of layers. Transducer studies, however, indicate that the desired modes can be excited preferentially, at least in double film structures.

7.1 Ripple

Amplitude and phase ripple with origins other than MSW dispersion is at present the most significant obstacle to the systems application of MSW delay lines. Two factors have to be considered, the origins of the ripple and the accurate measurement of phase errors of $<20^{\circ}$ at microwave frequencies. Assuming an automatic network analyzer such as an HP 8409C is used, the optimum measurement technique may be to "best fit" the phase measurements to a quadratic phase with frequency variation and display the phase error. This will require a software modification for the 8409C.

Amplitude and phase ripple are intimately related and are due to any mechanism which can cause either frequency selective coupling of the desired mode into another nonpropagating or highly attenuated mode, or interference between the desired mode and another signal. An example of

150

the first mechanism is in coupling between FVW or SW and exchange[32] spin waves, which produces regularly spaced narrow-band absorbtions or "notches" in the delay line transmission response. This effect is most severe with FVWs and is attributed to nonuniformities in the magnetic properties through the thickness of the YIG film. Another example could be scattering of the FVW into higher order thickness modes (or exchange spin waves) by defects on the YIG film surface.

Interference can arise with signals due to end reflections, transducer reflections, higher order thickness and width modes, and electromagnetic feedthrough. End reflections can be minimized by use of some absorbing material such as poly-YIG, recording tape, or thin resistive metal on the ends of the delay line. The ends can also be bevelled in thickness at a shallow angle, tapered in width, or damaged by sand-blasting or rough polishing. Bevelling at an approximately 1° angle and evaporation of a thin ($<500Å$) aluminum layer have been found effective.

Prevention of transducer reflections requires that either the coupling of the transducer to the MSW is weak, which is usually not desirable, or that the electromagnetic output port of the transducer is well matched. The severity of ripple due to end or transducer reflection, i.e., triple transit, can be estimated through use of simple equations.

Amplitude ripple $= 20 \log [(1 + K_1^2)/(1 - K_1^2)]$	dB	peak to peak
Phase ripple $= 2 \tan^{-1} K_1^2$	degrees	" " "
Delay ripple $= 4 D K_1^2$	nS	" " "

where K_1 is the fraction of the incidence energy reflected and D is the time delay for one transit. Some representative values are shown in Table 4.

Similar relationships will hold for interference due to the higher order modes. It can be seen from Table 4 that the most sensitive parameter is the delay. Thus, care must be taken when specifying

Table 4

REPRESENTATIVE VALUES FOR TRIPLE TRANSIT RIPPLE

K_1	Amplitude Ripple(dB)	Phase Ripple($^{\circ}$)	Delay Ripple Normalized
0.1	0.17	1.18	0.04
0.2	0.69	4.58	0.16
0.4	2.80	18.18	0.64

desired delay line characteristics. For example, it may be more realistic to specify a phase ripple together with a maximum level for "spurious" time-separated pulses rather than specify a maximum delay ripple.

Higher order thickness modes are launched by the microstrip transducer but, since their wave number increases rapidly with frequency, their effects are confined to the low-frequency end of the FVW band. Width modes are degenerate with the lowest order mode at high wavenumbers but are nondegenerate at low wave numbers and if excited can cause significant amplitude and delay ripple.[33] Ripple due to width modes can be avoided by using wide films so that the modes are almost degenerate or by matching the driving transducer current distribution to the field pattern of the desired mode. Transducer-mode field matching is complicated in thick film by the effects of launching the MSW on the current distribution. The radiation resistance into a FVW in a thick film can be as high as 200 Ω/cm and, in a long transducer, results in an exponential decay in current along its transducer length. A related possible cause of ripple is the mechanism, whatever it is, which produces beam steering of FVWs.

Ripple due to e.m. feedthrough can be reduced to negligible levels with careful design of the delay line box.

In general, ripple is most severe in FVW delay lines using thick YIG films (>30 μm) and is much less of a problem in SW and BVW

152

devices. However, FVW devices <u>are</u> required since they can operate at X-band and above with much wider bandwidths than SW devices and can tolerate higher power levels in S-band than SW devices.

7.2 Future Work

Presently available MSW variable delay lines based on "up-chirp" and "down-chirp" devices in cascade show characteristics which are promising for some phased array applications. Effort in the short term should be directed toward implementing these devices for systems use. Topics to be studied in the short term include, in approximate order of importance:

1. Ripple reduction.

2. Transducer matching to minimize insertion loss.

3. Bias magnet design to reduce size and weight.

4. Tuning magnet design to minimize switching speed.

5. Temperature stabilization.

6. Resettability -- required for microprocessor control of variable delay line and phase shifters.

7. Systems studies.

In the slightly longer term, techniques which will improve the delay line performance should be studied. These include:

1. Low phase error techniques for single and double film devices.

2. Multiple YIG film structures.

3. Unidirectional transducers for low-loss volume wave devices.

4. Other variable delay techniques, e.g., variable bias field angle, variable spacing between films.

8. REFERENCES

1. J. C. Sethares, J. M. Owens, and C. V. Smith, Jr., Electronics Letters, 16, 825 (1980).

2. Michael R. Daniel, J. D. Adam, and T. W. O'Keefe, IEEE Sonics and Ultrasonics Symposium, Proceeding, New Orleans (1979) IEEE Cat. No. 79CH1482-9.

3. C. V. Smith, Jr., J. M. Owens, T. J. Mean II, and N. D. Parikh, IEEE Trans MAG-15: 1738 (1979).

4. W. L. Bongianni, Microwave Journal, 17: 49 (1974).

5. Z. M. Bardai, J. D. Adam, J. H. Collins, and J. P. Parekh, Magnetism and Magnetic Materials, 1976, AIP Conference Proc. No. 34: 268 (1977).

6. J. D. Adam, T. W. O'Keeffe, and Michael R. Daniel, Proc. Soc. Photo-Optical Instrumentation Engineers, 241: 96 (1980).

7. J. D. Adam, Michael R. Daniel, T. W. O'Keeffe, and P. R. Emtage, WPAFB Avionics Laboratory, Final Report, "Magnetic Surface Wave Device Technology," Contract No. F33615-77-C-1068 (1981).

8. SUPER-COMPACT, trade mark of the Compact Engineering Company, 1131 San Antonio Road, Palo Alto, CA 94303.

9. P. R. Emtage, J. App. Phys., 49, 4475 (1978).

10. Michael R. Daniel, J. D. Adam, and D. K. Schroder, Westinghouse Electric Corp., unpublished (1980).

11. W. L. Bongianni, Final Report USAF Contract AFAL-TR-71-275, p. 24-27 (1971), Air Force Avionics Laboratory Wright Patterson AFB, OH 45433.

12. IMSL Library, Edition 9 (1MSL S-PA9) for Univac 1100/80 Computer, IMSL Inc., 7500 Bellaire Blvd., Houston, TX 77036.

13. J. D. Adam and J. H. Collins, Proc. IEEE 61, 794 (1976).

14. F. R. Morgenthaler, J. Appl. Phys. 41, 1014 (1970).

15. J. P. Parekh, Proc. IEEE 61, 1371 (1973).

16. N. D. J. Miller, Phys. Stat. Solidi (a) 43, 593 (1977).

17. N. D. J. Miller, IEEE Trans. Magnetics 14, 829 (1978).

18. S. N. Bajpai and N. C. Srivastava, Phys. Status Solidi (a) 27, 307 (1980).

19. H. Goldstein, Classical Mechanics, Addison-Wesley Publishing Co., Inc. p.107 (1969).

20. N. D. J. Miller Phys. Status Sol(a) 37, 83 (1976).

21. T. Koike, IEEE MTT-S Digest, p. 86 (1982).

22. S. N. Bajpai, J. Appl. Phys. 50, 6564 (1979).

23. J. P. Parekh, H. S. Tuan, J. Appl. Phys. 52, 2279 (1981).

24. C. V. Smith, J. M. Owens, N. D. Parekh, R. L. Carter, IEEE Trans. on Mag. MAG-17, 2967 (1981).

25. J. E. Mee, G. R. Pulliam, J. L. Archer, P. J. Besser, IEEE Trans. on Mag. MAG-5, 717 (1969).

26. G. F. Dionne, Mat. Res. Bull, 6, 805 (1971).

27. A. Sommerfeld, "Optics," Academic Press, p. 254 ff(1954).

28. Michael R. Daniel and P. R. Emtage, J. Appl. Phys., 53, 3723 (1982).

29. L. R. Adkins and H. L. Glass, Electronics Letters, 16, 503, 1980.

30. J. M. Robertson, M. J. G. van Hout, M. M. Jansen, and W. T. Stacy, J. Cryst. Growth 18, 194 (1973).

31. E. A. Giess, M. M. Faktor, R. Ghez, and C. F. Guerce, J. Cry. Growth 56, 576 (1982).

32. J. D. Adam, T. W. O'Keeffe, and R. W. Patterson, J. App. Phys., 50, 2446 (1979).

33. J. D. Adam and S. N. Bajpai, 1982 Joint Intemag and MMM Conf., paper EC-06 to be published in IEEE Trans. on Magnetics.

APPENDIX I

EXCITATION OF MAGNETOSTATIC WAVES BY COPLANAR STRUCTURES

The theory of excitation follows Emtage's method,[9] save that the normal component of magnetic field in the gaps is treated as the excitatory agent, rather than the current itself. The field is later related to the current through the shape factors s(k) described in Section 2.7.

We consider waves travelling in the x direction on a ferrite film between the planes $y = d$ and $y = 0$. The lower plane is metallized, apart from gaps along the z direction; currents flow along the z direction, and all fields, etc. vary in the xy-plane only.

The boundary condition on the metallized plane is

$$B_y(y=0) = 0, \text{ except on the gaps.} \quad [A1]$$

As in reference 9, we define a relative surface permeability through

$$\mu^s = -iB_y/\mu_o H_x. \quad [A2]$$

The secular equation, from reference 9, with $\mu^s = 0$ on $y = 0$, is

$$\mu^s = 0 = \frac{\pm 1 + (\mu_{11}\mu_{22} - \mu_{12}^2 \mp \mu_{12}) \dfrac{1}{\beta\mu_{22}} \tanh \beta k d}{1 + (\mu_{12} \pm 1) \dfrac{1}{\beta\mu_{22}} \tanh \beta k d} \quad [A3]$$

where the ± signs are taken as k is positive or negative, the terms μ_{ij} are the relative permeabilities of the ferrite layer, and where

156

$$\beta^2 = \mu_{11}/\mu_{22}.$$

In the plane $y = 0$, define the Fourier transforms of B_y and H_x through

$$B_k = \int B_y(x)e^{-ikx}dx,$$

$$H_k = \int H_x(x)e^{-ikx}dx.$$

From the definition of the surface permeability in Equation A2, therefore,

$$H_x(x) = -\frac{1}{2\pi\mu_o} \int \frac{B_y(k)}{\mu^s(k)} e^{ikx}dk$$

But $\mu^s(k)$ is zero at the roots $k_{\pm}$ of the secular equation, Equation A3. Consider the positive root; the above relation yields

$$H_x(x) = \frac{1}{\mu_o} \frac{B_y(k_+)e^{ik_+x}}{\partial\mu^s/\partial k_+}$$

$$= \frac{1}{\mu_o} \frac{e^{ik+x}}{\partial\mu^s/\partial k_+} \int dx' B_y(x')e^{ik_+x'} \qquad [A4]$$

From the boundary condition, Equation A1, B_y is zero everywhere except on the gaps. The above relation therefore describes a wave originating at the gaps in the conducting sheet and travelling to the right. From reference 9, the power travelling to the right is

$$P^+ = -\frac{1}{2} \frac{\omega}{k_+} \mu_o |H_x|^2 \frac{\partial\mu^s}{\partial k_+},$$

$$= \frac{1}{2} \frac{\omega}{k_+} \mu_o |H_y(k_+)|^2 / \frac{\partial\mu^s}{\partial k_+} \qquad [A5]$$

where $H_y(k_+)$ is the Fourier transform of the field on the gaps.

This relation can be expressed in terms of a radiation resistance, provided that we know the relation of H_y in the gaps $\ldots$ the current J. We assume a relation of the form

$$H_y(k) = \frac{1}{2} s(k)J, \qquad [A6]$$

where $s(k)$ is the shape function in the text, and the factor 1/2 will be explained below. The radiated power now has the form

$$P^+ = \mu_0 \omega K^+ |s(k_+)^2 J^2, \qquad [A7]$$

where the coupling constant K^+ is

$$K^+ = 1 / \left(8k_+ \frac{\partial \mu^s}{\partial k_+} \right) .$$

Equation A3 for μ^s yields, at the roots $\mu^s = 0$,

$$K^{\pm} = \pm \frac{1}{8k_{\pm} d} \frac{\mu_{22}}{\mu_{12}^2 - \mu_{11}\mu_{22}} \qquad [A8]$$

Substitution of appropriate expressions for the μ_{ij} yields the equations in the text for the surface wave-coupling constants.

The Fourier Transforms s(k)

The shape functions s are proportional to the Fourier transforms of the normal field in the gap, normalized to the total current, as in Equation A6.

We have no means of evaluating these functions when a magnetic medium is present. The following expressions are therefore approximations.

In vacuo, the tangential fields above and below the metal plane are equal and opposite, and the change in tangential field is equal to the current density $j_z(x)$. Therefore,

$$H_z(x,0+) = -H_x(x,0-) = \frac{1}{2} j_z(x).$$

The magnetic fields are derived from the gradient of a potential $\underline{H} = \nabla\psi$, where

$$\psi = \sum_k \psi_k e^{ikx} e^{-|k|y} .$$

It follows that

$$|H_y(k)| = |H_x(k)| = \frac{1}{2} |j_z(k)|. \qquad [A9]$$

This accounts for the factor 1/2 in Equation A6, and the radiated power in Equation A7 can be set in the familiar form

$$P^+ = \mu_o \omega K^+ |j_z(k)|^2.$$

While this form is both familiar and exact in the theory of microstrips, it is here only approximate, and it is Equation A5 that is exact.

The Fourier transforms in the text are obtained from the fact that a field

$$H_y = [(\frac{w}{2})^2 - x^2]^{-1/2}$$

in a gap is associated with a current density.

$$j_z = \pm 2 [x^2 - (\frac{w}{2})^2]^{-1/2}$$

the $\pm$ signs being on opposite sides of the gap. This form holds for distances x short compared with the electromagnetic wavelength.

For the slot line we need only one such term, the current J being the total current on one side of the line. The coplanar waveguide has been approximated as a superposition of two such distributions, J being the current in the center strip.

159

Magnetostatic volume wave propagation in a ferrimagnetic double layer [a]

Michael R. Daniel and P. R. Emtage

Westinghouse Research and Development Center, Pittsburgh, Pennsylvania 15235

Using the technique of "surface permeabilities," an expression is derived for the dispersion of magnetostatic waves propagating in two close proximity ferrimagnetic films. Two modes of propagation for volume waves are identified respectively as the symmetric and antisymmetric modes from the symmetry of the rf magnetization. Useful group delay behavior is shown to result from films of equal thickness. Some measurements are reported using two yttrium iron garnet films sandwiching simple single finger transducers. Difficulties in exciting the symmetric forward volume mode are explained in terms of the coupling coefficients for these double film structures.

PACS numbers: 75.30.Ds, 75.50.Gg, 85.70.Ge

I. INTRODUCTION

There have recently been a number of papers, [1-3] of a mostly theoretical nature, describing the propagation of magnetostatic surface waves in two ferrimagnetic films coupled together by their close proximity. Scant attention has been given to the propagation of magnetostatic volume waves in a double film structure. Our interest in the volume waves was motivated by practical considerations to see if they offered any useful time delay characteristics for microwave delay-line applications. Additionally, the problem provided an opportunity to demonstrate the useful technique of "surface permeabilities" [4] in a relatively complicated situation. We will describe the propagation characteristics for forward volume waves (FVWs) in which the static magnetic bias field is applied normal to the plane of the films, and also for backward volume waves (BVWs) with the bias field in-plane and parallel to the propagation direction. Measurements of time delay versus frequency are presented for epitaxially grown Yttrium Iron Garnet (YIG) films. Finally, transducer coupling strengths are calculated for films of equal thickness; these coupling strengths help to explain some of the experimental results.

II. THEORY

A. Introduction

1. General

The surface permeability μ' is useful in the analysis of systems with plane parallel discontinuities (such as magnetic films) because its value at each interface can be calculated from its value at the interface above or below [4,5] (see Eq. 7); further μ' is known at the upper and lower boundaries of the system, which are metal or vacuum. For a sample of N layers, therefore, N algebraic iterations yield the secular equation; this process is simpler than the usual method of solving $2N$ simultaneous equations for the field amplitudes.

We consider waves travelling along the x axis in a film bounded by planes $y = $ const. The field $\mathbf{h}$ and flux density $\mathbf{b}$ are

$$b_x/\mu_0 = \mu_{11}h_x + i\mu_{12}h_y ,$$
$$b_y/\mu_0 = -i\mu_{12}h_x + \mu_{22}h_y . \tag{1}$$

In the magnetostatic approximation we set $\mathbf{h} = \nabla\psi$, where ψ is a potential. From $\nabla \cdot \mathbf{b} = 0$, Eq. (1) yields

$$\mu_{11}\frac{\partial^2\psi}{\partial x^2} + \mu_{22}\frac{\partial^2\psi}{\partial y^2} = 0 . \tag{2}$$

A magnetostatic wave of wave number k along the x axis is therefore derived from a potential

$$\psi = e^{i(kx-\omega t)}[Ce^{\beta k y} + De^{-\beta k y}] , \tag{3}$$

where

$$\beta^2 = \mu_{11}/\mu_{22} , \tag{4}$$

and where C and D are constants found from the boundary conditions.

2. The surface permeability

The surface boundary conditions are that the tangential field h_x and the normal flux b_y be continuous across an interface $y = $ const. These conditions are satisfied if the ratio b_y/h_x, which has the dimensions of a permeability, is continuous everywhere.

We therefore define a relative surface permeability μ' as

$$\mu'(y) = -ib_y(y)/\mu_0 h_x(y) , \tag{5}$$

where the factor i is introduced because b_y and h_x are out of phase.

Consider a magnetic system extending between y_{min} and y_{max}. The magnetic potential ψ in Eq. (3) must be small far from the system. For positive k, then, the constants in Eq. (3) are $C = 0$ when $y > y_{max}$, and $D = 0$ when $y < y_{min}$. In the vacuum regions, therefore,

$$\mu' = \pm 1 , \quad (y > y_{max}), \tag{6a}$$
$$\mu' = \mp 1 , \quad (y < y_{min}),$$

the upper or lower signs being taken as k is positive or negative. If one of the limits of the system is a perfectly conducting metal layer, where $b_y = 0$, then the boundary condition becomes

$$\mu' = 0, \text{ (metal layer)} . \tag{6b}$$

160

Suppose that μ^s is known in the plane $y = y_1$ and that a continuous medium extends between y_1 and y_2. The ratio

C/D in Eq. (3) can be found from $\mu^s(y_1)$, and $\mu^s(y_2)$ can then be calculated. The result is

$$\mu^s(y_2) = \frac{\mu_{22}\mu^s(y_1) + [\mu_{11}\mu_{22} - \mu_{12}^2 - \mu^s(y_1)\mu_{12}]\beta^{-1}\tanh \beta k (y_1 - y_2)}{\mu_{22} + [\mu^s(y_1) + \mu_{12}]\beta^{-1}\tanh \beta k (y_1 - y_2)} . \tag{7}$$

Therefore we can use Eq. (7) to iterate μ^s from an upper (or lower) surface where it is known, through Eqs. (6), until we reach another surface where it is known. The secular equation is obtained by requiring that these values be the same.

More generally, in a system of N layers there are discontinuities at $y_1, y_2, \ldots y_{N+1}$ ($y_1 > y_2$, etc.); $\mu^s(y_1)$ and $\mu^s(y_{N+1})$ are known from the boundary conditions. Denote by $\mu^{sp}(y_i)$ the value of μ^s at y_i calculated from all layers above y_i, and by $\mu^{sn}(y_i)$ the value found from all layers below y_i. Thus

$$\mu^s(y_1) \rightarrow \mu^{sp}(y_2) \ldots \rightarrow \mu^{sp}(y_i) ,$$

$$\tag{8}$$

$$\mu^s(y_{N+1}) \rightarrow \mu^{sn}(y_N) \ldots \rightarrow \mu^{sn}(y_i) ,$$

where the sign $\rightarrow$ means "leads to." The secular equation is

$$\mu^{sp}(y_i) = \mu^{sn}(y_i) . \tag{9}$$

The use of this procedure is demonstrated in the following section.

B. Secular equations

1. Single layer

For a magnetic layer extending between $y = 0$ and $y = d$ we have $\mu^s(d) = \pm 1$, $\mu^s(0) = \mp 1$. Equations (7) and

(9) then give

$$\frac{1}{\beta}\tanh \beta k d = \frac{\mp 2\mu_{22}}{\mu_1\mu_{22} + 1 - \mu_{12}^2} , \tag{10}$$

which is the usual result for a single layer.

2. Double layer

We consider the system sketched in Fig. 1. Upper and lower layers of thicknesses d_1 and d_2 are separated by a vacuum layer extending between $y = 0$ and $y = t$. There are ground planes at distances s_1 above the upper layer and s_2 below the lower layer.

The surface permeabilities at the ground planes are $\mu^s = 0$, from Eq. (6b). At the upper and lower magnetic surfaces, therefore, Eq. (7) gives

$$\mu^{sp}(t + d_1) = \tanh k s_1 ,$$

$$\mu^{sn}(-d_2) = -\tanh k s_2 .$$

These ratios tend to ± 1 when s is large, as Eq. (6a) requires. From Eq. (7), the surface permeabilities at the edges of the central vacuum layer are

$$\mu^{sp}(t) = \frac{\mu_{22}^{(1)}\tanh k s_1 + [\mu_{11}^{(1)}\mu_{22}^{(1)} - (\mu_{12}^{(1)})^2 - \mu_{12}^{(1)}\tanh k s_1]\beta_1^{-1}\tanh \beta_1 k d_1}{\mu_{22}^{(1)} + [\tanh k s_1 + \mu_{12}^{(1)}]\beta_1^{-1}\tanh \beta_1 k d_1} , \tag{11}$$

$$\mu^{sn}(0) = -\frac{\mu_{22}^{(2)}\tanh k s_2 + [\mu_{11}^{(2)}\mu_{22}^{(2)} - (\mu_{12}^{(2)})^2 + \mu_{12}^{(2)}\tanh k s_2]\beta_2^{-1}\tanh \beta_2 k d_2}{\mu_{22}^{(2)} + [\tanh k s_2 - \mu_{12}^{(2)}]\beta_2^{-1}\tanh \beta_2 k d_2} .$$

These quantities each involve the properties of one layer only. The secular equations for waves of positive or negative k on either layer alone (together with the associated ground plane) are

$$D_{\pm}^{(1)} \equiv \mu^{sp}(t) \pm 1 = 0 , \quad D_{\pm}^{(2)} \equiv \mu^{sn}(0) \mp 1 = 0 . \tag{12}$$

The interaction of the films through the vacuum layer between 0 and t is obtained by calculating $\mu^{sp}(0)$ from $\mu^{sp}(t)$; Eq. (7) gives

$$\mu^{sp}(0) = \frac{\mu^{sp}(t) + [1 - \mu^{sp}(t)]\tanh k t}{1 + \mu^{sp}(t)\tanh k t} . \tag{13}$$

On equating this to $\mu^{sn}(0)$, we obtain the secular equation

$$D_+^{(1)} D_-^{(2)} - D_-^{(1)} D_+^{(2)} e^{-2kt} = 0 , \tag{14}$$

where the D's are defined in Eq. (12). When kt is large and positive, the second term represents a weak interaction between modes that belong predominantly to each film separately.

3. Symmetric system

When the two interacting layers are of the same material and thickness, with equidistant ground planes, it is still not the case that $D^{(1)} = \pm D^{(2)}$ unless $\mu_{12} = 0$. This inequality is associated with the fact that $D^{(1)}$ is constructed from μ^{sp}, while $D^{(2)}$ is constructed from μ^{sn}. It is therefore impossible to obtain symmetric or antisymmetric modes except in the case of volume waves ($\mu_{12} = 0$).

In a symmetric system with $\mu_{12} = 0$, Eqs. (11) yield $\mu^{sp}(t) = -\mu^{sn}(0)$; from Eq. (14), we find
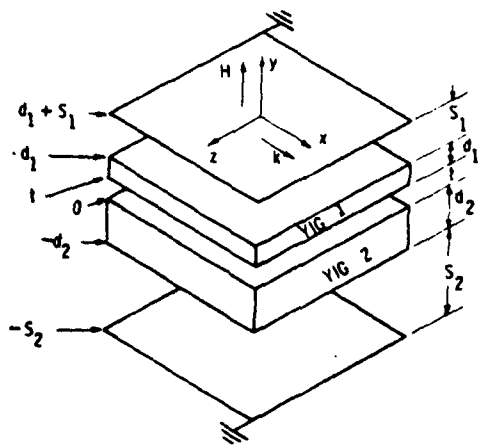
3724   J. Appl. Phys., Vol. 53, No. 5, May 1982

M. R. Daniel and P. R. Emtage   3724

161

G. 1. Double YIG film configuration; the direction of H allows opagation of FVWs.

FIG. 2. rf components of magnetization $(m_x, m_y, —)$ and field $(h, ---)$ as a function of distance normal to the plane of two 20-μ-thick films spaced 40 μ apart: L.H. curves—FVWs $(f = 9.4$ GHz, $k_s = 112.93$ cm^{-1}, $k_a = 256.75$ cm$^{-1})$; R.H. curves—BVWs $(f = 10.25$ GHz, $k_s = 122.83$ cm^{-1}, $k_a = 268.84$ cm$^{-1})$.

$$\mu^{in}(0) = \tanh \frac{1}{2} kt, \quad \text{(even in } \psi),$$

$$= \coth \frac{1}{2} kt, \quad \text{(odd in } \psi). \tag{15}$$

These modes are identified as even or odd in the magnetostatic potential because, in the central vacuum region, they correspond to $\psi \sim \cosh k [y - (1/2)t]$, $\sinh k [y - (1/2)t]$, respectively [the plane $y = (1/2)t$ is the center of the system].

Volume waves exist only in the region $\mu_{11}\mu_{22} < 0$. The quantity β in Eq. (4) is then imaginary, and we define

$$\alpha^2 = -\beta^2 = -\mu_{11}/\mu_{22}. \tag{16}$$

The secular equation is now

$$\tan \alpha kd = \frac{\mu_{22}\alpha[\tanh ks + \mu^{in}(0)]}{\mu_{22}^2\alpha^2 - \mu^{in}(0)\tanh ks}, \tag{17}$$

where $\mu^{in}(0)$ is given in Eq. (15).

In the following discussion we shall always refer to the fundamental mode as symmetric, even through, for backward volume waves, that mode is odd in the magnetostatic potential. For these waves the applied magnetic field is along the x axis, so the excursion in the magnetization is in the y direction. An odd magnetostatic potential therefore gives rise to a symmetric excitation of the system, and we regard the excitation as more significant than the potential.

This is illustrated in Fig. 2, which shows the rf field parameters $m_x(y)$ and $h_x(y)$ for FVWs and $m_y(y)$ and $h_x(y)$ for BVWs. The particular examples chosen were for two films of equal thickness 20μ, spaced 40μ apart. The ordinate values in Fig. 2 were derived from a magnetostatic potential function normalized to unity on the lower face of film no. 2. The static bias field (H) and frequency (f) were chosen to yield approximately equal wavevector (k) values for the symmetric FVW and BVW modes. It will be noted that the symmetric mode, as judged from the symmetry of the magnetization, is in both cases the fundamental mode, as judged from the wavenumber.

III. RESULTS

A. Calculations

The subsequent results were obtained from numerical solutions of Eq. (17) (for dissimilar films Eq. 14 is solved). Unless noted otherwise the following parameters were used: $S_1 = S_2 = 1$ cm; $4\pi M_1 = 4\pi M_2 = 1.8$ kG; $H_{FVW} = 3.214$ kG and $H_{BVW} = 2.991$ kG. This equation yields two sets of roots which have been termed the symmetric (S) and antisymmetric (A) modes. Each set corresponds to a fundamental thickness mode and an infinite sequence of higher-order
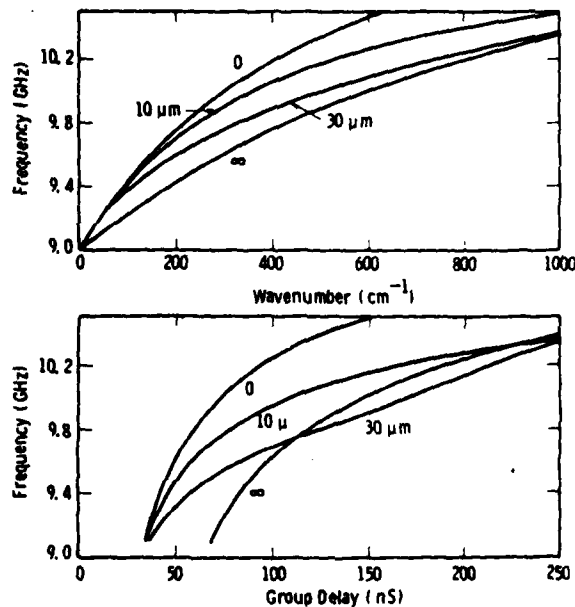
FIG. 3. Dispersion and group delay curves for a symmetric FVW propagating in two 20-μ-thick films with the film separation (t) as a parameter; $4\pi M_1 = 4\pi M_2 = 1.8$ kG, $H = 3.214$ kG, $S_1 = S_2 = 1$ cm.

162

FIG. 4. Dispersion and group delay curves for FVWs and BVWs propagating in 20-μ-thick films separated by 40 μ. The differences between the symmetric (S) and antisymmetric (A) modes are illustrated; other parameters as in Fig. 3 except $H_{\text{BVW}} = 2.991$ kG, $t_{\text{BVW}} = 30$ μ, $t_{\text{FVW}} = 40$ μ.

modes. The group delay data are the derivatives $[(1/2\pi)(dk/df)]$ of the dispersion curves expressed in nS for a 1-cm path leng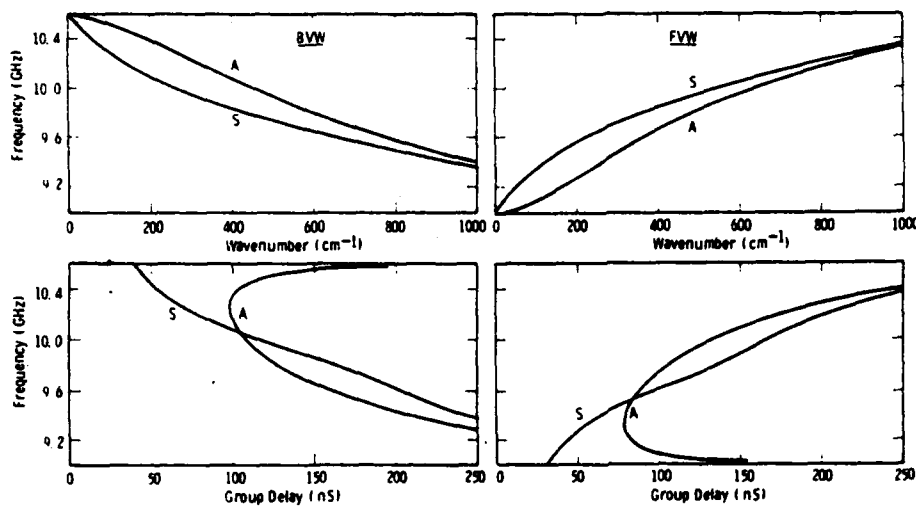th. We recognized that Eq. 14 or 17 can yield a substantial harvest of results from the permutation of all the parameters they contain. However, the following generalities did emerge: interesting results, i.e., results significantly different from those of FVW or BVW propagation in single films, are obtained from films of equal or nearly equal thickness; useful results in the context of yielding linear or constant group delays are obtained from films spaced 1 to 2 film thicknesses apart.

In Fig. 3 (upper) we illustrate the effects of different interaction strengths for the symmetric mode for FVWs in 20-μ thick films. When the film separation t is zero the dispersion curve is appropriate to a FVW in a single coalesced film of 40-μ thickness. When $t \rightarrow \infty$ the dispersion corresponds . to a FVW in an isolated 20-μ film. The film separa- . . n has a significant effect on the group delay and we note parentnetically that a value of $t = 30\mu$ gives a useful range of quasilinear delay from approximately $k = 100$ to $k = 1000$ cm^{-1}.

Figure 4 shows the dispersion and group delay results for the fundamental S- and A-modes of FVWs and BVWs in two 20-μ-thick films. From an applications point of view it was generally found that the S-mode has quasilinear group delay variation with frequency and the A-mode shows some region of quasiconstant delay. The t values of 40 μ for the FVW and 30 μ for the BVW were in fact found to give optimum group delay linearity over bandwidths of about 1 GHz for the S-mode.

One feature peculiar to double films was found for those of different magnetizations. In an external bias field H_0 these films have different operating bandwidths for magnetostatic wave excitation [γH to $\gamma H(H + 4\pi M)^{1/2}$] due to different demagnetizing fields and different $4\pi M$ values. For overlapping, but not coincident, bandwidths the dispersion relations are discontinuous. This is illustrated in Fig. 5 for magnetizations of 1.8 and 1.4 kG, respectively. If the internal bias field in film no. 1 is H then it is $(H + 4\pi M_1 - 4\pi M_2)$ in film

no. 2 for the FVW geometry. In Fig. 5 (upper) between 9 and 10.12 GHz, $\mu_{11}(1) < 0$ and $\mu_{11}(2) > 0$ for $H = 3.214$ kG. Film no. 1 supports most of the magnetostatic volume wave which decays exponentially in film no. 2. This is shown by the potential plots in Fig. 6. Both the S- and A-modes show this decay feature in film no. 2, however, the symmetry features are now gone and the terms symmetric and antisymmetric no longer describe the rf parameters. At 10.12 GHz $\mu_{11}(2) \rightarrow \pm \infty$ and a discontinuity appears in the dispersion curves. Above 10.12 GHz both μ's are negative and "normal" propagation resumes, the dispersion curves restart at
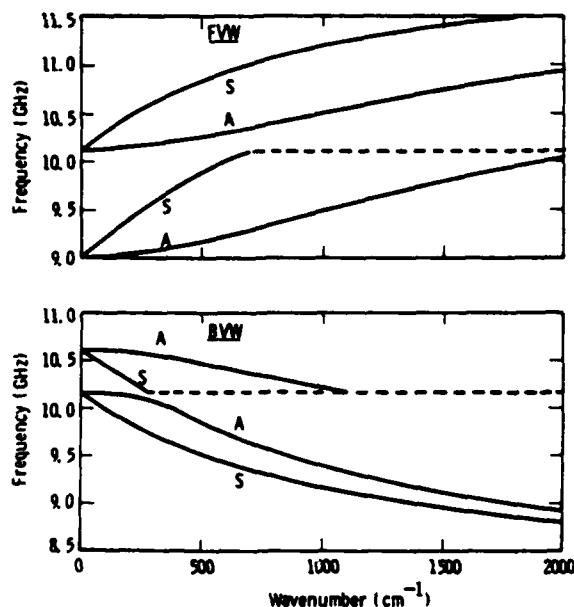

FIG. 5. Dispersion curves for FVWs and BVWs propagating in films of equal thickness but different magnetizations; $4\pi M_1 = 1.8$ kG, $4\pi M_2 = 1.4$ kG, $t = 40$ μ, $S_1 = S_2 = 1$ cm, H_{FVW} (in film no. 1) = 3.214 kG, $H_{\text{BVW}} = 2.991$ kG.

M. R. Daniel and P. R. Emtage   3726

163

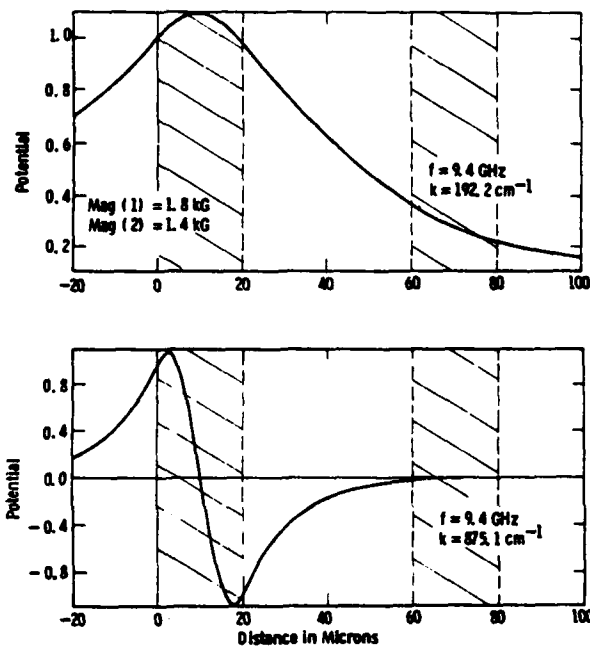FIG. 8. Experimental results of group delay vs frequency for a FVW *A*-mode in two 20-μ-thick YIG films spaced 25 μ apart.

FIG. 6. Magnetostatic potential as a function of distance normal to the plane of two 20-μ-thick films spaced 40 μ apart supporting a FVW: upper curve, the first or fundamental mode; lower curve, the first overtone.

$k = 0$. For BVW's with H in the plane of the films there is no change in the internal bias field H, but the upper frequency limit is down shifted in film no. 2 due to the lower $4\pi M_2$ value. In Fig. 5 (lower) above 10.15 GHz $\mu_{22}(1) < 0$ and $\mu_{22}(2) > 0$, the BVW is carried primarily in film no. 1 with an exponential decay in film no. 2. At 10.15 GHz, $\mu_{22}(2) = 0$, but the propagation constant β is singular since $\beta = 1/(\mu_{22})^{1/2}$ and a discontinuity in the dispersion curves result. Below 10.15 GHz both μ's are negative and "normal" propagation occurs.

B. Experiments

Three possible transducer configurations for exciting magnetostatic waves in a double film are shown in Fig. 7. The conductors supporting the microwave currents J could
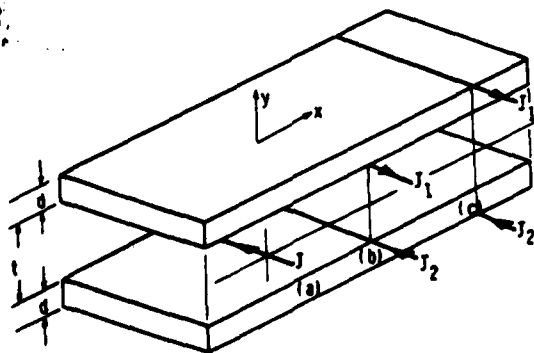
be either fine wires or conducting metal strips defined photo-lithographically. In the first experiment configuration (a) was used. Two 20-μ-thick YIG films, grown epitaxially on gadolinium gallium garnet substrates, were cut into rectangular samples 3 mm by 25 mm. The transmitting and receiving transducers were 25-μ-diam gold wires which also acted as the spacers to keep the films 25 μ apart. Group delay measurements were performed on a network analyzer (HP model 8410B) under computer control (HP model 9845B). The static bias field was provided by a 12-in. Varian magnet. The results for FVWs are shown in Fig. 8 and for BVWs in Fig. 9. From the geometry of Fig. 7(a) the rf field h_x has odd symmetry in the films. Hence, by Fig. 2 the FVW should be an *A*-mode and the BVW an *S*-mode. Comparing the group delay results in Fig. 4 with the experimental results confirms this deduction. In fact, the experimental results were found to be in very good agreement with calculation. There was considerable interest in trying to excite the FVW *S*-mode due to its linear group delay behavior. Transducer configuration 7(b) was chosen for this. The transducers were made from gold ribbon 12 μ by 50 μ in cross section. These were driven by antiphase currents from a microstrip power divid-

FIG. 7. Three possible transducer geometries for the excitation of magnetostatic waves in a double film structure.

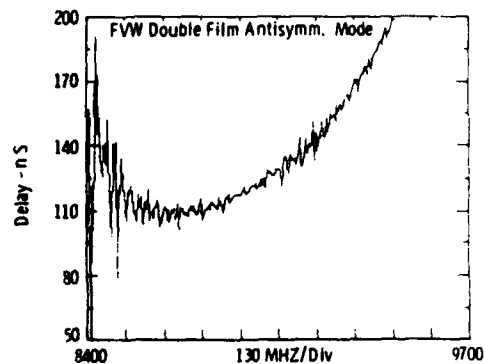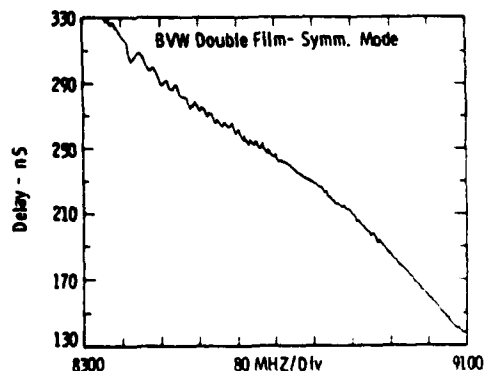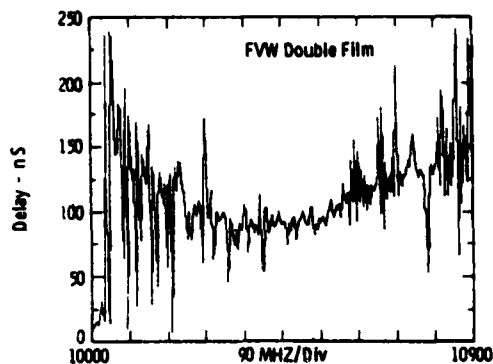FIG. 9. Experimental results of group delay vs frequency for a BVW *S*-mode in two 20-μ-thick YIG films spaced 25 μ apart

FIG. 10. Experimental results of group delay vs frequency for a FVW in two 20-μ-thick YIG films spaced 50 μ apart and using the transducer geometry of Fig. 7(b).

er. The transducer pair elements and films were kept apart by several layers of a commercial polymer film (Saran wrap). The group delay results are shown in Fig. 10. The two noteworthy features of these results are the substantial noise or interference and the delay behavior more characteristic of an A-mode, see Fig. 8.

At this juncture it was decided to perform a coupling constant calculation the details of which are given in the Appendix. The calculations could only be readily performed for equal films with ground planes far away—a situation which fortunately described the experimental conditions. We term the coupling constants $K_{internal}$ when the wires are between the films, as in Fig. 7(b), and $K_{external}$ when the wires are outside the films, as in Fig. 7(c). Figure 11 shows the results of these calculations. The results of Fig. 10 for FVWs are now explainable by the curves of Fig. 11 (upper left). Since $K_{int}(A) > K_{int}(S)$ any asymmetry in the magnitude or geometry of J_1 and J_2 will cause some A-mode generation. Ideally, for S-mode generation $J_1 = -J_2$ exactly. Figure 10 suggests that significant asymmetry exists and mostly A-

mode is being launched with some interference from a weaker S-mode. Physically the reason for the low $K_{int}(S)$ for FVWs is that the fields from the opposing current elements will tend to cancel, particularly as the elements are brought close together. A solution to this problem is clearly to use the external configuration of Fig. 7(c). In Fig. 11 (lower left) $K_{ext}(S) > K_{ext}(A)$ but $K_{ext}(A)$ is not negligible and such a transducer arrangement will still be susceptible to launching the A-mode if any asymmetries exist. Experiments have not yet been performed with the Fig. 7(c) geometry because the gadolinium gallium garnet (GGG) substrates, supporting the YIG films, were too thick (500 μ) to allow close placement of the gold ribbon transducers for effective coupling. Experiments are planned to grow two YIG films directly on a thin GGG spacer.

IV. CONCLUSIONS

Using a technique termed "surface permeabilities" a general expression was derived for the dispersion relation of magnetostatic waves propagating in two ferrimagnetic films coupled by their close proximity. From the symmetry of the rf magnetization within the films two sets of modes were identified for FVWs and BVWs termed the symmetric and antisymmetric, respectively. Additionally, two films of different static magnetization $(4\pi M)$ were found to support a magnetostatic wave in a frequency range normally outside that for propagation in the lower value film. Group delay measurements were performed on epitaxially grown YIG double films which confirmed the dispersion analysis and mode identification. However, coupling constant calculations for the two modes showed that the relative excitation strength of each was transducer geometry dependent. In practice, it may prove difficult to always excite one desired mode without stimulating the second to some degree.

V. ACKNOWLEDGMENTS
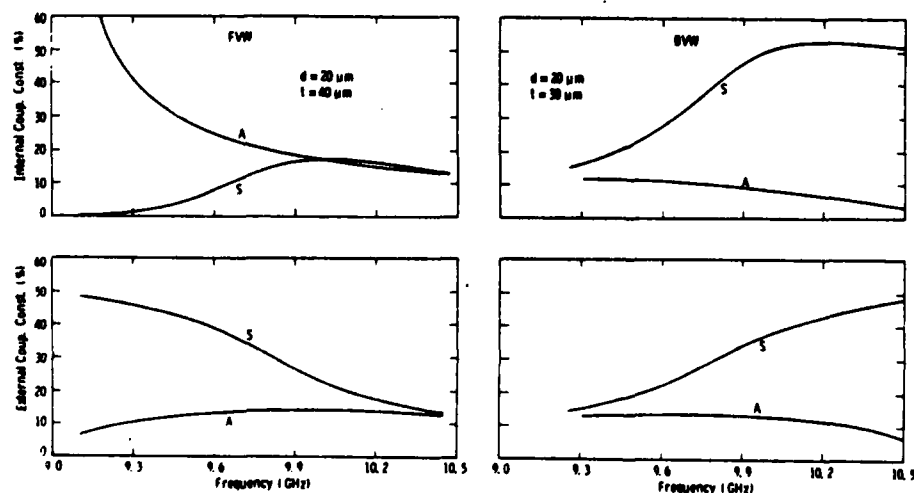
FIG. 11. Coupling constants as a function of frequency for the excitation of FVW and BVW S- and A- modes in two 20-μ-thick films; $4\pi M_1 = 4\pi M_2 = 1.8$ kG, $H_{FVW} = 3.214$ kG, $H_{BVW} = 2.991$ kG, S_1 and $S_2 \rightarrow + \infty$, respectively.

3728   J. Appl. Phys., Vol. 53, No. 5, May 1982   M. R. Daniel and P. R. Emtage   3728

165

APPENDIX: COUPLING TO A CURRENT

We shall treat the generation of magnetostatic waves in the system sketched in Fig. 7(b), where the stimulating currents J_1 and J_2 are between the two films. Results for exterior currents, as in Fig. 7(c), are given at the end. The method is that of Ref. 4, except that two sheets of current are present. The influence of the ground plane will be neglected.

Let $b_k(y)$ and $h_k(y)$ be the Fourier transforms of b_y and h_x in the plane $y = \text{const}$.

$$b_y(x,y) = \frac{1}{2\pi} \int b_k(y) e^{ikx} dk , \quad \text{etc.}$$

The current sheet J_1 in $y = t$ gives rise to the field discontinuity

$$h_x(x,t+) - h_x(x,t-) = -j_1(x) .$$

Upon taking Fourier transforms, using the definitions of μ^s, μ^{in}, μ^{sp} in Eqs. (5) and (8), and noting that b_y is continuous across $y = t$, we obtain

$$b_k(t) = \frac{i\mu_0 j_1(k)\mu^{sp}(t)\mu^{in}(t)}{[\mu^{sp}(t) - \mu^{in}(t)]} , \tag{A1}$$

where $j_1(k)$ is the Fourier transform of the current $j_1(x)$.

It is convenient to obtain the total field in the plane $y = 0$, where the second current sheet J_2 flows. The algebra is greatly simplified if we note that we shall later integrate b_k over k in order to obtain the field at large distances. The dominant contribution comes from the pole at $\mu^{sp} = \mu^{in}$, and we can use this substitution everywhere except in the denominator. In the plane $y = 0$, the field $b_k^{(1)}$ due to J_1 is found to be

$$b_k^{(1)}(0) = \frac{ir j_1 \mu_0 [\mu^s(0)]^2}{[\mu^{sp}(0) - \mu^{in}(0)]} , \tag{A2}$$

where

$$r = \cosh kt - \mu^s(0)\sinh kt . \tag{A3}$$

The total flux due to both currents is a similar quantity proportional to $j_2 + rj_1$. Upon taking Fourier transforms, the travelling field on the right of the transducer is found to be

$$b_y(x) = \frac{\mu_0[\mu^s(0)]^2(j_2 + rj_1)e^{ikx}}{(\partial/\partial k)[\mu^{sp}(0) - \mu^{in}(0)]} , \tag{A4}$$

where k is now the root of the secular equation.

It is shown in the Appendix of Ref. 4 that the power travelling to the right is

$$P^+ = \frac{1}{2} \frac{\omega}{k} \mu_0 |h_x|^2 \frac{\partial}{\partial k}(\mu^{in} - \mu^{sp}) ,$$

where h_x and μ^s are found in the same plane. On using Eq. (A4) to obtain $h_x = ib_y/\mu_0\mu^s$, we obtain

$$P^+ = \frac{1}{2}\mu_0\omega(j_2 + rj_1)^2 K^+ , \tag{A5}$$

in which K^+ is a coupling constant,

$$K^+ = [\mu^s(0)]^2/k \frac{\partial}{\partial k}[\mu^{in}(0) - \mu^{sp}(0)] . \tag{A6}$$

This definition differs by a factor of two from that used in Ref. 4, because there are two films (see below).

Symmetric system

For two equal films with $\mu_{12} = 0$, text Eq. (15) is, at the roots of the secular equation,

$$\mu^s(0) = \tanh \frac{1}{2} kt , \quad \text{(even modes)} ,$$

$$= \coth \frac{1}{2} kt , \quad \text{(odd modes)} .$$

From Eq. (A3) we find $r = \pm 1$ for even and odd modes. The total power radiated in the positive direction is the sum of powers in even and odd modes

$$P^+ = \frac{1}{2}\mu_0\omega[(j_2 + j_1)^2 K_e^+ + (j_2 - j_1)^2 K_0^+] . \tag{A7}$$

Note that, for widely separated films and $j_1 = 0$, only the lower film is excited and $K_e^+ \simeq K_0^+ = K^+$. The radiated power is then $P^+ = \mu_0\omega j_2^2 K^+$, which agrees with the definition in Ref. 4 for coupling to a single film.

The permeabilities in Eq. (A6) are given in text Eqs. (11) and (13). Evaluation in the case of a symmetric system without a ground plane gives

$$K^+ = \mu_{22}k^{-1}[2d + \mu_{22}t - \mu_{22}$$
$$\times (2d\mu_{11} + t)(\mu^s(0))^{-2}]^{-1} . \tag{A8}$$

This form holds equally for odd and even modes.

Exterior currents

When the current sheets lie outside the magnetic films, as in Fig. 7(c), an extension of the above argument yields a power dissipation similar to that in Eq. (A7), except that the coupling constants are multiplied by a numerical factor

$$K_{\text{exterior}}^+ = K^+[1 - \mu_{11}\mu_{22}(\mu^s(0))^{-2}]$$
$$\times [1 - \mu_{11}\mu_{22}]^{-1} . \tag{A9}$$

[1]L. R. Adkins and H. L. Glass, Electron. Lett. 16, 503 (1980).
[2]P. Grünberg, J. Appl. Phys. 51, 4338 (1980).
[3]H. Sasaki and N. Mikoshiba, J. Appl. Phys. 52, 3546 (1981).
[4]P. R. Emtage, J. Appl. Phys. 49, 4475 (1978).
[5]This concept of surface permeability is similar to that of surface impedance used in electrical engineering problems.

3729   J. Appl. Phys., Vol. 53, No. 5, May 1982

M. R. Daniel and P. R. Emtage   3729

166

APPENDIX III   SURFACE WAVE GENERATION

The generation of surface magnetostatic waves by a single current sheet has been calculated by the method used for volume waves in Appendix II. Symmetrically placed current sheets were not considered, because the inherent asymmetry of surface waves renders selective excitation unlikely. Ground planes are ignored, because our principal interest is in finding out which type of mode is most strongly generated.

No algebraic simplification has been possible. We give our results for equal films of thickness d separated by a distance t. Define

$$\mu_{11} = \mu_{22} = \mu \ , \ \mu_{12} = \kappa,$$

$$S = \pm 1 \text{ as } k = \pm.$$

Surface permeabilities at the upper and lower boundaries of the central space, and in its middle, are

$$\mu(+) = \frac{S\mu + (\mu^2 - \kappa^2 - S\kappa) \tanh kd}{\mu + (S+\kappa) \tanh kd},$$

$$\mu(-) = -\frac{S\mu + (\mu^2 - \kappa^2 + S\kappa) \tanh kd}{\mu + (S-\kappa) \tanh kd},$$

$$\mu(0) = \frac{\mu(+) + \tanh (kt/2)}{1 + \mu(+) \tanh (kt/2)}.$$

For a current outside the films, and adjacent to the lower layer, the coupling constant is

$$K = -1/2kdQ,$$

where

167

$$Q = \text{sech}^2 kd \; \frac{\mu^2 - \kappa^2 + \kappa(S - \mu(-)) + S\mu(-)}{\mu + (\mu(-) + \kappa)\;\tanh kd}$$

$$+ \frac{\mu - (\kappa - S)\;\tanh kd}{\mu + (\mu(-) + \kappa)\;\tanh kd} \left\{ \frac{t}{d}\;\text{sech}^2 kt\; \frac{1 - \mu(+)\mu(\;)}{1 + \mu(+)\;\tanh kt} \right.$$

$$\left. + \text{sech}^2 kd\; \frac{1 - \mu(-)\;\tanh kt}{1 + \mu(+)\;\tanh kt} \cdot \frac{\mu^2 - \kappa^2 - \kappa(S + \mu(+)) - S\mu(+)}{\mu + (\mu(+) + \kappa)\;\tanh kd} \right\} \; .$$

For a current between the two films (which is the only position in which symmetry requires that $K^+ = K^-$), we find for positive k

$$K = -\mu(0)^2/2kdQ,$$

where

$$Q = \text{sech}^2 kd \left\{ \frac{1 - \mu(0)\;\tanh \tfrac{1}{2} kt}{1 + \mu(+)\;\tanh \tfrac{1}{2} kt} \cdot \frac{\mu^2 - \kappa^2 - \kappa - (1 + \kappa)\mu(+)}{\mu + (1 + \kappa)\;\tanh kd} \right.$$

$$\left. + \frac{1 + \mu(0)\;\tanh \tfrac{1}{2} kt}{1 - \mu(-)\;\tanh \tfrac{1}{2} kt} \cdot \frac{\mu^2 - \kappa^2 + \kappa + (1 - \kappa)\mu(-)}{\mu + (1 - \kappa)\;\tanh kd} \right\}$$

$$+ \tfrac{1}{2} \frac{t}{d}\;\text{sech}^2 \tfrac{1}{2} kt \left\{ \frac{1 - \mu(+)\mu(0)}{1 + \mu(+)\;\tanh \tfrac{1}{2} kt} + \frac{1 - \mu(-)\mu(0)}{1 - \mu(-)\;\tanh \tfrac{1}{2} kt} \right\} \; .$$

168

MISSION
of
Rome Air Development Center

RADC plans and executes research, development, test and selected acquisition programs in support of Command, Control Communications and Intelligence (C^3I) activities. Technical and engineering support within areas of technical competence is provided to ESD Program Offices (POs) and other ESD elements. The principal technical mission areas are communications, electromagnetic guidance and control, surveillance of ground and aerospace objects, intelligence data collection and handling, information system technology, ionospheric propagation, solid state sciences, microwave physics and electronic reliability, maintainability and compatibility.

END

FILMED

11-83

DTIC